GEORG-AUGUST-UNIVERSITÄT GÖTTINGEN

UNIVERSITÄTSMEDIZIN GÖTTINGEN UMG

STUDYING THE ROLE OF COENZYME Q_{10} IN MITOCHONDRIAL CALCIUM AND REDOX SIGNALING

Dissertation

for the award of the degree

"*Doctor rerum naturalium*"

of the Georg-August-Universität Göttingen

within the doctoral program *Molecular Medicine*

of the Georg-August University School of Science (GAUSS)

Submitted by:

ZURIÑE BONILLA DEL RÍO

Born in Barakaldo, Spain

Göttingen, 2022

Members of the thesis committee:

Prof. Dr. Ivan Bogeski
Institute of Cardiovascular Physiology
University Medical Centre, Georg-August University Göttingen

Prof. Dr. Michael Meinecke
Department of Cellular Biochemistry
University Medical Centre, Georg-August University Göttingen

Dr. rer. nat. Antje Ebert
Cardiovascular Cell Biology and Systems Medicine
University Medical Centre, Georg-August University Göttingen

Further members of the Examination Board:

Dr. Katrin Streckfuß-Bömeke
Clinic for Cardiology and Pneumology / Heart Center Göttingen
University Medical Centre, Georg-August University Göttingen

Prof. Dr. Ralph Kehlenbach
Department of Molecular Biology
University Medical Centre, Georg-August University Göttingen

Prof. Dr. Thomas Meyer
Molecular Psychocardiology Laboratory
University Medical Centre, Georg-August University Göttingen

Date of oral examination: 1st March 2022

Supervised by:

Prof. Dr. med. IVAN BOGESKI

Dedicated to my parents and sister,
who always supported and encouraged me
to go on every adventure, especially this one.

INDEX

Abbreviations

ADP: adenosine diphosphate

AIF = AIFM1: mitochondrial apoptosis-inducing factor

AIFM2: apoptosis-inducing factor mitochondrial 2

APS: ammonium persulfate

APTX: aprataxin

ATP: adenosine triphosphate

BRAF: RAF kinase, isoform B

BSA: bovine serum albumin

BSO: buthionine sulfoximine

Ca^{2+}: calcium ions

CAT: catalase

Cb5R: monoamine oxidase and cytochrome b5 reductase

CCCP: carbonyl cyanide m-chlorophenyl hydrazine

cDNA: complementary DNA

CM: cardiomyocytes

CNS: central nervous system

CO_2: carbon dioxide

CoQ_1: coenzyme Q_1

CoQ_{10}: coenzyme Q_{10} or ubiquinone

$CoQ_{10}H^{\bullet}$: semiquinone or semi-ubiquinone

$CoQ_{10}H_2$: reduced CoQ_{10} or ubiquinol

CoQs: quinones

CRAC: Ca^{2+} release-activated Ca^{2+}

CT: cycle threshold

CTB: CellTiter-Blue

CVDs: cardiovascular diseases

Cyt_c: cytochrome c

cytCa^{2+}: cytosolic Ca^{2+}

cytH_2O_2: cytosolic H_2O_2

ddH_2O: double-distilled water

DecylQ: decylubiquinone

DEPC: diethylpyrocarbonate

Dig: digitonin

DMEM: Dulbecco's modified Eagle's medium

DMSO: dimethylsulfoxid

DNA: deoxyribonucleic acid

dNTP: deoxynucleoside triphosphate

DTT: dithiothreitol

e^-: electrons

ECAR: extracellular acidification rate

EDTA: ethylenediaminetetraacetic acid

Em: emission

EMRE: essential MCU regulator

ER: endoplasmic reticulum

ER Ca^{2+}: Ca^{2+} concentration in the endoplasmic reticulum

ETC: electron transport chain

ETFDH: electron-transferring-flavoprotein dehydrogenase

EtOH: ethanol

Ex: excitation

FAD$^+$: oxidized flavin adenine dinucleotide

$FADH_2$: reduced flavin adenine dinucleotide

FBS: fetal bovine serum

Fe^{2+}: ferrous iron

Fe^{3+}: ferric iron

$FeO^{\bullet}$/$FeOO^{\bullet}$: perferryl radicals

FINs: ferroptosis inducers

FPP: farnesyl pyrophosphate

FQR: electron transfer flavoprotein-ubiquinone oxidoreductase

FRET: fluorescence resonance energy transfer

FSP1: ferroptosis suppressor protein 1

GCL: glutamate-cysteine ligase

GPCR: G protein-coupled receptors

GPDH: glycerol-3-phosphate dehydrogenase

GPx: glutathione peroxidases

GPX4: glutathione peroxidase 4

GRX: glutaredoxins

GSH: Glutathione

GSSG: glutathione disulphide

H^{+}: protons

H_2O: water

H_2O_2: hydrogen peroxide

H_3PO_4: phosphoric acid

HEPES: 4-(2-hydroxyethyl)-1-piperazineethanesulfonic acid

His: histamine

$HO^{\bullet}$: hydroxyl radical

HSF: human skin fibroblasts

IC50: half maximal inhibitory concentration

IMM: inner mitochondrial membrane

IMS: intermembrane space

IP_3: inositol 1,4,5-triphosphate

IP_3R: inositol 1,4,5-triphosphate receptor

iPSC-CM: induced pluripotent stem cell – derived cardiomyocytes

LETM1: leucine zipper-EF-hand-containing transmembrane protein 1

LPO: lipid peroxidation

$m\Delta\Psi$: mitochondrial membrane potential

mCa^{2+}: mitochondrial matrix Ca^{2+}

MCU: mitochondrial calcium uniporter

MCUa: mitochondrial calcium uniporter a

MCUb: mitochondrial calcium uniporter b

MCUR1: mitochondrial calcium uniporter regulator 1

mH_2O_2: mitochondrial H_2O_2

MICU1: mitochondrial calcium uptake 1

MICU2: mitochondrial calcium uptake 2

MICU3: mitochondrial calcium uptake 3

mito-CoQs: mitocondria-targeted quinones

mitoQ: mitoquinone mesylate

mPTP: mitochondrial permeability transition pore

mRNA: messenger-RNA

mROS: mitochondrial ROS

mtDNA: mitochondrial DNA

Na_3VO_4: sodium orthovanadate

NaCl: sodium chloride

$NAD(P)^+$: oxidized nicotinamide adenine dinucleotide (phosphate)

NAD(P)H: reduced nicotinamide adenine dinucleotide (phosphate)

NaF: sodium fluoride

nCa^{2+}: nuclear matrix Ca^{2+}

NCX: Na^+ / Ca^{2+} exchanger

NOX: NADPH oxidase

O_2: molecular oxygen

$O_2^{-\bullet}$: superoxide

OCR: oxygen consumption rate

OH-CoQs: hydroxylated quinones

OH-decylQ: hydroxy- decylubiquinone

OH-mitoQ: hydroxy- mitoquinone trifluoroacetate

OH-Q_1: hydroxy- coenzyme Q_1

OMM: outer mitochondrial membrane

Orai 1: calcium release-activated calcium channel protein 1

Orai 2: calcium release-activated calcium channel protein 2

Orai 3: calcium release-activated calcium channel protein 3

OXPHOS: oxidative phosphorylation

PBS: phosphate buffered saline

PDH: pyruvate dehydrogenase

PFA: paraformaldehyde

pH: power of hydrogen

Pi: phosphate ions

PI: protease Inhibitor

PMCA: plasma membrane Ca^{2+} transport ATPase

PMSF: phenylmethylsulfonylfluorid

PNS: peripheral nervous system

PRDX: peroxiredoxins

PUFA: polyunsaturated fatty acids

Q_1: coenzyme Q_1

$R^{\bullet}$: free radical

RNA: ribonucleic acids

ROI: regions of interest

ROO•: lipid peroxyl radical

ROOH: lipid hydroperoxyl radical

ROS: reactive oxygen species

rpm: revolutions per minute

RPMI: Roswell Park Memorial Institute

RSL3: RAS-selective lethal 3

RT-qPCR: real-time quantitative polymerase chain reaction

RyR: ryanodine receptor

SDS: sodium dodecyl sulfate

SDS-PAGE: sodium dodecyl sulfate polyacrylamide gel electrophoresis

SEM: standard error of the mean

SERCA: sarco/endoplasmic reticulum Ca^{2+}-ATPase

SOCE: storage-operated Ca^{2+} entry

SOD: superoxide dismutase

SR: sarcoplasmic reticulum

STIM1: stromal interaction molecule 1

STIM2: stromal interaction molecule 2

Sx_c^-: cystine/glutamate antiporter system

TBP: TATA-binding protein

TBS: tris-buffered saline

TBS-T: tris-buffered saline - Tween

TCA: tricarboxylic acid cycle

TEMED: tetramethylethylenediamine

Tg: thapsigargin

TGH buffer: buffer based on Triton X-100, glycerol and HEPES

TMRM: tetramethylrhodamin-methylester-perchlorat

TPP^+: triphenylphosphonium cation

TRPC: transient receptor potential channels

TRPML1: TRPC mucolipin 1

TRX: thioredoxins

UCP2: mitochondrial uncoupling protein 2

UCP3: mitochondrial uncoupling protein 3

V: volt

VDAC: voltage-dependent anion channel

WB: western blot

WHO: World Health Organization

4HB: 4-hydroxybenzoate

4NB: 4-nitrobenzoate

αKGDH: α-ketoglutarate dehydrogenase

Δ**p**: proton gradient

° **C**: degree Celsius

1. SUMMARY

Mitochondria can take up large amounts of calcium (Ca^{2+}) in order to control the activity of several enzymes and their bioenergetics output. As a consequence of this metabolic flux, reactive oxygen species (ROS) are generated that modulate cell signaling pathways, contributing to many cellular processes. Coenzyme Q_{10} (CoQ_{10}) is an essential component of the mitochondrial electron transport chain (mETC) and is also found in other cellular compartments such as the plasma membrane. Due to their role as effective antioxidants, CoQs act as radical scavengers in the mitochondria, and prevent lipid peroxidation (LPO) in the plasma membrane. Accordingly, CoQs are crucial regulators of the mitochondrial bioenergetics and of ferroptosis. Coenzyme Q_{10} insufficiency is related to severe pathologies in humans. This deficit can be caused by mutations in genes involved in CoQ_{10} biosynthesis or by defects in other biological functions that are indirectly related. Furthermore, statins, used as inhibitors of the mevalonate pathway in the treatment of hypercholesterolemia, also induce a CoQ_{10} deficiency causing serious side effects. In patients with CoQ_{10} deficiency, supplementation with CoQ_{10} is used as a first line of therapy. However, the effectiveness of this approach is rather limited.

Here, we demonstrate that CoQ_{10} regulates mitochondrial Ca^{2+} and redox signaling as well as ferroptotic cell death in primary human skin fibroblasts (HSF) and iPSC-derived cardiomyocytes (iPSC-CM). In this regard, depletion of CoQ_{10} elevated mitochondrial Ca^{2+} (mCa^{2+}) uptake while its upregulation caused a decrease in mCa^{2+}. Treatment with mitochondrially targeted CoQ_{10} (mitoQ) reduced ROS levels but suppressed essential cellular parameters such as respiration, mitochondrial membrane potential ($m\Delta\Psi$) and viability in HSF. Furthermore, addition of mitoQ to CoQ_{10} deficient patient-derived HSF caused similar negative effects and did not compensate for the intrinsic CoQ_{10} deficiency. Hydroxylated CoQ forms (OH-CoQs) act as potent antioxidants, transport Ca^{2+} across artificial bio-membranes and have been suggested to have superior properties when compared to the native CoQs. We generated mitochondrial targeted OH-CoQ_{10} (OH-mitoQ) and tested its role in the same cellular systems. Notably, the antioxidant effects of OH-mitoQ were comparable with those of mitoQ. However, OH-mitoQ had less side-effects when compared with mitoQ. We also found that both mitoQ and OH-mitoQ were effective inhibitors of ferroptosis. These findings suggested that mitochondrial redox and Ca^{2+} signalling play an important role in this form of cell death. To investigate the functional relevance and the role of mitochondria within the CoQ_{10}-ferroptosis axis, we exposed CoQ_{10}-deficient HSF and iPSC-CM to ferroptosis inducers (FINs). Surprisingly, we found that CoQ_{10} deficient cells display reduced ferroptotic sensitivity.

These results thus suggested that CoQ_{10} protective properties are compensated by alternative regulatory pathway(s) or antioxidant system(s).

In summary, our findings suggest that due to their redox properties, OH-CoQs are superior to the CoQs and are thus potential drugs for treating primary and secondary CoQ_{10} deficiencies. Moreover, our study indicates that mitochondrial redox signals are important regulators of ferroptosis.

Key words: Coenzyme Q_{10}, Hydroxylated-CoQs, Calcium signaling, Redox signalling, Reactive Oxygen Species, Lipid peroxidation, Ferroptosis, Fibroblasts, iPSC-cardiomyocytes.

2. INTRODUCTION

2.1. MITOCHONDRIA

Mitochondria are essential organelles presented in the cytoplasm of eukaryotic cells. They are involved in the regulation of multiple metabolic and signaling pathways. Mitochondrial respiration is their most critical function, as it provides the cell with the energy (in the form of Adenosine triphosphate, ATP) needed to power the biochemical reactions through a process called oxidative phosphorylation (OXPHOS), which takes place in the electron transport chain (mETC) (Tait & Green, 2012). Mitochondria are also implicated in β-oxidation of fatty acids, amino acid catabolism, ketone body synthesis, heme biosynthesis, urea cycle, steroidogenesis, gluconeogenesis and calcium storage (Bravo-Sagua et al., 2017). Due to their function in energy production, mitochondria are crucial for the proper functioning of highly energy-demanding organs, such as muscles, the brain and the heart (Magner et al., 2015).

On the other hand, mitochondrial dysfunction is a characteristic of aging, essentially of all chronic diseases. These diseases include neurodegenerative diseases, cardiovascular diseases, diabetes and metabolic syndromes, autoimmune diseases, neurobehavioral and psychiatric diseases, gastrointestinal disorders, fatiguing illnesses, musculoskeletal diseases, cancer and chronic infections (Nicolson, 2014).

2.1.1. Mitochondrial structure

The presence of two membranes defines mitochondria, the outer and inner mitochondrial membranes (OMM and IMM), composed of lipid bilayers, creating two spaces within the organelle (**Figure 1**). The intermembrane space (IMS), which is required to establish the electrochemical proton gradient (Δp), and the mitochondrial inner space, the matrix, which is the site for mitochondrial DNA (mtDNA) replication, transcription and protein synthesis, and contains numerous metabolic enzymes.

The OMM has a high permeability, allowing the crossing of small uncharged molecules and ions via porins such as the voltage-dependent anion channel, VDAC, which enables the transport of all energy-related metabolites (i.e., succinate, malate, pyruvate, NADH, ATP, ADP and phosphate) from the cytosol into the mitochondria (Bravo-Sagua et al., 2017). Whereas bigger molecules, such as proteins, require specific translocases (Grevel et al., 2019). By contrast, the IMM behaves as a tight barrier for ions and molecules. These can only get across

through specific and selective membrane transport proteins; for example, in the case of calcium ions (Ca^{2+}), the mitochondrial calcium uniporter (MCU) complex. Consequently, a natural electrochemical membrane potential is formed across the IMM (Kuhlbrandt, 2015).

The IMM forms invaginations, the so-called "cristae", which extend into the mitochondrial matrix, causing an increase in its surface area. Integrated into the IMM, especially on the cristae, protein complexes of the mETC can be found; consequently, this increase in IMM enhances the capacity of the mitochondria to synthesize ATP (**Figure 1**) (Cogliati et al., 2013).

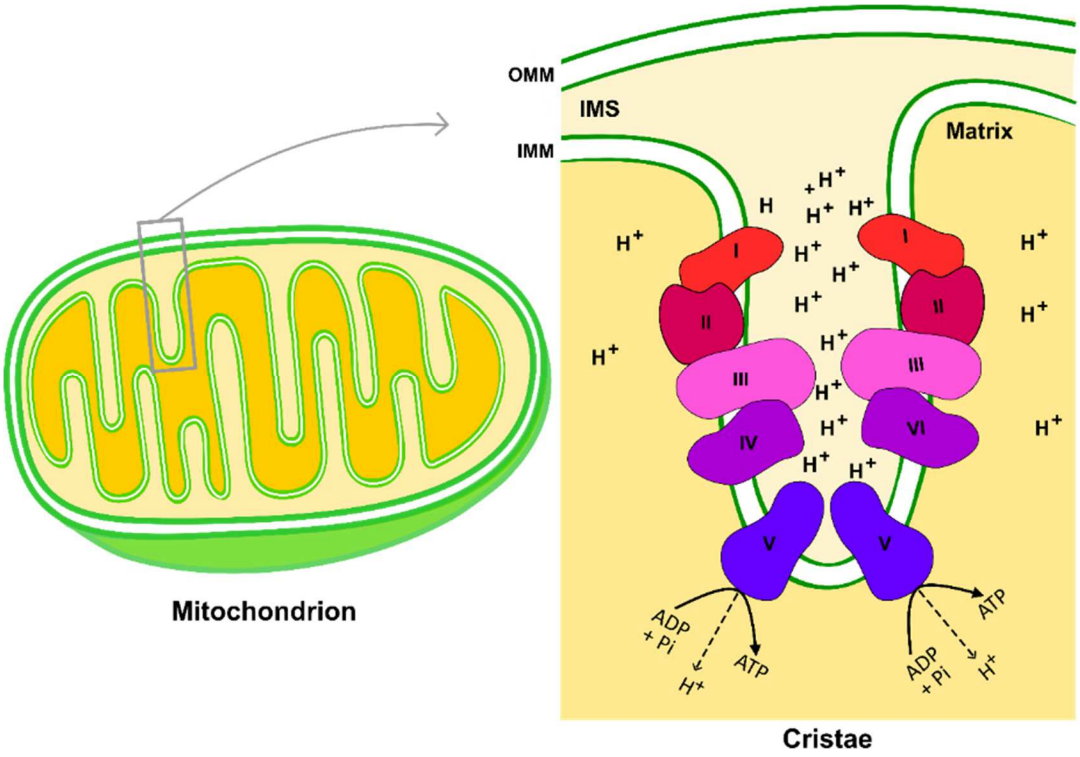

Figure 1. *Drawing of the mitochondrion' structure showing its compartments: outer mitochondrial membrane, inner mitochondrial membrane, intermembrane space and matrix. In an enlarged form, the model of a cristae with the oxidative phosphorylation (OXPHOS) complexes (I-V) representing, in simplified form, the energy production in form of adenosine triphosphate (ATP) molecules. Due to the current of protons taken up by Complex V, it phosphorylates adenosine diphosphate, producing ATP. Abbreviations: ADP = adenosine diphosphate; ATP = adenosine triphosphate; H^+ = protons; IMM = inner mitochondrial membrane; IMS = intermembrane space; OMM = outer mitochondrial membrane.*

2.1.2. Mitochondrial electron transport chain

The central role of mETC is, as mentioned, supplying the energy needed for all the cellular processes via the mechanism known as OXPHOS. It consists of passing electrons (e^-) collected from the metabolism of sugars, proteins and fatty acids through the complexes of the mETC up to, finally, reach the last acceptor, the molecular oxygen (O_2) (**Figure 2**).

At a more detailed level, Complex I (NADH-ubiquinone oxidoreductase) takes e^- from glucose's catabolism. Glucose is transformed into pyruvate through a series of reactions taking place in the cytoplasm (glycolysis). Pyruvate enters the mitochondrial matrix, where it is further decarboxylated by pyruvate dehydrogenase (PDH) into acetyl CoA. Acetyl CoA undergoes some reactions in the tricarboxylic acid cycle (TCA cycle or Krebs cycle), generating high energy-rich e^- in the form of reduced nicotinamide adenine dinucleotide (NADH) and carbon dioxide (CO_2). NADH transfers its energy-rich e^- to Complex I.

Additionally, Complex II (succinate-ubiquinone oxidoreductase) takes energy-rich e^- in the form of reduced flavin adenine dinucleotide ($FADH_2$) provided mainly by fatty acid β-oxidation.

Coenzyme Q_{10} (CoQ_{10}) picks up e^- from Complexes I and II and transports them to Complex III (succinate-cytochrome c oxidoreductase). Through complex redox reactions, the e^- are then transferred to Complex IV (cytochrome c oxidase).

Lastly, O_2 is the final e^- acceptor, reducing to water (**Figure 2**).

The energy generated through the e^- flow pumps protons (H^+) across the IMM to the IMS, generating an electrochemical Δp, which accounts for over 90 % of the available respiratory energy. Differences in the electrochemical potential across the IMM are known as the mitochondrial membrane potential ($m\Delta\Psi$) and refer to the functional metabolic state of the mitochondria.

These H^+, in the IMS, are caught by ATP synthase (Complex V) to synthesize ATP from adenosine diphosphate (ADP) and phosphate ions (Pi). As a result, cells generate 36 ATP molecules per glucose molecule through OXPHOS (Letts & Sazanov, 2017).

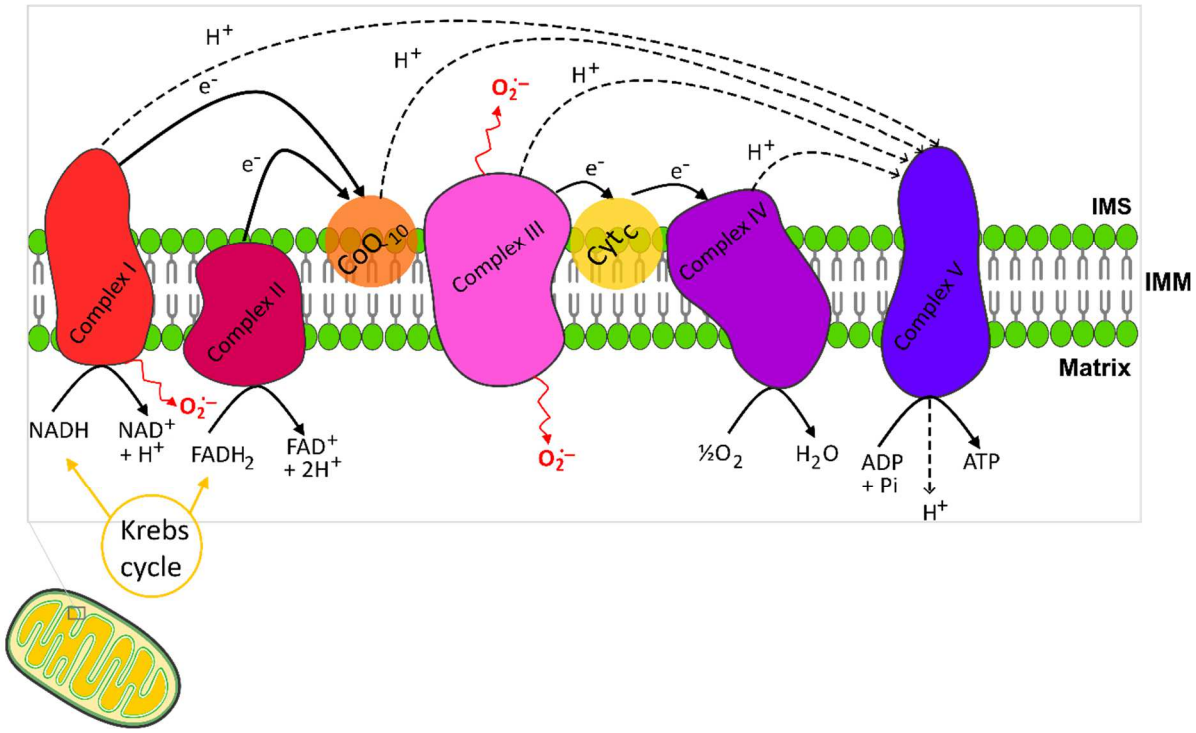

Figure 2. *Oxidative phosphorylation in the Inner Mitochondria Membrane. Electrons from NADH and $FADH_2$ (produced in cell metabolism) are accepted by Complexes I and II and transported to Complex III through CoQ_{10} and then to Complex IV. Finally, electrons are taken by O_2, producing water. The electron flow provides the energy to pump protons (H^+) across the membrane to the intermembrane space, generating the electrochemical gradient. Complex V uses the H^+ and synthesizes ATP from ADP and phosphate ions. Abbreviations: ADP = adenosine diphosphate; ATP = adenosine triphosphate; Cyt_c = cytochrome c; e^- = electrons; FAD^+ = oxidized flavin adenine dinucleotide; $FADH_2$ = reduced flavin adenine dinucleotide; H^+ = proton; H_2O = water; IMM = inner mitochondrial membrane; IMS = intermembrane space; NAD^+ = oxidized nicotinamide adenine dinucleotide; NADH = reduced nicotinamide adenine dinucleotide; O_2 = molecular oxygen; $O_2^{-\bullet}$ = superoxide; Pi = phosphate ion.*

2.2. COENZYME Q_{10}

Coenzyme Q or ubiquinone, first described by Cain and Morton in 1955 (Cain & Morton, 1955), is the only endogenously synthesized redox-active lipid found in all endomembranes, plasma membrane and serum lipoproteins; being especially abundant in mitochondria, as a component of the mETC (Turunen et al., 2004). It comprises a benzoquinone ring as a head group and a polyisoprenoid chain, which varies in length depending on the species. It has ten isoprene units in humans, being named Coenzyme Q_{10} (CoQ_{10}) (Rodriguez-Aguilera et al., 2017) (**Figure 3**). It is generally accepted that the isoprenoid chain is within the membrane's lipid bilayer stabilizing the molecule, while the quinone ring moves across the IMM, depending on its redox state (Alcazar-Fabra et al., 2016).

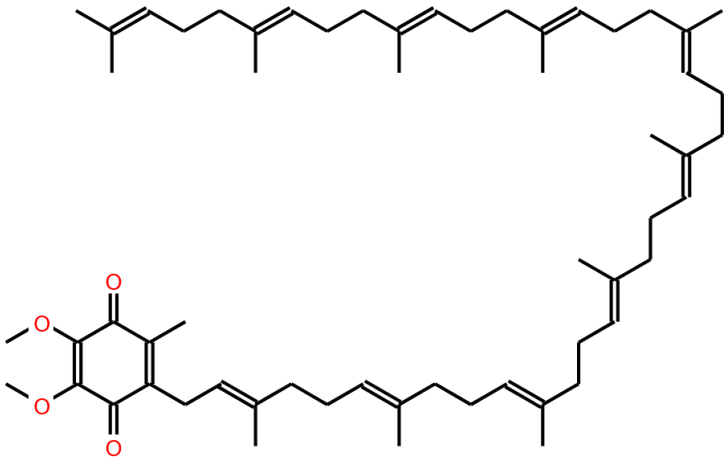

***Figure 3**. Coenzyme Q_{10} (CoQ_{10}) chemical structure in humans. The schematic representation distinguishes the benzoquinone ring and the lipophilic polyisoprenoid side chain composed of ten isoprene units. CoQ_{10} is an essential component of the mitochondrial electron transport chain (mETC) where it mediates electron transport and the absorption and release of protons in the intermembrane space, thus generating the mitochondrial membrane potential necessary for ATP synthesis. In addition to the mETC in the inner mitochondrial membrane, it is found in other cellular components such as the plasma membrane. In its reduced state, CoQ_{10} is an effective antioxidant. In the mitochondria, CoQ_{10} acts as a radical scavenger, while in the plasma membrane it acts as an inhibitor of lipid peroxidation.*

The primary function of CoQ_{10} in the mETC was proposed by Crane *et al*. in 1957 (Crane, 1957). They observed that Q275 (later called CoQ) underwent oxidation and reduction steps

when incubated with isolated mitochondria. Furthermore, they saw that these redox changes were inhibited by specific mitochondrial inhibitors, which evidenced the role of Q275 as an e^- carrier in the mETC.

However, it was not until 1975 when Mitchell discovered the contribution of CoQ to energy conversion (Mitchell, 1975). He had been considering the formation of a $m\Delta\Psi$ as the driving force for ATP synthesis. Mitchell discovered that CoQ was involved in the generation of a Δp across the membrane. It was shown that CoQ's redox state mediates the transport of e^- and the uptake and release of H^+ into the IMS, thereby generating the necessary $m\Delta\Psi$ for ATP synthesis.

In 1990, the role of CoQ as an antioxidant was defined. Early studies had shown that the reduced form of CoQ was an excellent free radical scavenger and antioxidant, but this role was not established until its general distribution in all cell membranes was known (Kagan et al., 1990). In addition, supporting this discovery, CoQ can be efficiently regenerated by various dehydrogenases through continuous oxidation/reduction cycles, providing the molecule with high effectiveness against oxidative stress (Bentinger et al., 2010).

Later in the 2000s, several other essential functions were attributed to CoQ, although a more extensive investigation is needed to understand this molecule better. It was described that CoQ could prevent lipid peroxidation (**Figures 11** and **13**) by donating a hydrogen atom from one of its hydroxyl groups to a lipid peroxyl radicals ($ROO^{\bullet}$). In addition, reduced CoQ prevents propagation of lipid peroxidation by reducing the initial perferryl radical ($FeO^{\bullet}/FeOO^{\bullet}$) and regenerating vitamin E, another important antioxidant within the IMM, from the α-tocopheroxyl radical (Bentinger et al., 2007; Bentinger et al., 2010).

Furthermore, hydrogen peroxide (H_2O_2), one of the more stable reactive ROS, interferes with metal ions attached to the DNA during oxidative stress, generating hydroxyl radicals. With its role as an antioxidant, CoQ was shown to efficiently prevent DNA base oxidation, which is particularly important in the case of mtDNA due to the lack of efficient DNA repair-mechanisms (Bentinger et al., 2010).

Additionally, CoQ constitutes an essential cofactor for uncoupling proteins (UCP) as H^+ from fatty acids are transferred to these proteins via oxidized CoQ (Echtay et al., 2000). The role of UCP in the IMM is the passage of H^+ from the IMS to the matrix. Consequently, the Δp formed by the mETC is uncoupled from OXPHOS and heat is generated instead.

CoQ is also known for being a modulator of the mitochondrial permeability transition pore (mPTP). An essential function in cell metabolism since the opening of the mPTP causes the collapse of mitochondrial function by translocating molecules as large as 1500 Da, leading to necroptosis and cell death (Fontaine et al., 1998; Liu et al., 2020; Rasola & Bernardi, 2011).

CoQ_{10} permanently goes through oxidation-reduction cycles while shuttling e^- from Complexes I and II to Complex III in the mETC. Thus, CoQ_{10} is in different oxidative states: it can be completely oxidized and is called CoQ_{10} or ubiquinone, or completely reduced if it receives two e^-, being called $CoQ_{10}H_2$ or ubiquinol. Besides, it can be found as an intermediated product, named semiquinone, semi-ubiquinone or $CoQ_{10}H^{\bullet}$, if this redox cycle occurs by a two-step transfer of one e^- each (Alcazar-Fabra et al., 2016) (**Figure 4**). As a result of these redox state changes, CoQ_{10} rapidly translocates from one side of the IMM bilayer to the other.

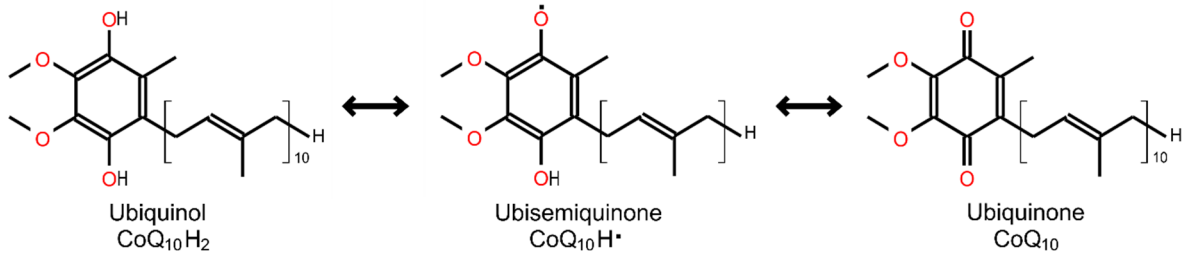

***Figure 4**. The three oxidative states of CoQ_{10}: the fully reduced ubiquinol form ($CoQ_{10}H_2$), the radical semiquinone intermediate ($CoQ_{10}H^{\cdot}$), and the fully oxidized ubiquinone form (CoQ_{10}).*

2.2.1. Coenzyme Q_{10} biosynthesis

The biosynthesis of the CoQ_{10} is mainly controlled by the COQ gene family (Acosta et al., 2016). The resulting COQs' proteins are located in the mitochondrial matrix associated with the IMM and most of them form a protein complex (Marbois et al., 2005; Marbois et al., 2009) (**Figure 5**).

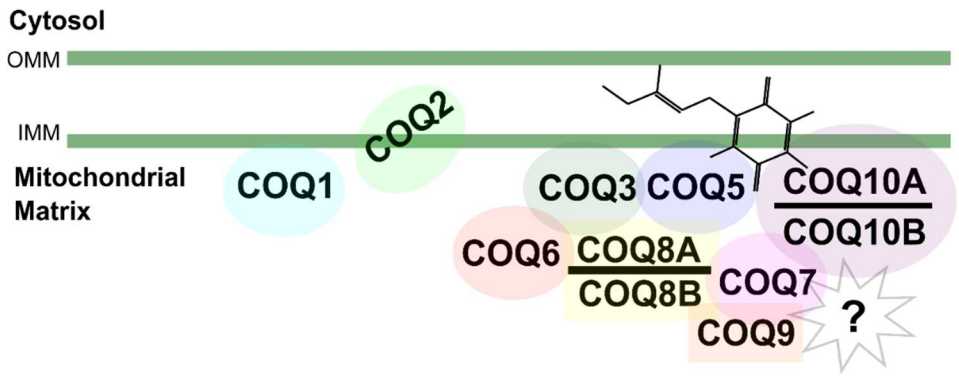

***Figure 5**. Model of the coenzyme Q_{10} biosynthetic complex, containing COQ enzymes (in colored circles and squares) and the Coenzyme Q_{10} itself. COQs enzymes are located in the mitochondrial matrix associated with the inner mitochondrial membrane. The question mark refers to the enzymes involved in the CoQ_{10} biosynthesis process but still are uncharacterized. Abbreviations: IMM = inner mitochondrial membrane; OMM = outer mitochondrial membrane.*

The biosynthesis process starts forming the quinone ring and the polyisoprenoid chain by two independent routes. The precursor of the quinone ring is 4-hydroxybenzoate (4HB) (Olson, R.E., 1983), which is derived from tyrosine, whereas the isoprenoid chain is synthesized via the mevalonate pathway (Olson & Rudney, 1983). The mevalonate pathway, which takes place in the cytosol, starts from acetyl-CoA and ends, after a series of reactions, with the production of farnesyl pyrophosphate (FPP). FPP can then be converted to CoQ_{10}, cholesterol and dolichols, or it can be used for protein farnesylation (Bentinger et al., 2010).

The following steps in CoQ_{10} biosynthesis, in which COQ genes participate, occur in the mitochondrial matrix (**Figure 6**). COQ1 (PDSS1/PDSS2) synthesizes the polyisoprenoid chain, condensing to a benzoquinone ring by COQ2 (Forsgren et al., 2004). COQ3, COQ5, COQ6 and COQ7 are involved in methylation, decarboxylation, hydroxylation and deamination reactions (Tran & Clarke, 2007). COQ8A/COQ8B (also called ADCK3/ADCK4) is a protein kinase necessary for the phosphorylation processes of COQ3 and COQ5 (Stefely et al., 2015; Xie et al., 2011). COQ9 is a lipid-binding protein required to stabilize COQ7 (Lohman et al., 2014) and COQ10A/COQ10B can function as a CoQ_{10} transporter from its synthesis site to the catalytic sites of the complexes of the respiratory chain where it performs its function (Barros et al., 2005). The role of COQ4 is not yet well defined, but it is believed to be necessary for the assembly and stability of the CoQ_{10} biosynthetic complex (Marbois et al., 2009).

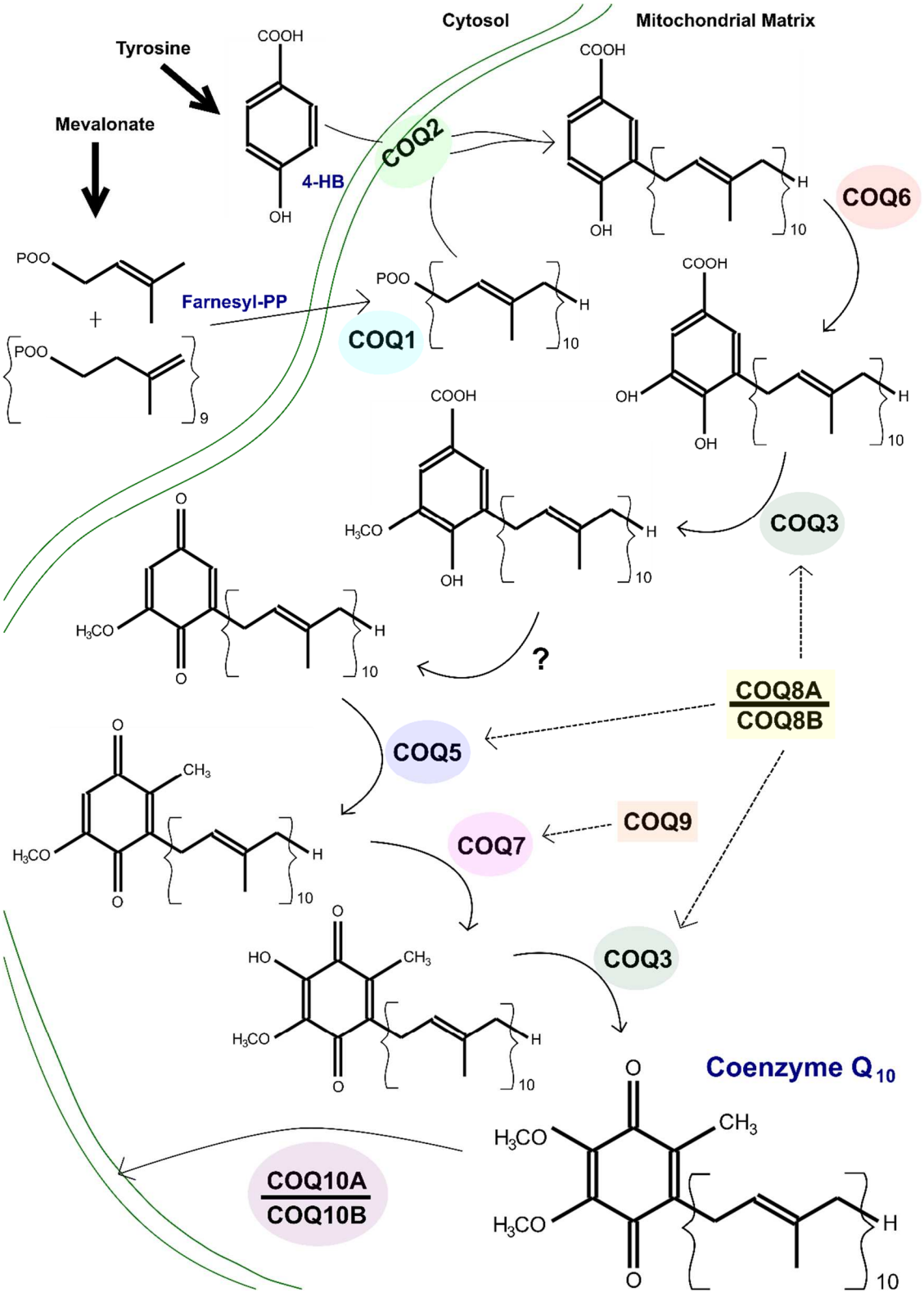

Figure 6. *The coenzyme Q_{10} biosynthetic pathway in humans. The black arrows represent enzymatic reactions and the dotted arrows indicate regulatory mechanisms driven by COQ enzymes (in colored circles and squares). The question mark indicates the still uncharacterized enzymatic step.*

2.2.2. Others Quinones and Hydroxylated forms

The CoQ family consists, apart from CoQ_{10}, of additional analogues, which can also be found in cells, such as CoQ_1 (**Figure 7**).

Additionally, the existence of hydroxylated CoQ (OH-CoQ) derivatives were described in several studies (Bogeski, Gulaboski, et al., 2011; Gulaboski et al., 2013). Concretely, these publications reported that native CoQ_1 and $CoQ_{10,}$ in alkaline media or after exposure to CYP450 enzymes, undergo structural changes and form OH-CoQs, which have different chemical properties than their native forms. They can bind and transfer Ca^{2+} through artificial bio-membranes undergoing reduction and oxidation steps. Moreover, they have more negative redox potentials than the natives forms, and present a relatively pH insensitive redox chemistry. The fact that similar hydroxylated forms are precursors of CoQ_1 and CoQ_{10} during their biosynthesis (Turunen et al., 2004) emphasizes the need to understand the physiological importance of these OH-CoQs in Ca^{2+} signaling and antioxidant defense, and hence their potential pharmacological use.

Focusing on mitochondria, derivatives of $CoQ_{10}H_2$ were promising antioxidants to target mitochondria since the highest amounts of CoQ are found there. However, problems such as low solubility in water and mitochondrial targeting, complicate the use of CoQs *in vitro* and *in vivo*. Therefore, in 2001 Kelso *et al*. synthesized a ubiquinone analogue adding a lipophilic triphenylphosphonium cation (TPP+) which improves the mitochondrial targeting of CoQs (Kelso et al., 2001). Lipophilic cations easily penetrate lipid bilayers and accumulate in mitochondria within cells, driven by the high potential of the mitochondrial membrane. The antioxidant component is the same ubiquinone as found in CoQ_{10} (Tabara et al., 2014); hence in the mitochondrial matrix, the respiratory chain continuously reduces it to its active form and protects the mitochondria from oxidative damage. This analogue was called mitoQ and it was the first mitochondrial antioxidant drug to undergo clinical trials in humans. MitoQ refers to a mixture of two redox forms, the reduced form, mitoquinol, and the oxidized form, mitoquinone (Tabara et al., 2014). In this context, the idea of investigating the physiological and biochemical effects of hydroxylated mitoquinones enabling the identification of new therapeutic targets arises.

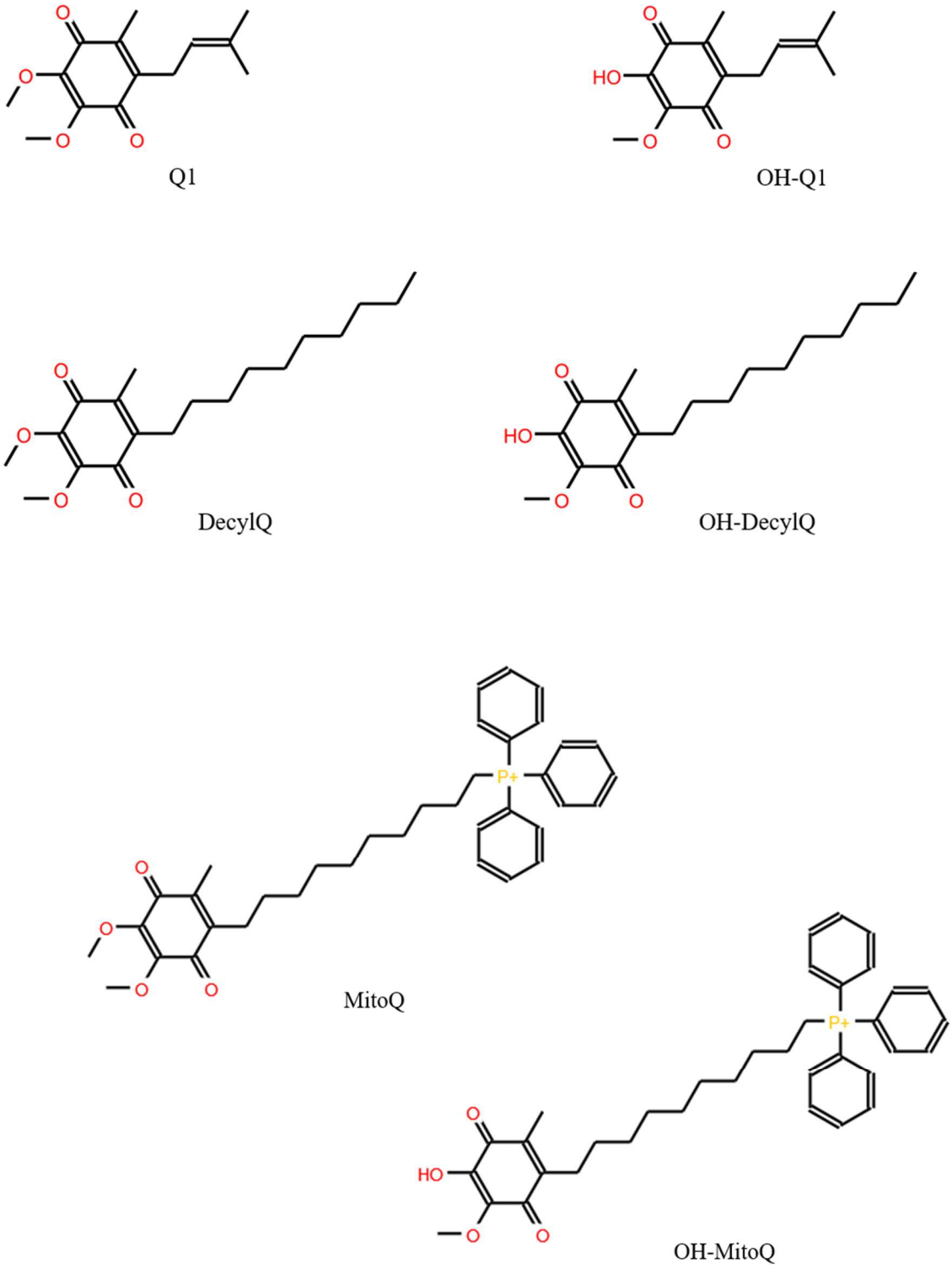

Figure 7. *The schematic representation of Q_1, OH-Q_1, DecylQ. OH-DecylQ, mitoQ and OH-mitoQ chemical structures. In each one, it distinguishes the benzoquinone ring and the lipophilic polyisoprenoid side chain of different lengths depending on the compound. MitoQ and OH-mitoQ also present the lipophilic triphenylphosphonium cation that allows its targeting in the mitochondria.*

2.2.3. Clinical manifestations of CoQ_{10} deficiencies

There is a wide range of clinical manifestations associated with CoQ_{10} deficiency. It has been estimated that 1 in 100,000 individuals is affected by CoQ_{10} deficits worldwide (Hernandez-Camacho et al., 2018). Patients with CoQ_{10} insufficiency have reduced levels of CoQ_{10} in tissues. Low levels are explained either by mutations in the genes encoding proteins of the CoQ_{10} biosynthesis pathway (COQ genes) or its regulation (primary CoQ_{10} deficiencies) (Salviati et al., 1993) or by defects in other mitochondrial functions that are indirectly involved in CoQ_{10} biosynthesis (secondary CoQ_{10} deficiencies) (Yubero et al., 2016).

Primary CoQ_{10} deficiencies are sporadic conditions that are genetically caused by autosomal recessive mutations. These deficiencies usually affect multiple organ systems in a highly variable way, including the central nervous system (CNS), peripheral nervous system (PNS), respiratory system, liver, kidney, skeletal muscle, heart and sensory system (Alcazar-Fabra et al., 2018; Hernandez-Camacho et al., 2018) (**Figure 8**).

Meanwhile, **s**econdary CoQ_{10} deficiencies are more common than primary deficiencies, probably because of the diversity of biological functions and metabolic pathways in which CoQ_{10} is involved. Secondary deficiencies may be due to interferences with the signaling pathways involved in the CoQ_{10} biosynthesis process. They can also be related to side effects of a malfunction of the mETC and a general deterioration of mitochondrial function (Rodriguez-Aguilera et al., 2017). Furthermore, CoQ_{10} levels seem to be reduced in aging (Hernandez-Camacho et al., 2018) and a secondary deficiency of CoQ_{10} may be a side effect of hypercholesterolemia treatment with statins since both cholesterol and CoQ_{10} share part of their biosynthesis pathways (Acosta et al., 2016). Additionally, mutations in genes not related to CoQ_{10} biosynthesis have been reported to cause CoQ_{10} secondary deficiencies. Among them: the aprataxin gene (APTX), which causes ataxia and oculomotor apraxia (Quinzii et al., 2005; Sacconi et al., 2010); the electron-transferring-flavoprotein dehydrogenase gene (ETFDH), which causes isolated myopathy (Gempel et al., 2007; Sacconi et al., 2010) or the BRAF (RAF kinase, isoform B) gene, which causes cardiofaciocutaneous syndrome (Aeby et al., 2007; Sacconi et al., 2010). Moreover, CoQ_{10} deficiency was reported in a patient with mtDNA depletion syndrome (Montero et al., 2009; Sacconi et al., 2010). Although, the connection between these mutations and CoQ_{10} deficiency is unknown.

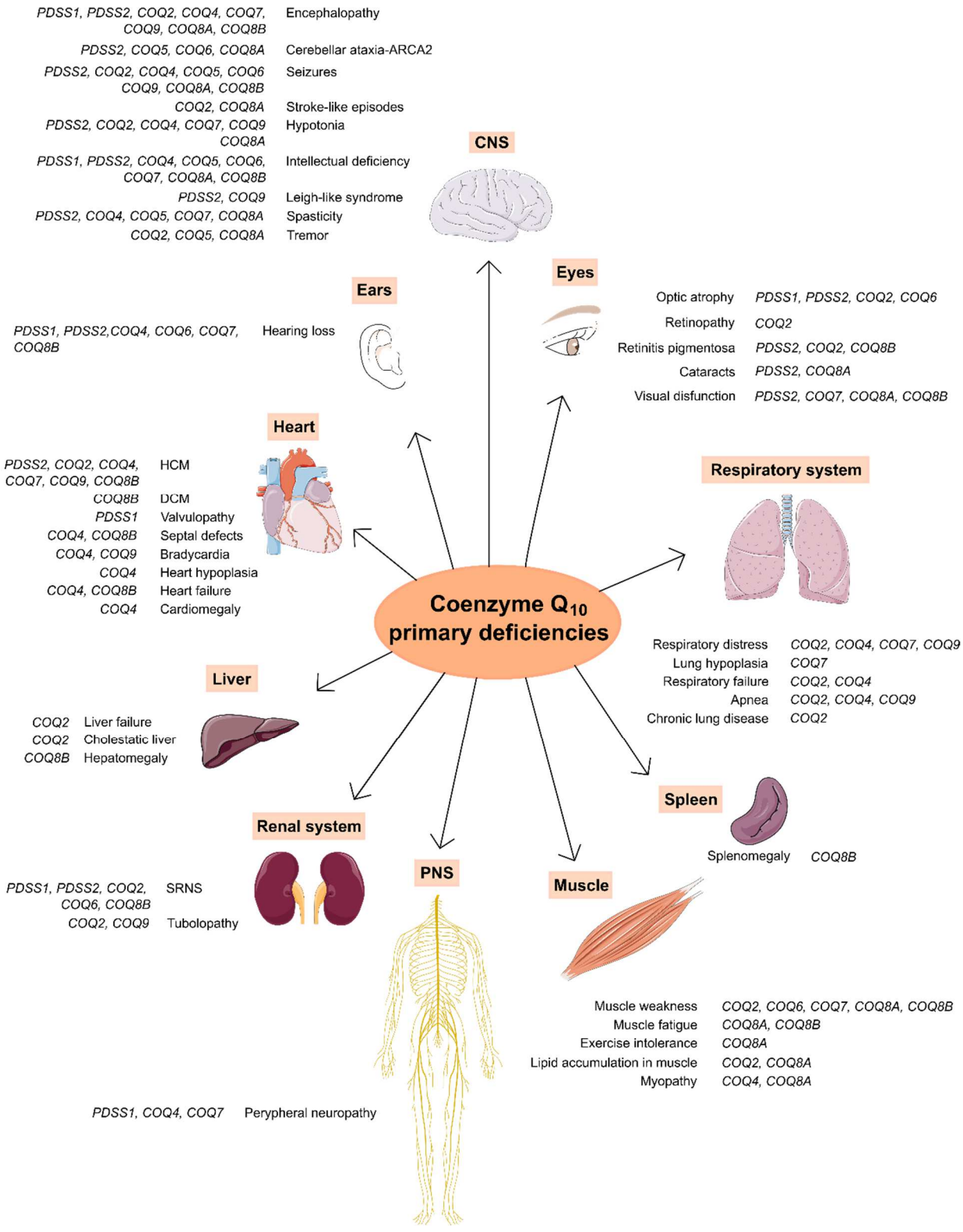

Figure 8. *Organs and systems affected in primary CoQ_{10} deficiencies, specifying clinical manifestations in each one and the genes involved in them. Abbreviations: CNS = central nervous system; PNS = peripheral nervous system. Figure adapted from (Alcazar-Fabra et al., 2018)*

Nevertheless, supplementation of CoQ_{10} in the clinics has been used for a long time. The first successful use of CoQ_{10} was in 1967 when Yuichi Yamamura reported CoQ_{10} as a treatment for congestive heart failure (Greenberg & Frishman, 1990; Singh et al., 2007; Yamamura et al., 1967). Later, the application of CoQ_{10} has been successful in other diseases, such as immunodeficiencies (Mantle et al., 2021), encephalomyopathy or ataxia (Hirano et al., 2006), Parkinson's and Huntington's disease (Yang et al., 2009), cancer (Brea-Calvo et al., 2006) and diabetes (Shen & Pierce, 2015).

Beneficial effects have also been reported in softening the side effects of statins (Crane, 2007). More specifically, ubiquinol, the reduced form of CoQ_{10}, was recently approved as a drug in case of primary CoQ_{10} deficiency; by contrast, some patients with a secondary CoQ_{10} deficiency showed no clinical relief (Rodriguez-Aguilera et al., 2017). These controversial observations, gained by CoQ_{10} derivate as supplements in the clinics, highlight the importance of investigating their biosynthesis, function and role in human pathology in more detail.

2.3. CALCIUM AND REACTIVE OXYGEN SPECIES

2.3.1. Calcium homeostasis and signaling

Calcium ions (Ca^{2+}) are essential signaling molecules implicated in the regulation of diverse cellular functions, such as cell differentiation, gene expression, proliferation, muscle contraction, protein folding, energy metabolism, and cell death (Berridge, 2012; Berridge et al., 2003; Bravo-Sagua et al., 2017).

The low resting cytosolic Ca^{2+} ($cytCa^{2+}$) concentration and Ca^{2+} signaling have to be strictly regulated since any deregulated increase in $cytCa^{2+}$ would cause cell damage or even cell death (Hajnoczky et al., 2006). Furthermore, the regulation of the functions of specific organelles depends on the propagation of the $cytCa^{2+}$ signal, such as the nucleus for gene regulatory events (Bagur & Hajnoczky, 2017; Zhang et al., 2009), and the mitochondria for oxidative metabolism (Bagur & Hajnoczky, 2017; Griffiths & Rutter, 2009).

The intracellular free Ca^{2+} is highly variable depending on its location. For example, $cytCa^{2+}$ concentration is $\sim 10^{-7}$ M under resting conditions, while Ca^{2+} concentration in the extracellular medium is $\sim 10^{-3}$ M. Within the cell, Ca^{2+} levels in the nuclear matrix (nCa^{2+}) and in the mitochondrial matrix (mCa^{2+}) resemble those of the cytosol. However, in intracellular Ca^{2+}

stores, a much higher Ca^{2+} concentration can be accumulated (1-5 × 10^{-4} M). The main Ca^{2+} store in non-excitable cells is the endoplasmic reticulum (ER) and, in excitable cells the sarcoplasmic reticulum (SR) (Bagur & Hajnoczky, 2017).

In a resting cell, cytCa^{2+} remains in an optimal range thanks to the action of the plasma membrane Ca^{2+} transport ATPase (PMCA) and the Na^{+}/Ca^{2+} exchanger (NCX). When cytCa^{2+} increases, it can be stored in the ER/SR via Ca^{2+}-ATPase (SERCA) or can enter the mitochondria via voltage-dependent anion channels (VDAC) (cytosol to IMM) and the mitochondrial Ca^{2+} uniporter (MCU) complex (IMM to matrix). In this way, a homeostatic control of cytCa^{2+} is achieved (**Figure 9**).

Nevertheless, cellular stimuli such as membrane depolarization, extracellular signaling molecules or intracellular messengers generate a greater than 10-fold increase in cytCa^{2+} concentration. This increase occurs by the entry of extracellular Ca^{2+} via the Ca^{2+} channels of the plasma membrane or by the release of Ca^{2+} from the ER/SR via the inositol 1,4,5-triphosphate receptor (IP_3R) and the ryanodine receptor (RyR) (**Figure 9**).

Each cell type demands a particular Ca^{2+} signaling to adapt to its physiological requirements and it presents a specific combination of Ca^{2+} channels and pumps that make them unique. (Berridge et al., 2000). These Ca^{2+} channels and pumps possess different activity thresholds, namely, the PMCA and SERCA pumps have high affinities for Ca^{2+} and a low pumping rate (Juhaszova et al., 2000), whereby they respond to small increases in cytCa^{2+}, restoring the levels. In comparison, NCX and MCU have a lower affinity for Ca^{2+} and higher transport rates (Boyman et al., 2009) and thus can limit more strictly cytCa^{2+} transients.

Additionally, although the general amplitude of cytCa^{2+} concentration reaches a maximum of around 10^{-6} M near the open Ca^{2+} channels, a 10-100 × 10^{-3} M concentration can be achieved. This substantial local Ca^{2+} increase activates Ca^{2+} detection motifs of proteins with low affinity for Ca^{2+}, which do not respond to fluctuations in the global cytCa^{2+} levels. An example is a mechanism known as storage-operated Ca^{2+} entry (SOCE), the main Ca^{2+} signaling pathway in non-excitable cells (Parekh & Putney, 2005; Putney, 1986, 1990). This influx of Ca^{2+} occurs through the plasma membrane, after a decrease in Ca^{2+} content from the ER. The primary function of SOCE is to refill the intracellular Ca^{2+} stores to maintain the balance of cellular Ca^{2+}. The process begins when stromal interaction molecule 1 (STIM1) (and its isoform STIM2), a transmembrane protein that is located in the ER, detects a decrease in Ca^{2+} concentration in the endoplasmic reticulum (ER Ca^{2+}) (Liou et al., 2005; Roos et al., 2005;

Zhang et al., 2005). Under resting conditions, Ca^{2+} is bound to a pair of EF-hand domains of STIM1. However, when the Ca^{2+} content of the ER lumen drops, Ca^{2+} dissociates from the STIM1 EF-hands domains (Bagur & Hajnoczky, 2017). As a result, STIM1 unfolds, oligomerizes and translocates to specific ER regions near the plasma membrane (named ER-PM junctions), where it interacts with and activates the plasma membrane Ca^{2+} channel calcium release-activated calcium channel protein 1-3 (Orai 1-3) (Schindl et al., 2009). Thus, defining the Ca^{2+} release-activated Ca^{2+} (CRAC) channels (**Figure 9**) (Bagur & Hajnoczky, 2017).

During SOCE, mitochondria take up Ca^{2+} by the MCU complex (**Figure 10**). The elevated mCa^{2+} enhances the activity of critical enzymes of the TCA and leads to the activation of mitochondrial dehydrogenases, resulting an increase in NADH production and OXPHOS. This in turn causes the greater proton motive force that maintains the $m\Delta\Psi$ and consequently, there is an increase in ATP production (Parekh & Putney, 2005). Thus, mCa^{2+} uptake plays a critical role in matching ATP production to an increased demand and enhancing the generation of antioxidants.

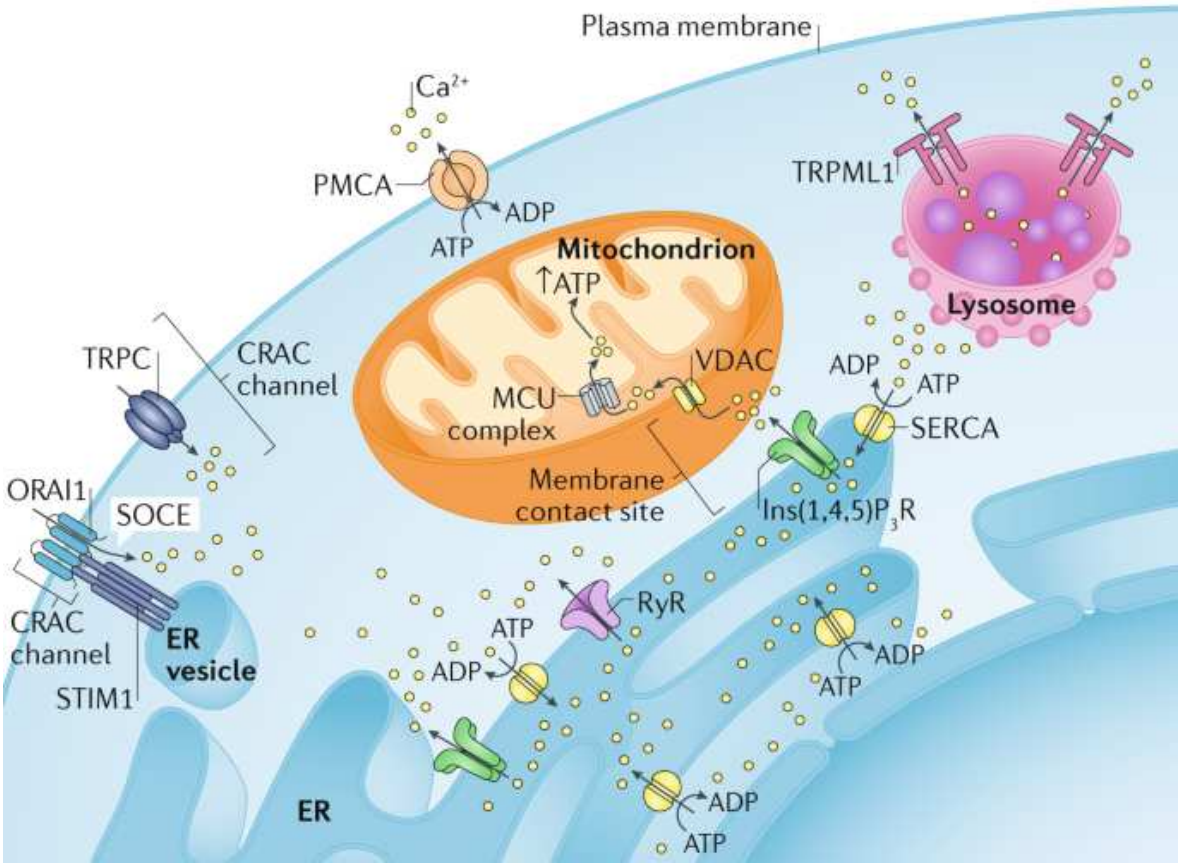

***Figure 9**. Intracellular Ca^{2+} signaling. The sarcoplasmic / endoplasmic reticulum Ca^{2+} ATPases (SERCA) pumps Ca^{2+} to the endoplasmic reticulum (ER) which is the main intracellular Ca^{2+} store. The ryanodine receptors (RyR) and the inositol 1,4,5-triphosphate receptors (Ins (1,4,5) P3R) mediate the release of Ca^{2+} from the ER. Ca^{2+} is then taken up by neighboring mitochondria through voltage-gated anion-selective channel proteins (VDAC; in the mitochondrial outer membrane) and the mitochondrial Ca^{2+} uniporter complex (MCU; in the inner mitochondrial membrane), leading to ATP production. Depletion of ER Ca^{2+} stores leads to activation of the Ca^{2+} sensing protein stromal interaction molecule 1 (STIM1; in the ER), which binds and activates the Ca^{2+} channel protein Ca^{2+} release-activated Ca^{2+} channel protein 1 (ORAI1; in plasma membrane) working as a Ca^{2+} release-activated Ca^{2+} channel (CRAC) for store-operated Ca^{2+} entry (SOCE). Transient receptor potential channels (TRPC) also mediates the entry of Ca^{2+} into the cell as CRACs. Ca^{2+} export from the cytosol is mediated by plasma membrane Ca^{2+} ATPases (PMCA), maintaining the intracellular Ca^{2+} concentration at adequate values for correct cell signaling. In addition to ER, lysosomes store Ca^{2+} and it can be released through TRPC mucolipin 1 (TRPML1).). Abbreviations: ADP = adenosine diphosphate; ATP = adenosine triphosphate; Ca^{2+} = calcium ions; CRAC = the Ca^{2+} release-activated Ca^{2+}; ER = endoplasmic reticulum; Ins(1,4,5)P3R = inositol 1,4,5-triphosphate receptors; MCU = mitochondrial Ca^{2+} uniporter; PMCA = plasma membrane Ca^{2+} ATPases; ORAI1 = calcium release-activated calcium channel protein 1; RyR = ryanodine receptor; SERCA = sarcoplasmic / endoplasmic reticulum Ca^{2+} ATPases; STIM1 = stromal interaction molecule 1; SOCE = storage-operated Ca^{2+} entry; TRPC = Transient receptor potential channels; TRPML1 = TRPC mucolipin 1; VDAC = voltage dependent anion-selective. Image taken from (Giorgi et al., 2018).*

2.3.1.1. Mitochondrial Calcium Uniport Complex

The MCU complex resides in the IMM and, as mentioned before, it is necessary to facilitate Ca^{2+} uptake into the mitochondrial matrix (**Figure 10**). The large electrochemical gradient (-80 mV) generated by mETC across the IMM drives Ca^{2+} flux through the MCU complex.

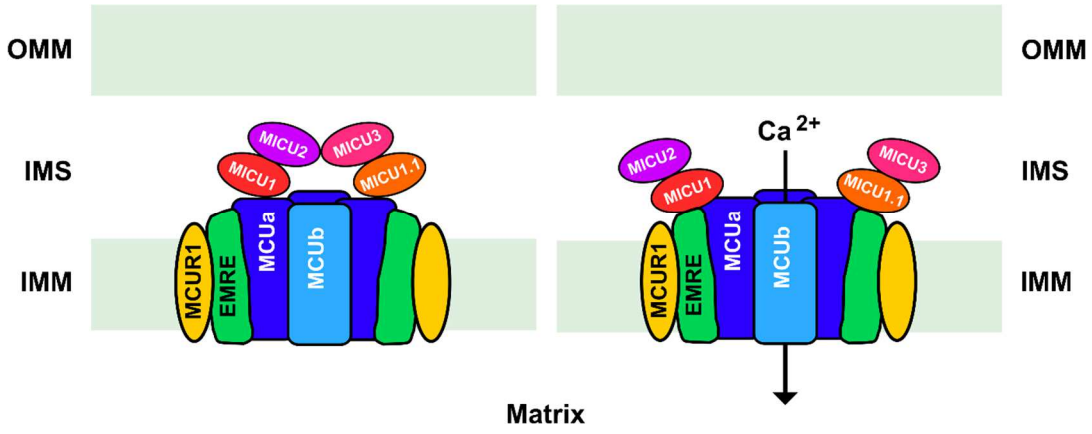

Figure 10. *Schematic representation of the MCU complex. On the left, the complex keeps the pore closed, on the right the pore is open allowing the flow of calcium ions to the mitochondrial matrix. Abbreviations: Ca^{2+} = calcium ions; EMRE = essential MCU regulator; MCUa and b = mitochondrial calcium uniporter a and b; MCUR1 = mitochondrial calcium uniporter regulator 1; MICU1-3 = mitochondrial calcium uptake 1-3, IMM = inner mitochondrial membrane; IMS = intermembrane space; OMM = outer mitochondrial membrane.*

MCU complex is a multiprotein complex composed of mitochondrial calcium uniporter a and b (MCUa and MCUb), the channel-forming subunits, along with essential MCU regulator (EMRE), mitochondrial calcium uptake 1, 2 and 3 (MICU1, MICU2 and MICU3) and mitochondrial calcium uniporter regulator 1 (MCUR1).

MCUa (often called just MCU) are believed to form homo-oligomers, with a highly conserved 'DIME' sequence motif serving as a Ca^{2+} selectivity filter and the transmembrane domains that form a hydrophilic pore crossing the IMM, which allows the entry of Ca^{2+}. Loss of MCUa completely abolishes all channel functions, leading to a lack of mCa^{2+} uptake. MCUb is a similar protein and shares 50 % homology to MCUa. MCUb alters the assembly of the complex by changing the stoichiometry of mitochondrial Ca^{2+} subunits, inhibiting Ca^{2+} entry (Lambert et al., 2019). MICU1, MICU2 and MICU3 form heterodimers, which under resting conditions act as MCU gatekeepers, thanks to the dominating inhibitory effect of MICU2, thus preventing vicious Ca^{2+} cycles. As soon as Ca^{2+} signaling is induced, the increase in Ca^{2+} concentration in the IMS causes a conformational change in MICUs dimer leading to the release of the MICU2-dependent inhibition and triggering a rise of MCU activity aided by MICU1 and MICU3 (De Stefani et al., 2015). EMRE was defined as an essential MCU regulator based on studies that determined that the necessary channel components for proper MCU complex operation are

MCU and EMRE. Besides, EMRE controls MICUs interactions with MCU and, therefore, may also indirectly contribute to channel gating (Liu et al., 2020). MCUR1 has been identified as another component that regulates the role of MCU; it is believed to form a scaffold for channel formation (Mallilankaraman et al., 2012).

It has been estimated that the IMM contains 10 - 40 MCU channels per μm^2 and MCU complex is activated by Ca^{2+} concentrations around 1 µM depending on the cell type (Petrungaro et al., 2015).

2.3.2. Reactive Oxygen Species and redox signaling

ROS are the most common oxidants in cells and are generated when O_2 is reduced to superoxide ($O_2^{-\bullet}$), hydrogen peroxide (H_2O_2), hydroxyl ($HO^{\bullet}$), peroxyl radicals ($ROO^{\bullet}$) etc (Gaschler & Stockwell, 2017).

ROS were initially considered toxic products that damage cellular structures and cause oxidative stress (Holmstrom & Finkel, 2014). However, it is presently accepted that ROS act as important messengers in many cellular signaling cascades (Casas et al., 2015; Jezek & Hlavata, 2005).

Oxidative stress occurs when the production of ROS exceeds the defense provided by the antioxidant systems. Indeed, when in excess, ROS can trigger different signaling cascades and pathways, contributing to various cardiovascular (Takano et al., 2003), neurological or metabolic pathologies (Lemire & Appanna, 2011; Piconi et al., 2003) or cancer (Thanan et al., 2014).

In contrast, ROS are also required as regulators of cell metabolism (Jezek & Hlavata, 2005). In this regard, they function as signaling molecules that regulate essential physiological processes such as cell proliferation and differentiation, vascular tone, the innate immune response and inflammation (Casas et al., 2015; Holmstrom & Finkel, 2014).

Mitochondria are thought to be the major source of ROS in most cell types (Murphy, 2009). Accordingly, mitochondrial ROS (mROS) production is tightly connected with mCa^{2+}. In particular, mitochondria produce $O_2^{-\bullet}$ at Complexes I, II and III of mETC (Murphy, 2009). The $O_2^{-\bullet}$ produced at Complex I is believed to be released only within the matrix, whereas at Complex III, $O_2^{-\bullet}$ is discharged both into the matrix and into the IMS (Finkel, 2011).

Mitochondrial ΔΨ is also thought to influence mROS production. An increase in the proton motive force is associated with elevated ROS production, whereas a decrease leads to a reduction in generated ROS (Mailloux & Harper, 2012). This is based on the fact that a high proton motive force slows down the flow of e^- along the mETC. This deceleration of e^- increases the probability that a free e^- will interact with O_2, leading to the production of $O_2^{-\bullet}$ (Holmstrom & Finkel, 2014).

Other contributors to the generation of mROS include metabolic enzymes. Some of them can be found in the OMM, e.g., monoamine oxidase and cytochrome b5 reductase (Cb5R), whereas other are located in the IMM, e.g., glycerol-3-phosphate dehydrogenase (GPDH) and electron transfer flavoprotein-ubiquinone oxidoreductase (FQR) system. There are also several matrix enzymes and complexes, including PDH and α-ketoglutarate dehydrogenase (αKGDH) that can generate $O_2^{-\bullet}$ (Finkel, 2011; Lin & Beal, 2006).

ROS are generated by other cellular sources. One major source for intracellular oxidant production is the family of NADPH oxidases which are membrane-bound enzymes that transfer e^- from cytosolic NADPH to O_2 to produce $O_2^{-\bullet}$. This group of enzymes, known as NOX enzymes, is composed of seven-members (Nox1–5 and Duox1–2) and their activity is also depended of Ca^{2+} (Bedard & Krause, 2007; Dikalov, 2011; Finkel, 2011; Saul et al., 2016).

In addition, intracellular enzymes such as the xanthine oxidase, cyclooxygenases, cytochrome p450 enzymes and lipoxygenases produce ROS as part of their normal enzymatic function. Furthermore, cell organelles, such as the peroxisomes and the ER can also generate ROS (Finkel, 2011; Holmstrom & Finkel, 2014).

2.3.2.1. Antioxidant systems

All biological systems are in redox homeostasis keeping a balance between oxidative and reducing reactions. The accumulation of oxidant molecules, causing failures in redox homeostasis, can lead to disease or even death. Excessive production of oxidants can occur either by overproduction or by a loss in the cellular reduction capacity. In both cases, generated oxidizing agents can oxidize DNA, proteins and lipids, thus altering their structure, activity, and physical properties (Jezek & Hlavata, 2005). To combat the harmful effects of ROS and the aberrant production of oxidized biomolecules, cells have developed antioxidant mechanisms (Holmstrom & Finkel, 2014).

The $O_2^{-\bullet}$ generated by mitochondria is rapidly converted to H_2O_2 by the enzymatic activity of either manganese (Mn) or copper/zinc (Cu/Zn)-dependent superoxide dismutase (SOD), which are located in the mitochondrial matrix and the IMS, respectively (Fridovich, 1997; Holmstrom & Finkel, 2014; Mailloux & Harper, 2012).

The generated H_2O_2 is far more stable than $O_2^{-\bullet}$ and can cross membranes. H_2O_2 is hence, the main ROS involved in cell signaling. To this end, H_2O_2 can control intracellular signaling pathways by reversibly oxidizing cysteine residues in key proteins (Bogeski et al., 2010; Gibhardt et al., 2020). However, H_2O_2 can also cause oxidative stress; thus, a number of enzymes such as glutathione peroxidases (GPx), peroxiredoxins (PRDX), thioredoxins (TRX), and glutaredoxins (GRX) can scavenge H_2O_2. Catalase (CAT) is another enzyme that can also degrade H_2O_2 (Finkel, 2011; Holmstrom & Finkel, 2014; Mailloux & Harper, 2012).

Furthermore, (as already depicted in chapter **2.2**) CoQ_{10} is a very important antioxidant in the IMM but also in other cellular membranes.

2.4. FERROPTOSIS

Ferroptosis is a recently described form of regulated cell death (Dixon et al., 2012). It is characterized by an iron-mediated cell death, caused by the accumulation of lipid peroxidation products in membranes. Ferroptosis appears to be completely different from other forms of regulated cell death, such as apoptosis, necrosis and autophagy, in terms of morphology, biochemistry and genetics (Doll & Conrad, 2017). Nevertheless, recent studies have shown that ferroptosis plays an essential regulatory role in the onset and development of nervous system disease, heart disease, liver disease, gastrointestinal disease, lung disease, kidney disease, pancreatic disease and more (Li et al., 2020). Therefore, a better understanding of its pathogenesis is necessary for proposing new targets for the treatment and improvement of the prognosis of these diseases. To this end, CoQ_{10} has been suggested as an inhibitor of lipid peroxidation and consequently, a suppressor of ferroptosis (Jiang et al., 2021).

2.4.1. Lipid peroxidation

Lipid peroxidation (LPO) is a sequence of devastating oxidative reactions in which free radicals attack unsaturated fatty acids in membranes of cellular or subcellular compartments (Yin et al., 2011).

The toxic effects of lipid peroxides may be due to two general mechanisms. On the one hand, extensive LPO alters their assembly, composition, structure and dynamics and leads to a disruption of cell membranes. On the other hand, being highly reactive compounds, lipid peroxides can also propagate a more significant generation of ROS or degrade into reactive compounds capable of cross-linking DNA and proteins.

LPO occurs mainly in polyunsaturated fatty acids (PUFA). They are long-chain fatty acids with more than one double bond. Oxidation of PUFAs can be a non-enzymatic or enzymatic process.

The non-enzymatic peroxidation of lipids is a process that can be divided into three phases: initiation, propagation, and termination (**Figure 11**).

In the **initiation** step, free radicals abstract the allylic hydrogen of a fatty acid molecule, forming a lipid radical and water.

In the **propagation** phase, the lipid radical reacts rapidly with O_2 to form a lipid peroxyl radical ($ROO^{\bullet}$), which can subtract a hydrogen atom from another lipid molecule generating a new lipid radical and a lipid hydroperoxyl (ROOH). Thus, radical compounds can give rise to new radicals, causing a chain reaction.

In the **termination** reaction, if the concentration of radicals is high enough that two radicals can react, they will form a new chemical bond between them and eliminate the radical. Alternatively, antioxidants could donate one hydrogen atom to the $ROO^{\bullet}$ species resulting in the formation of non-radical products and thus, stop the radical's propagation. These antioxidants are the central defence mechanism against uncontrolled LPO and other oxidative damage (Ayala et al., 2014; Gaschler & Stockwell, 2017).

The enzymatic peroxidation of PUFAs can be carried out by two different groups of enzymes. PUFAs esterified with phospholipids can only be oxidized by lipoxygenases. In contrast, free fatty acids can be oxidized by lipoxygenases, cyclooxygenases and by cytochrome P450 (Gaschler & Stockwell, 2017).

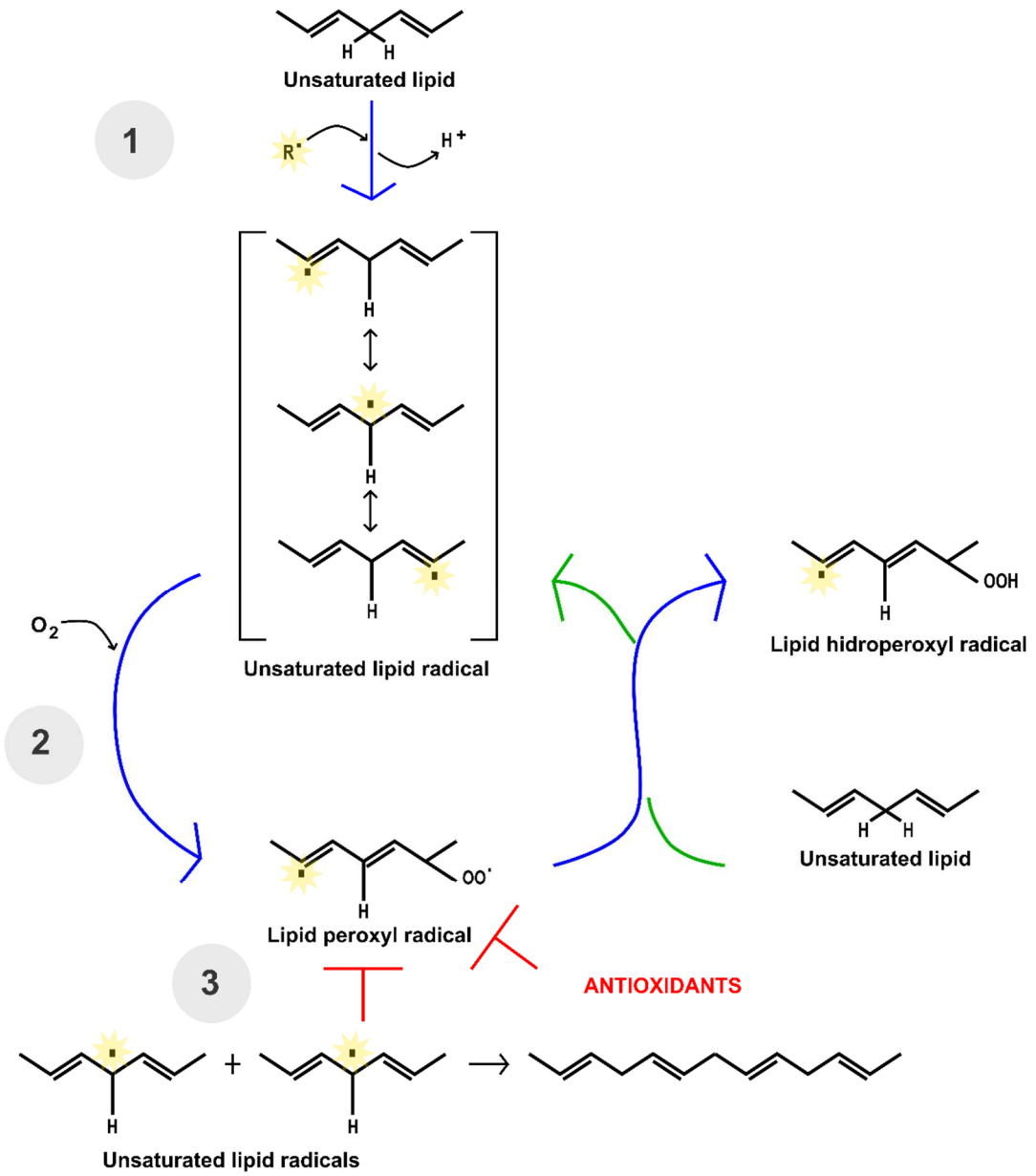

Figure 11. *Lipid peroxidation process. (1) The Initiation step: lipid radicals are formed when free radicals take the allylic hydrogen from fatty acids. These lipid radicals are stabilized in different resonance structures by delocalization of the free electron. (Brastianos et al.) The Propagation phase: Peroxyl lipid radicals are formed after lipid radicals react with oxygen. The new lipid peroxyl radicals may abstract a hydrogen from another lipid molecule, which create a new lipid radical and lipid hydroperoxide. (3) The Termination step: two lipid radicals react with each other to form a stable bond. Antioxidants also stop de reaction donating a hydrogen atom to the lipid peroxy radical species, which generate non-radical products. Abbreviations:* H^+ *= proton;* O_2 *= molecular oxygen;* $R^\bullet$ *= free radical.*

2.4.2. Lipid peroxidation in ferroptosis

In 2012, Dixon *et al*. used the term "ferroptosis" for the first time (Dixon et al., 2012). Name that comes from Greek word "ptosis" meaning "a fall" and ferrum, which is iron in Latin, suggesting the significance and repercussion of this metal in this kind of cell death (Doll & Conrad, 2017). A certain amount of iron is essential for proper cellular metabolism. Most cellular iron is bound to heme, bound in FeS clusters, or stored in the iron storage protein ferritin. However, there is a small amount of iron that is loosely bound, named "labile". Cells harbour a labile redox-active iron pool in the cytosol, mitochondria and lysosomes (Amoretti et al.). Labile iron acts as a pro-oxidant in ferroptosis through a series of redox reactions known as "Fenton chemistry" (**Figure 12**). Radical compounds generated in these reactions attack unsaturated fatty acids and cause LPO. Hence, it is crucial to maintain the pools in an optimal range concentration (0.5 – 5.5 µM) (Cabantchik, 2014).

In the first step of Fenton chemistry, a hydroxide anion and a highly reactive hydroxyl radical are generated by the formation of ferric iron from the oxidation of ferrous iron by H_2O_2. Ferric iron can be reduced to its ferrous state and create a hydroperoxyl radical if another H_2O_2 is available. Besides, the union of two H_2O_2 generates hydroxyl and hydroperoxyl radicals. These generated radicals act in the initiation phase of LPO. (Doll & Conrad, 2017).

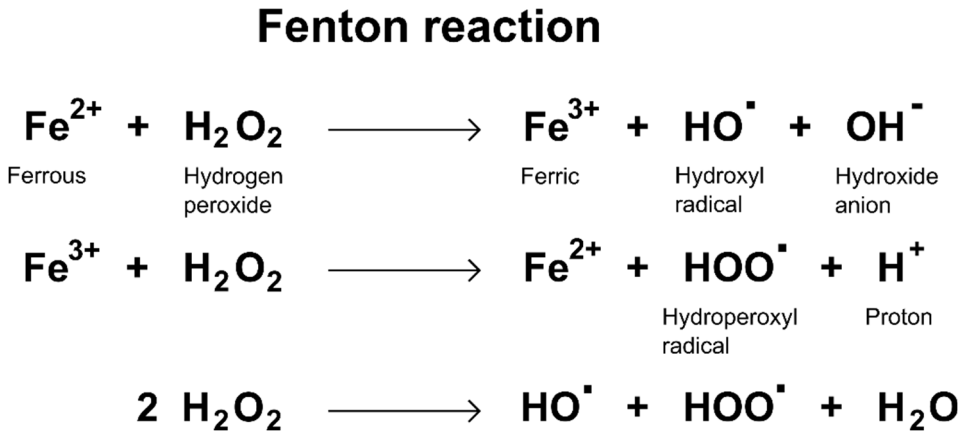

***Figure 12**. Fenton reaction. Ferrous ion reacts with hydrogen peroxide to produce the hydroxyl radical (HO•). Ferric ion from the previous reaction can be reduced back to ferrous iron in the presence of superoxide and generate hydroperoxyl radical. Two hydrogen peroxide can generate hydroxyl and hydroperoxyl radicals.*

2.4.3. Regulation of Ferroptosis

2.4.3.1. Glutathione-dependent pathway

Until recently, ferroptosis was thought to be controlled only by a glutathione-dependent pathway (Yang et al., 2014) (**Figure 13**), in which glutathione peroxidase 4 (GPX4) is the main regulator. GPX4 prevents ferroptosis by reducing ROOH into non-toxic lipid alcohols through the following reaction (**Figure 14**) (Yang et al., 2014):

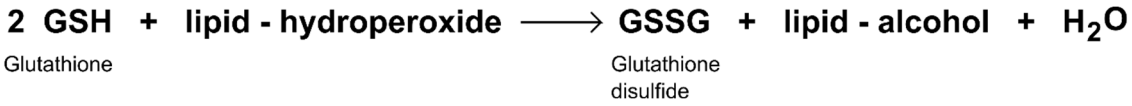

Figure 14*. Two reduced Glutathione molecules are converted to an oxidized Glutathione disulfide molecule reducing lipid hydroperoxides to the corresponding alcohol and producing water. This reaction inhibits the oxidative stress induced ferroptosis.*

Another critical part of this pathway is the availability of cysteine/cystine since it is necessary for glutathione synthesis. Cysteine is transported into cells via neutral amino-acid transport systems, whereas cystine, the oxidized form and the predominant in the extracellular space, is carried by the cystine/glutamate antiporter (Sx_c^-) system (Bannai & Tateishi, 1986).

Glutathione (GSH) is synthesized in the cytosol by two enzymes, glutamate-cysteine ligase (GCL), composed of catalytic and modifier subunits (GCLC and GCLM) and GSH synthetase. Both steps are dependent on ATP. Then, GSH is distributed to the nucleus, the ER and the mitochondria, constituting the major cellular antioxidant system GSH / GSSG (Lu, 2013)**.**

Hence, the cystine uptake by Sx_c^-, synthesis of GSH and proper functioning of GPX4 are key cellular processes suppressing ferroptosis.

Small-molecule compounds can be inducers of ferroptosis (FINs) by interfering with the protective effect of this pathway. Among them, erastin, a small molecule identified by Dixon *et al*. that blocks Sxc-, and hence depriving the cell of cysteine and inhibiting the synthesis of GSH (Dixon et al., 2014); RAS-selective lethal (RSL3) that can triggers ferroptosis blocking

GPX4 activity (Yang & Stockwell, 2008); and buthionine sulfoximine, which inhibits the enzyme GCL, prevents the production of GSH from cysteine (Guo et al., 2009).

2.4.3.2. FSP1–CoQ_{10}–NAD(P)H pathway

In 2019 another regulatory axis was proposed to play a central role in ferroptosis. The FSP1–CoQ_{10}–NAD(P)H pathway (**Figure 13**) suppresses LPO and ferroptosis in cooperation with GPX4 and GSH, but in an independent manner (Bersuker et al., 2019; Doll et al., 2019).

Ferroptosis suppressor protein 1 (FSP1) was known as AIFM2 (apoptosis-inducing factor mitochondrial 2), based on its homology to the mitochondrial apoptosis-inducing factor (AIF or AIFM1). However, FSP1 lacks the N-terminal mitochondrial targeting sequence of AIF, is not found in mitochondria and does not trigger apoptosis. Instead, FSP1 is localized at the plasma membrane, where it mediates the NADH-dependent reduction of CoQ_{10} to ubiquinol-10 ($CoQ_{10}H_2$) (**Figure 15**).

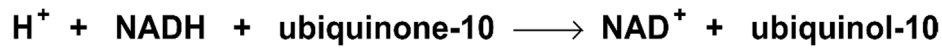

Figure 15*. Reduction of ubiquinone-10 to ubiquinol-10 dependent of NADH and H^+ with the consequent production of NAD^+. NAD^+ = oxidized nicotinamide adenine dinucleotide; NADH = reduced nicotinamide adenine dinucleotide; H^+ = proton; NAD^+ = oxidized nicotinamide adenine dinucleotide; NADH = reduced nicotinamide adenine dinucleotide.*

CoQ_{10} acts as radical-trapping antioxidant inhibiting LPO by preventing the production of $ROO^{\bullet}$ and reduced CoQ_{10} supresses the initial $FeO^{\bullet}/FeOO^{\bullet}$, with concomitant formation of ubisemiquinone. This quenching of radicals prevents the propagation of LPO.

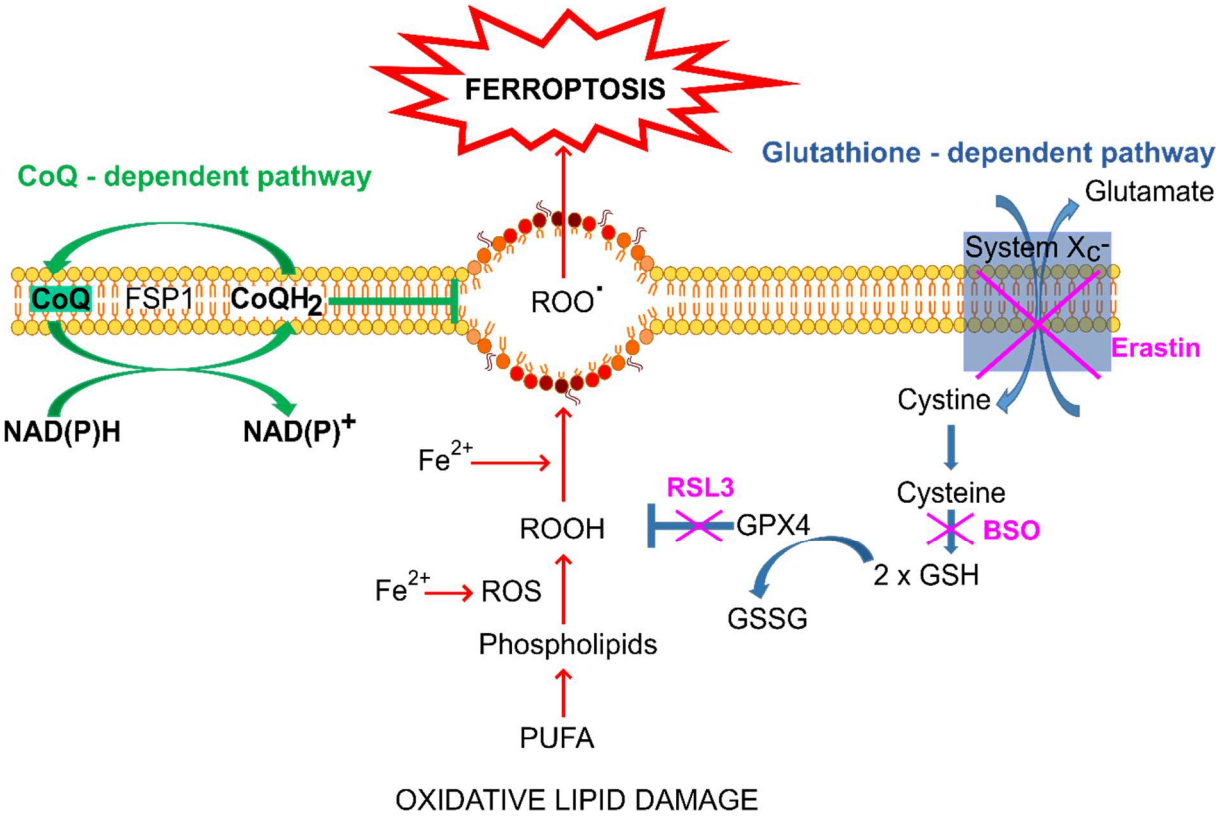

Figure 13. *Graphic scheme representing the oxidative lipid damage (in red) and the anti-ferroptotic function of CoQ (in green) as a suppressor of phospholipid peroxidation independent of the glutathione pathway (in blue). Also depicted (in pink) the reactions where the drugs BSO and Erastin act and block the anti-ferroptotic effect of glutathione. Abbreviations: BSO = buthionine sulfoximine; CoQ = Coenzyme Q; $CoQH_2$ = reduced Coenzyme Q; Fe^{2+} = Ferrous iron; FSP1 = Ferroptosis suppressor protein 1; GPX4 = glutathione peroxidase 4; GSH = glutathione; GSSG= Glutathione disulphide; $ROO^{\bullet}$ = lipid peroxyl radical; ROOH = lipid hydroperoxyl radical; $NAD(P)^{+}$ = oxidized nicotinamide adenine dinucleotide (phosphate); NAD(P)H = reduced nicotinamide adenine dinucleotide (phosphate); PUFA = polyunsaturated fatty acid; ROS = reactive oxygen species; Xc System = cystine/glutamate antiporter.*

2.5. ROLE OF CoQ_{10} AND THE IMPORTANCE OF FERROPTOSIS IN CARDIOMYOPATHY

Cardiovascular diseases (CVDs) are the leading cause of death in the world, taking an estimated 17.9 million lives each year (2021 WHO). Interestingly, patients with CoQ_{10} deficiency often have heart related pathologies; moreover, around 75 % of all heart disease patients present low levels of CoQ_{10} (Zozina et al., 2018). For example, in patients with ischemic heart disease and dilated cardiomyopathy, the CoQ_{10} content has been found to be much lower than in healthy patients. Furthermore, depending on the severity of the cardiomyopathy, this decrease is directly proportional to the progression of the disease (Kumar et al., 2009; Zozina et al., 2018). Various theories have been proposed about the role of CoQ_{10} in CVDs.

Firstly, for its antioxidant function against ROS and free radicals in biological membranes as mentioned above. The reduced form of CoQ_{10}, ubiquinol, has its full function as an antioxidant, preventing the serious cellular damage that ROS produces by reacting with cell membranes, DNA, and proteins. Moreover, oxidative stress products and cytokines can cause hypertrophy by triggering myocyte growth (Nakagami et al., 2003). In addition, ferroptosis is discovered in CVDs more recently and ubiquinol stops the initial process of LPO avoiding ferroptotic cell death (Zhai et al., 2021).

Secondly, CoQ_{10} plays an important role in the energy needs of the heart since it is a main component in the transport of e^- necessary for the production of ATP. For instance, the cardiac contraction process, which involves the release of Ca^{2+} from the SR and its binding to troponin C in myofilaments to cause cardiomyocytes to contract, requires a large contribution of energy from the mitochondria (Kai et al., 2005; Schaub & Kunz, 1986). Furthermore, a possible cause of myocardial insufficiency is a low energy production in the mitochondria (Kumar et al., 2009).

In addition to that, recent studies attribute anti-inflammatory properties to CoQ_{10} possibly through the regulation of nitric oxide (Jung et al., 2009). This mechanism can be effective in the treatment of CVDs, since some of them, for example heart failure (Palty et al.), are related to a chronic pro-inflammatory state. Therefore, the secretion of cytokines and chemokines would not induce myocardial fibrosis, preventing the development of heart failure (Kai et al., 2005; Zozina et al., 2018).

3. OBJECTIVES

In the present study, my main goals were to investigate the role of coenzyme Q_{10} in Ca^{2+} signaling and redox homeostasis, and to test a possible therapeutic use of CoQs and OH-CoQs.

In order to understand the role of CoQ_{10}, I addressed the following objectives:

1. To determine whether depletion or increase in CoQ_{10} affects the mitochondrial Ca^{2+} and redox signaling in human skin fibroblasts (HSF).
2. To test whether addition of mitochondrial targeted CoQ and OH-CoQ alters the mitochondrial Ca^{2+} and redox signalling in HSF genetically deficient in CoQ_{10}, and to identify the parameters involved.
3. To investigate the role of CoQ_{10} in the regulation of ferroptosis in HSF and the function of CoQs and OH-CoQs as inhibitors of ferroptosis.
4. To unravel a connection between CoQ_{10}, Ca^{2+} signaling and ferroptosis in HSF.

Since patients with CoQ_{10} deficiency often display heart-related pathologies, I focused my efforts on the role of CoQ_{10} in these diseases. For this purpose, I addressed the following objectives:

1. To investigate whether CoQ_{10} affects the Ca^{2+} signaling in cardiomyocytes.
2. To determine the function of CoQ_{10} in the regulation of ferroptosis in cardiomyocytes and to identify a possible therapeutic use of CoQs and OH-CoQs.

4. MATERIALS AND METHODS

4.1. CONSUMABLES

Laboratory consumables (pipettes, tips, centrifuge tubes, cell culture flasks, dishes and microplates) are purchased from Sarstedt, Eppendorf, and Corning/Falcon.

4.2. CELL LINES

Table 1. Cell lines used in the study.

Cell	Description
HSF	Primary human skin fibroblasts (Cells provided by the Department of Dermatology, Venereology and Allergology, UMG)
P104	Fibroblasts from a 15-year-old woman with cerebellar ataxia caused by a mutation in the ADCK3 gene, which generates a CoQ_{10} deficiency.*
P106	Fibroblasts from a child with multiple disorders caused by a mutation in the COQ2 gene that leads to a CoQ_{10} deficiency.*
COQ4mut iPSC-CM **(COQ4 mutated iPSC-Cardiomyocytes)**	iPSC were generated using the CytoTune-iPS Sendai Reprogram-ming Kit (Life Technologies, Carlsbad, California, www.thermofisher.com), from primary dermal fibroblasts. Those fibroblasts were from a 4-year-old girl diagnosed with minor mental retardation and lethal rhabdomyolysis caused by a mutation in the COQ4 gene (c.483 G>C), leading to a CoQ_{10} deficiency.#

	CQ4mut-iPSC were differentiated *in vitro* into pure cardiomyocytes by Johanna Heine (AG Katrin Streckfuß-Bömeke, Göttingen).
COQ4corr iPSC-CM **(COQ4 corrected iPSC-Cardiomyocytes)**	CRISPR-Cas9 gene editing was used to get COQ4-corrected iPSC from COQ4-mutated iPSC.# CQ4corr-iPSC were differentiated *in vitro* into pure cardiomyocytes by Johanna Heine (AG Katrin Streckfuß-Bömeke, Göttingen).

***** Cells provided by Prof. Placido Navas from Pablo de Olavide-CSIC University, Seville, Spain.

iPSCs with mutation in COQ4 and the corrected ones were provided by Banco Nacional de Lineas Celulares (BNLC), Instituto de Salud Carlos III, Madrid, with the authorization of Pablo Menéndez, Josep Carreras Leukaemia Research Institute, School of Medicine, University of Barcelona, Spain. Primary dermal fibroblasts with mutation in COQ4 gene (from which the iPSCs were generated) were obtained from the patient in accordance with procedures approved by the Clinic Hospital of Barcelona and informed consent was obtained in accordance with the Declaration of Helsinki. iPSCs were generated in the lab of Pablo Menéndez (Romero-Moya et al., 2017).

4.3. CELL CULTURE

Human Skin Fibroblasts (HSF) were maintained in Dulbecco's modified Eagle's medium (DMEM; Gibco Cat. No. 41966-029) and 10 % fetal bovine serum (FBS; Sigma-Aldrich, Cat. No. F7524). The fibroblasts from patients with the genetic deficiency in CoQ_{10}, P104 and P106, were also cultured in DMEM and 10 % FBS plus 1 % Penicillin-Streptomycin (10,000 units penicillin and 10 mg streptomycin/mL; Sigma-Aldrich, Cat. No. P4333). During experiments cells were cultured without antibiotics, and P104 and P106 were maintained with DMEM + 10 % FBS as HSF. Cells were grown on untreated T75 flask at 37 °C in a humidified 5 % CO_2 atmosphere, and the medium was changed every third - fourth day. For passaging cells, confluent flask were washed once with phosphate buffered saline (PBS; Applichem, Cat. No.

A-0964), followed by a short trypsinization with 0.05 % trypsin-EDTA (Thermo Fisher Scientific, Cat. No. 25300-062). The trypsin was neutralized with culture medium (1:5) and after a centrifugation step (1,000 rpm, 5 min) and removing the supernatant; the cells were re-suspended in their culture medium and seeded at the necessary confluence. For counting cells, The Countess™ II FL Automated Cell Counter was used. The sample was prepared by adding 10 µL of cell suspension to 10 µL of 0.4 % trypan blue stain (Thermo Fisher Scientific, Cat No. 15250061), and loaded into the counting chamber (Countess™ Cell Counting Chamber Slide).

The iPSC-CM were maintained in medium RPMI 1640 Medium, GlutaMAX™ Supplement Reagent (Thermo Fisher Scientific, Cat. No. 61870-010) with the addition of B-27™ Supplement (50X), serum free (Thermo Fisher Scientific, Cat. No. 17504-044). iPSC-CM were kept in 6-well plate and medium was changed every two days. To digest iPSC-CM, 0.05 % trypsin-EDTA was used for 5 min, whose reaction was neutralized with FBS (1: 1) and followed with a centrifugation step (1,000 rpm, 5 min). The supernatant was discarded and the pellet with the cells was resuspended in Cardio digest medium containing their culture medium plus 25 mM Hepes (Thermo Fisher Scientific, Cat. No. 15630106), 20 % FBS and 2 µM Thiazovivin (Sigma-Aldrich, Cat. No. SML1045). Cells were counted in a Neubauer counting chamber and seeded at desire cell amount in a Geltrex (Thermo Fisher Scientific, Cat. No. A1413302) pre-coated (overnight at 4 °C) plates.

4.4. CELL TREATMENTS

4.4.1. Inhibition of CoQ_{10} synthesis by 4-Nitrobenzoate in HSF

HSF cultured in DMEM + 10 % FBS were treated with 4 mM 4-nitrobenzoate (4-NB; Sigma-Aldrich, Cat. No. 72910), an analogue of 4-hydroxybenzoate (4-HB), precursor of the benzoquinone ring, which inhibits 4-hydroxybenzoate:polyprenyl transferase (COQ2) leading to a decrease in the biosynthesis of CoQ_{10}. To demonstrate that the effects of 4 mM 4-NB were caused by CoQ_{10} deficiency rather than side effects of the compound, fibroblasts were supplemented also with 4 mM 4-NB + 2 mM 4-HB (Sigma-Aldrich, Cat. No. 240141). Medium was changed at day 1, 3 and 5, and cells were collected at day 7 for further experiments. 4-NB and 4-HB were dissolved in Dimethylsulfoxid (DMSO; Sigma-Aldrich, Cat. No. D2650) in a

concentration of 0.1 M and stored at -20 °C. This treatment protocol was based on the publication of Quinzii *et al.* (Quinzii et al., 2012).

4.4.2. Addition of Quinones to HSF, P104 and P106

Cells cultured in DMEM + 10 % FBS were treated with mitoquinone mesylate (mitoQ; Hycultec, Cat. No. HY-100116A), hydroxyl-mitoquinone trifluoroacetate (OH-mitoQ)*, decylubiquinone (DecylQ; Sigma-Aldrich, Cat. No. D7911), hydroxyl-decylubiquinone (OH-decylQ)*, coenzyme Q_1 (Q_1; Sigma-Aldrich, Cat. No. C7956) or hydroxy-coenzyme Q_1 (OH-Q_1)* in concentrations and for the duration as indicated in each experiment.

* Hydroxylated quinones were provided by Dr. Reinhard Kappl, Medical Faculty of Saarland University, Homburg, Germany.

Quinones were dissolved in DMSO in a concentration of 10 mM, they were further dissolved in ddH_2O to obtain a stock solution of 1 mM. The compounds were stored at -20 °C.

4.4.3. Addition of ferroptosis inducers to HSF

In order to induce ferroptosis cultured cells were treated with BSO (Sigma-Aldrich, Cat. No. B2515), erastin (Sigma-Aldrich, Cat. No. E7781) or RSL3 (Selleckchem, Cat. No. S8155) in concentrations and for the duration as indicated in each experiment.

FINs were dissolved in DMSO in a stock solution of 225 mM for BSO and 10 mM for erastin and RSL3. The compounds were stored at -20 °C.

4.5. PROLIFERATION AND VIABILITY ASSAY USING CELL TITER-BLUE

Proliferation was measured by using the CellTiter-Blue® Cell Viability Assay (CTB; Promega, Cat. No. G8081). It is a fluorometric method for estimating the number of viable proliferating cells. The assay is based on the ability of living cells to convert a redox dye (resazurin) into a

fluorescent end product (resorufin). Nonviable cells, however, rapidly lose this metabolic capacity and thus, do not generate a fluorescent signal (Promega Corporation, Technical Bulletin, 2016).

In order to characterize the fibroblasts of this study in respect to metabolic capacity and proliferation, to compare the toxicity of the used quinones, or their effect in the regulation of the ferroptosis, 1 x 10^4 fibroblasts were seeded per well into a transparent 96-well plate. Each condition was seeded minimum in triplicate and was left to settle in an incubator for 4 hours before any treatment or drug addiction. For the different experiments see below:

- To check if 4-NB and 4-HB cause any effect on the proliferation and viability of the cells, treated cells were seeded in a total volume of 100 µL DMEM + 10 % FBS per well.
- To check and compare de toxicity of the different quinones, cells were seeded and medium was changed 4 hours later and DMSO (as control), mitoQ, OH-mitoQ, decylQ, OH-decylQ, Q_1 and OH-Q_1 were added at 0.1 µM, 0.5 µM, 1 µM, 2.5 µM or 5 µM, in a total volume of 100 µL DMEM + 10 % FBS per well.
- In order to induce ferroptosis and see the effect of the quinones in the regulation of this cell death; medium was changed 4 hours after cell seeding and ferroptosis was induced by adding 100 µM BSO, 1 µM erastin or 0.5 µM RSL3 in a volume of 100 µL DMEM + 10 % FBS per well. After 1 hour, the quinones (mitoQ, OH-mitoQ, DecylQ, OH-DecylQ, Q_1 and OH-Q_1) and DMSO (as control) were added on top to a final concentration of 0.5 µM and in a total volume of 200 µL per well.
- To reduce the content of CoQ_{10} in fibroblast and induce ferroptosis, 1.25 µM Simvastatin (Sigma-Aldrich, Cat. No. 79902-63-9) were added for 72 hours (Marcheggiani et al., 2019). Simvastatin was dissolved in DMSO in a stock solution of 10 mM and stored at -20 °C. Afterwards, the medium was changed with a fresh addition of Simvastatin and ferroptosis was induced by adding a final concentration of 1 µM erastin or 0.5 µM RSL3. Quinones (or DMSO as control) were also added in a final concentration of 0.5 µM. The total volume was 200 µL of DMEM + 10 % FBS per well.

After the indicated growth time (12, 24, 48 or 72 hours), in each well with 100 µL or 200 µL growth medium, 10 µL or 20 µL of CellTiter-Blue® Reagent were added, respectively, and the assay was incubated at standard culture conditions (37 °C, 5 % CO_2) for 4 hours. Then,

fluorescence was recorded by using a Mithras LB 940 Multimode Microplate Reader (Berthold Technologies GmbH & Co. KG). The settings used for the experiments are shown in **Table 2.**

Table 2. Measurement settings for proliferation assay.

Excitation Filter	550 nm
Emission Filter	600 nm
Counter position	Top
Shake	100 rpm before plate reading

Fluorescence data were analysed and plotted by using Microsoft Excel 2016. The obtained values, were background subtracted (medium only) and were normalized with untreated cells.

4.6. VIABILITY ASSAY USING PFA FIXATION AND CRYSTAL VIOLET STAINING

Cell viability upon FIN treatment was assessed by cell fixation with 4 % PFA (Paraformaldehyd; stock solution of 16 % dissolved in PBS and calibrated with NaOH (Applichem, Cat. No. A.1432) for a pH = 7.2; Sigma-Aldrich, Cat. No. P6148) dissolved in PBS, followed by staining with a 0.05 % crystal violet solution (**Table 3**).

For this purpose, 300,000 cardiomyocytes/well were seeded in 6-well plates. After their attachment, cells were treated with different concentrations of FINs and quinones (RSL3 10 µM 216 hours / Erastin 10 µM 72 hours and 0.5 µM of mitoQ, OH-mitoQ, decylQ or OH-decylQ 216 hours). Afterwards, FIN-resistant cells were fixed with 4 % PFA for 5 minutes. Cells were subsequently washed thrice with 1 x PBS and stained with 0.05 % crystal violet for 30 minutes at room temperature. Following staining, cells were washed twice with ddH_2O and allowed to dry before imaging. Images were acquired using a Carl Zeiss Axiovert S100TV inverted microscope featuring a sCMOS pco.edge camera, 5× objective and VisiView® Software (Visitron Systems GmbH, Puchheim, Germany) and quantification was performed using ImageJ.

Table 3. Crystal Violet solution recipe.

Chemical	Concentration	Company	Product number
Crystal violet	0.05 %	Sigma-Aldrich	P6148
Formaldehyde	1 %	Carl Roth	4980.1
PBS	1 X	Gibco	14190-094
Methanol	1 %	Carl Roth	4627.5
ddH_2O	-	-	-

4.7. DETERMINATION OF MRNA EXPRESSION LEVELS

To check expression levels of genes related to cytosolic and mitochondrial calcium mobilization in fibroblasts, real-time quantitative polymerase chain reaction (RT-qPCR) was performed. Initially, RNA was isolated from the different fibroblasts. Then, complementary DNA (cDNA) was synthesized and, finally, RT-qPCR was performed.

4.7.1. RNA isolation

The total RNA was isolated using the RNeasy Plus Mini Kit (Qiagen, Cat. No. 74134) according to the manufacturer's protocol. First, all fibroblasts (with each study treatment) were grown in T75 flask to 85 - 95 % confluence and trypsinized to collected as a pellet. The pellet was re-suspended and lysed in 700 µL RLT Plus buffer + β-Mercaptoethanol (Applichem, Cat. No. A-1108). Each cell-homogenized lysate was then transfer to a gDNA Eliminator spin column placed in a 2 mL collection tube. After a short spin down, the column was discarded and the flow-through was saved. Next, 700 µL of 70 % ethanol (EtOH; Carl Roth, Cat. No. 5054.1) was added and mixed well by pipetting. The mix was then transferred to an RNeasy spin column placed in a 2 mL collection tube and spun down. The flow-through was discarded and the column was washed once with 700 µL Buffer RW1 and twice with 500 µL Buffer RPE working solution. After centrifugation to dry the membrane of the RNeasy spin column, the column was transferred to a new collection tube. Lastly, the RNA was eluted by the addition of 50 µL

RNase-free H_2O (DEPC-treated water) followed by a centrifugation step and the flow-through containing the total RNA was collected. The RNA concentration was measured with the NanoDrop 2000c (Thermo Scientific).

4.7.2. cDNA synthesis

The cDNA was synthesized by reverse transcription from the isolated RNA using the SuperscriptTM IV Reverse Transcriptase Kit (Invitrogen, Cat. No. 18091050, 18091150). First, 800 ng of template RNA were mixed with 50 µM Oligo-d(T)20 primers (Invitrogen, Cat. No 18418-020) and 10 mM dNTP mix (Invitrogen, Cat. No. 18427-013) to a final volume of 13 µL (addition of DEPC-treated water if necessary). This RNA-primer mix was heated at 65 °C for 5 minutes in a thermo cycler (C1000TM Thermal Cycler, Bio-Rad), which allow the primer annealing. Then, the annealed RNA was incubated on ice for at least 1 minute.

In the next step, RT reaction mix was prepared mixing 4 µL of 5× SuperScriptTM IV buffer (Invitrogen, Cat. No. 18090200), 1 µL of 100 mM DTT (Dithiothreitol (DL-); Sigma-Aldrich, Cat. No. D 0632), 1 µL of Ribonuclease Inhibitor (Invitrogen, Cat. No. 10777-019) and 1 µL of SuperScript™ IV Reverse Transcriptase (200 U/µL) (Invitrogen, Cat. No. 18090200) for each annealed RNA sample. To each annealed RNA, 7 µL of RT reaction mix were added, the combined reaction mixture was incubated at 55 °C for 10 minutes and lastly the reaction was inactivated by incubating at 80 °C for 10 minutes (both steps in the thermos cycler). The synthesized cDNA could then be used immediately for PCR amplification or stored it at -20 °C.

4.7.3. Quantitative real-time polymerase chain reaction (RT-qPCR)

The DNA amplification of a target gene was monitored by RT-qPCR using QuantiTect SYBR Green PCR Kit (Quiagen, Cat. No. 204141). This kit contains the 2× QuantiTect SYBR Green PCR Master Mix, which in turn contains: HotStarTaq®DNA Polymerase, QuantiTect SYBR Green PCR Buffer, dNTP mix (including dUTP), SYBR Green I, ROX™ passive reference dye and 5 mM $MgCl_2$ (see **Table 4** for more details). The SYBR Green I dye is a fluorescent dye

(494 nm Excitation) that binds with all double-stranded DNA molecules, emitting a fluorescent signal (521 nm Emission) on binding which can be monitored following each PCR cycle.

To proceed with the RT-qPCR, the 2× QuantiTect SYBR Green PCR Master Mix was mixed together with the primers of interest and DEPC-treated water, getting the so called reaction mix. (All primers were purchased from Qiagen and are listed in **Table 5**). Then, the RT-qPCR reaction mix and the cDNA (49 µL + 1 µL respectively) were pipetted into a 96-well PCR plate (**Table 6**). The plate was closed with a 4titude® adhesive qPCR seal (4titude®, Cat. No. 0560) in order to avoid the evaporation of the content due to high temperature cycles. The RT-qPCR was performed with the Stratagene Mx3000P qPCR System (Agilent Technologies), using the cycling program described in **Table 7**.

The results were analysed with the MxPro qPCR software. TBP (TATA box binding protein) was used in all RT-qPCRs as a housekeeping gene. The CT (number of cycles required for the fluorescent signal to exceed the fluorescent threshold) values of the target mRNAs were normalized to the CT values of TBP. Data were quantitated using the 2-ΔCT method.

Table 4. Components and their description included in 2× QuantiTect SYBR Green PCR Master Mix.

Component	Description
HotStarTaq DNA Polymerase	HotStarTaq DNA Polymerase is a modified form of a recombinant 94 kDa DNA polymerase, originally isolated from *Thermus aquaticus*, cloned into *E. coli*. (Deoxynucleoside-triphosphate: DNA deoxynucloetidyltransferase, EC 2.7.7.7).
QuantiTect SYBR Green PCR Buffer	Contains Tris-Cl, KCl, $(NH_4)_2SO_4$, 5 mM $MgCl_2$, pH 8.7 (20 °C)
dNTP mix	Contains dATP, dCTP, dGTP, and dTTP/dUTP of ultrapure quality
Fluorescent dyes	SYBR Green I and ROX
RNase-free water	Ultrapure quality, PCR grade

Table 5. RT-qPCR oligonucleotides (sequences 5' – 3').

Name	Forward primer sequence	Reverse primer sequence
HK TBP	CGGAGAGTTCTGGGATTGT	GGTTCGTGGCTCTCTTATC
ORAI1	ATGAGCCTCAACGAGCACT	GTGGGTAGTCGTGGTCAG
ORAI2	TGGAACTGGTCACCTCTAAC	GGGTACTGGTACTGCGTCT
ORAI3	GTACCGGGAGTTCGTGCA	GGTACTCGTGGTCACTCT
STIM1	CAGAGTCTGCATGACCTTCA	GCTTCCTGCTTAGCAAGGTT
STIM2	GTCTCCATTCCACCCTATCC	GGCTAATGATCCAGGAGGTT
MCU a	CACACAGTTTGGCATTTTGG	TGTCTGTCTCTGGCTTCTGG
MCU b	TTTTGCGTGTGAAGCTGTGT	TACCAAGGGAAGGCCATGT
Micu1	GTGTTCAGCCCTCACAACCT	CCACCAAACTGCCTCTCAGT
Micu2	AGCGCTTCATGCAGTTTTCT	CAGCTGTTTGGATCCCTGAC
Micu3	CCAGTTTGGAAAGGCTCATC	ATTCTGAACCCTGCATGTGG
MCUR1	GCCCTTCCCCAGTACCAC	AGAGTTTCCTGCTCCCAGAA
EMRE	CTTGAGGAAAGATGGCGATG	CGACATAGAGAAAGGGGATCA

The annealing temperature for all used primers was 58 °C.

Table 6. Components of the reaction mix used for RT-qPCR.

Reagent	Volume used per reaction (µL)
2× QuantiTect SYBR Green PCR	25
10 µM forward primer	1.5
10 µM reverse primer	1.5
ddH_2O	21
cDNA (< 500 ng)	1

Table 7. RT-qPCR cycling program.

Number of cycles	Temperature (°C)	Time (min:sec)	Step
1	95	15:00	polymerase activation
35	95	00:15	denaturation
	58	00:30	annealing
	72	00:30	elongation
1	95	1:00	dissociation
	58	00:30	
	95	00:30	

4.8. WESTERN BLOT

Western blot (WB) is a molecular biology method used to detect specific proteins among a mixture of proteins extracted from cells. This method consists of four main steps: sample preparation (section **4.8.1.**), protein separation by size (section **4.8.2.**), transfer to a nitrocellulose membrane (section **4.8.3.**) and labelling of the desired proteins with the use of corresponding primary and secondary antibodies (section **4.8.4.**). WB were done with the help of Ioana Todoran.

4.8.1. Sample preparation

First, fibroblasts were grown in T75 flask to 85 - 95 % confluence and treated with 0.5 µM mitoQ or OHmitoQ, and same amount of vehicle (DMSO) for 24 hours. Next, cells were washed twice with ice-cold 1× DPBS to remove the medium and any debris and they were lysed directly on the plate with the appropriate volume of lysis buffer (TGH lysis buffer), which was dependent on cell confluence. The TGH lysis buffer was prepared freshly (always keeping it on ice. See recipe **Table 8**). Immediately with a rubber scraper, the cells were scraped and the lysates were collected and transferred to 1.5 mL tubes. The tubes were incubated on ice for 20 minutes, during that time cells were often resuspended and subsequently centrifuged at 13,000

rpm for 10 minutes at 4 °C. The supernatants were collected and transferred to new tubes and they could be used directly or kept at -80 °C until further use.

The protein concentration of the cell lysates was quantified using the Bradford reagent (see recipe **Table 9**). This method is a protein colorimetric assay based on COOMASSIE® Brilliant Blue G 250, a dye that shows a change in absorbance from 470 nm to 595 nm upon binding to proteins. Therefore, it shows a differential colour change in response to different protein concentrations. For each sample, 1 µL of protein lysate was mixed with 799 µL ddH_20 and 200 µL Bradford's reagent. 200 µl of each sample was poured in triplicate into 96-well plates. In addition, to estimate the amount of proteins in the solution, a calibration curve for bovine serum albumin protein (BSA) was performed, ranging from 0.5 to 20 µg / mL. Quickly, the absorbance at 595 nm was read using the Berthold Mithras LB 940 device. The amount of absorption was directly proportional to the protein present in the sample.

Table 8. TGH lysis buffer recipe

Chemical	Concentration	Company	Product number
Na_3VO_4	1 mM	Sigma-Aldrich	S6508-50G
PMSF	1 mM	Sigma-Aldrich	P7626
NaF	1 mM	Sigma-Aldrich	S7920-100G
Protease Inhibitor (PI)	1 X	Roche	1183617001

Table 9. Bradford reagent recipe

Chemical	Concentration	Company	Product number
COOMASSIE® Brilliant Blue G 250	339 µM	Serva	35050
Ethanol	19.2 %	Carl Roth	P075.4
H_3PO_4	34 %	Carl Roth	9079.1
ddH_2O	-	-	-

4.8.2. Protein separation by size

Protein separation was performed by sodium dodecyl sulfate polyacrylamide gel electrophoresis (SDS-PAGE). First, all samples were adjusted to reach the same concentration (50 µg), mixed with 4× Lämmli buffer (Bio-Rad, Cat. No 1610747) (containing 1:10 β-mercaptoethanol (Gibco, Cat. No. 1985-023)) and denatured at 95 ° C. Next, the proteins were loaded into the formed wells in the polyacrylamide gel, which was totally buffered (Running Buffer, see recipe in **Table 10**). The polyacrylamide gel consisted in two parts, the stacking gel and the separating gel (**Tables 11-14** to see the recipe). Next, an electric current was applied that ran through the gel, causing proteins that are negatively charged to migrate through towards the anode (positively charged). Smaller proteins pass more easily through the pores of the gel migrating faster, while larger proteins encounter more resistance and migrate more slowly, thus separating the proteins by their molecular weight. The applied voltage at the beginning of the electrophoresis was 60 V, once the samples reached the separating gel, it was increased to 110 V. A protein ladder (Precision Plus Protein ™ Dual Color Standard; Bio-Rad, Cat. No. 161-0374) was used to determine the size of the protein.

Table 10. Running buffer recipe

Chemical	Concentration	Company	Product number
Tris	25 mM	Carl Roth	5429.3
Glycine	192 mM	AppliChem	A1067
SDS	0.1 %	Sigma-Aldrich	L-4509
ddH_2O	-	-	-

pH = 8.3

Table 11. Stacking gel buffer recipe

Chemical	Concentration	Company	Product number
Tris	0.5 M	Carl Roth	5429.3
SDS	0.4 %	Sigma-Aldrich	L-4509
ddH_2O	-	-	-

pH = 6.8. It was adjusted with NaOH 2 M (Merck, Cat. No, 109136) or HCl 1 M (Carl Roth, Cat. No. K025.1).

Table 12. Stacking gel recipe

Chemical	Concentration	Company	Product number
Stacking gel buffer	3 X	-	-
Acrylamide	5 %	Carl Roth	248272357
APS	0.075 %	Sigma-Aldrich	A3678
TEMED	6.67 M	Sigma-Aldrich	T7024
ddH_2O	-	-	-

Table 13. Separation gel buffer recipe

Chemical	Concentration	Company	Product number
Tris	1.5 M	Carl Roth	5429.3
SDS	0.4 %	Sigma-Aldrich	L-4509
ddH_2O	-	-	-

pH = 8.8. It was adjusted with NaOH 2 M (Merck, Cat. No, 109136) or HCl 1 M (Carl Roth, Cat. No. K025.1).

Table 14. Separation gel recipe

Chemical	Concentration	Company	Product number
Separation gel buffer	3 X	-	-
Acrylamide	10 %	Carl Roth	248272357
APS	0.075 %	Sigma-Aldrich	A3678
TEMED	6.67 M	Sigma-Aldrich	T7024
ddH_2O	-	-	-

4.8.3. Protein transfer to a nitrocellulose membrane

The proteins were transferred from the polyacrylamide gel to a 0.2 µm nitrocellulose membrane (Bio-Rad, Cat. No. 1704270) with the Trans-Blot® TurboTM Transfer System following the manufacturer's recommendations. The membranes and transfer stacks were equilibrated in transfer buffer (the recipe is shown in **Table 15**) for 3 minutes. The "transfer sandwich" was then assembled in the following order: botton (+) cassette (anode), bottom transfer stack, nitrocellulose membrane, gel top transfer stack, top (-) cassete (cathode), and it was placed in the device. The transfer was performed at 1.3 A, 25 V, for 7 minutes.

Table 15. Transfer buffer recipe

Chemical	Concentration	Company	Product number
5 X transfer buffer*	1 X	Bio-Rad	1704270
Ethanol	20 %	Carl Roth	9065.2
ddH_2O	-	-	-

* Part of the Trans-Blot® Turbo™ RTA mini 0.2 µm nitrocellulose transfer kit, Bio-Rad, # 1704270.

4.8.4. Membrane blocking and antibody incubation

Once the transfer was finished, the nitrocellulose membranes were blocked for 1 hour with a 5 % BSA (Sigma-Aldrich, Cat. No. SLBV4989) TBS solution (**Table 16**), then the primary antibodies were added and incubated overnight at 4 ° C. The primary antibodies used were Anti-MCU (D2Z3B) Rabbit mAb (Cell Signal. Tech., Cat. No.14997S), Anti-MCUb (C109B Antibody (C-term) (Abgent Cat. No. AP12355b)), Anti-MICU2 (Sigma-Aldrich, Cat. No. HPA045511) and Anti-MICU3 (Sigma-Aldrich, Cat. No. HPA024779) 1:500. And as a loading control it was used Calnexin (ENZO, Cat. No. ADI-SPA-860-F) 1:1000.

The membranes were then washed three times with 1× TBS-T (**Table 17**) for 5 minutes each time (on a rocker platform) and incubated with the secondary antibody IRDye 800CW Donkey anti-Rabbit (Li-Cor, Cat. No. 926-32213) 1:10,000, for 1 hour at room temperature and in the dark. Finally, the membranes were washed three times with 1× TBS-T for 10 minutes each time and imaged using the Odyssey® CLx system. Bands were quantified with Image Studio ™ Lite program.

Table 16. TBS recipe

Chemical	**Concentration**	**Company**	**Product number**
Tris	50 mM	Carl Roth	5429.3
NaCl	150 mM	AppliChem	A2942
ddH_2O	-	-	-

pH = 7.6. It was adjusted with NaOH 2 M (Merck, Cat.No. 109136) and HCl 1 M (Carl Roth, Cat. No. K025.1).

Table 17. TBS-T recipe

Chemical	**Concentration**	**Company**	**Product number**
Tris	50 mM	Carl Roth	5429.3
NaCl	150 mM	AppliChem	A2942
Tween® 20	0.1 %	Carl Roth	9127.1
ddH_2O	-	-	-

4.9. CYTOSOLIC PARAMETER MEASUREMENTS

4.9.1. Cytosolic Ca^{2+} measurements in HSF

Cytosolic Ca^{2+} measurements in fibroblasts were performed by using a calcium-imaging system on a fluorescence microscope equipped with an Axiovert S100TV (Carl Zeiss), pE-340fura (CoolLED, Andover, United Kingdom) LED light source with LED 340 nm (excitation filter: 340/20) and 380 nm (excitation filter: 380/20) together with a T400 LP dichroic mirror and 515/80 emission filter, 20× Fluar (N.A. 0.75) objective and a sCMOS pco.edge camera. Data acquisition was performed with VisiView 2.1.2 (Visitron Systems GmbH).

Cytosolic Ca^{2+} was measured with the ratiometric acetoxy-methyl-ester Fura-2 (Fura-2 AM; ThermoFisher, Cat. No. F1221), which diffuses across the cell membrane and is de-esterified by cellular esterases generating Fura-2 free acid. When free cytCa^{2+} binds to Fura-2, the peak excitation wavelength changes from 380 nm to 340 nm, while the peak emission around 510 nm remains unchanged. The values obtained by measuring the ratio of the fluorescence emission signal (340 nm / 380 nm) in the presence of known free Ca^{2+} concentrations, correlate with the concentration of cytCa^{2+} (Tinning et al., 2018).

For the cell preparation process, fibroblasts (100,000) were seeded on 25 mm round glass coverslips with a thickness No. 1.5 (VWR, Radnor, ISA, Cat. No. 6310172) 24 hours before measuring and in a confluence of 75 – 85 %. Cells were seeded in 2 mL DMEM medium supplemented with 10 % FBS. If necessary the cells were treated. In the case of CoQ_{10} inhibition, they were treated for 7 days prior to this experiment as indicated in chapter **4.4.1.**. In the case of addition of quinones or FINs to cell culture, this was done once they had been seeded on the coverslips. It was waited for the cells to attach to the bottom (minimum 4 hours) and the quinones were added at a concentration of 0.5 µM and erastin at 1 µM, for 24 hours prior imaging.

Before measuring, cells were stained with 1 µM Fura-2 AM solution (1 mM stock solution dissolved in DMSO) in growth medium for 30 minutes at room temperature on a platform shaker (Grant-Bio PMR-30 mini rocker-shaker).

For the measurements, a perfusion system was used, consisting of two tubes: an input tube connected to 1 mL syringe through which the working solution is added and the output tube that discharges the previous solution into a liquid-waste bottle by a suction line connected to a

vacuum pump; and an imaging chamber to which both tubes are connected, creating a small perfusion channel that enables a rapid solution exchange with minimal disturbance of the cells. Before each measurement, the perfusion system and the imaging chamber were properly cleaned with 70 % EtOH and ddH_2O, the input tube was carefully loaded with the first measuring solution (**Table 19**).

After incubation of FURA-2 AM and after removal of excess medium, the coverslip with the attached cells was assembled in the imaging chamber. First, the coverslip was mount onto the chamber ring. The perfusion chamber was then fixed with silicone paste, on top. A 12 mm round glass coverslip with a thickness No. 1.5 (VWR, Radnor, ISA, Cat. No. 630-2190) was inserted on the perfusion chamber fixed as well with silicone (**figure 16**). Lastly, the imaging chamber was placed into the microscope and connected to the perfusion tubes from both sides allowing the perfusion of solutions through the chamber.

The cells were perfused carefully with the first measuring solution to wash away remaining medium and poorly attached cells, and were left to equilibrate for a few minutes before starting the measurement. The measurements were performed in Ringer's buffer (pH 7.4; 310 mosmol/L) containing 145 mM NaCl, 4 mM KCI, 10 mM Glucose, 10 mM HEPES (4-(2-hydroxyethyl)-1-piperazineethanesulfonic acid), 2 mM $MgCl_2$, and concentrations of $CaCl_2$ as indicated, or in 0 mM $CaCl_2$ with 1 mM EGTA at room temperature. The settings used in the experiments are described in **Table 18**.

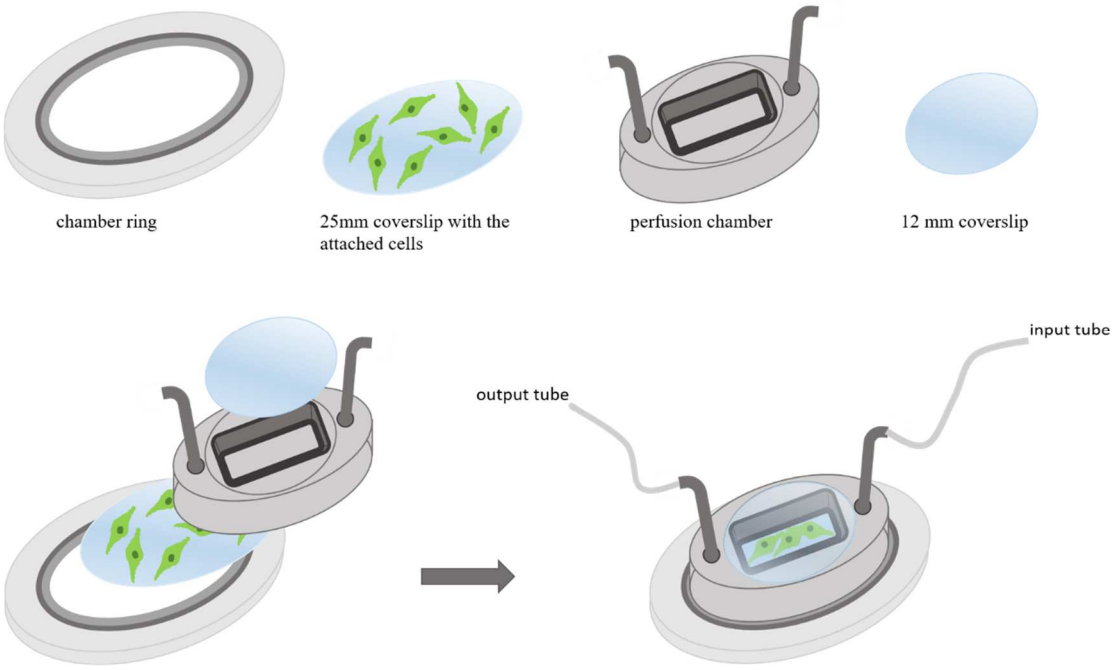

***Figure 16**. Image chamber and perfusion system for cytosolic Ca^{2+} measurements. The individual parts that make up the image camera are shown at the top of the figure. In the lower left corner, the assembly is shown, and in the right the final result ready to be placed in the microscope with the connected tubes that create the perfusion system.*

Before starting the measurement, the cells that were successfully loaded with the dye were identified and individually selected with the imaging software, thus defining the regions of interest (ROI) to monitor the change of cytCa^{2+} in each cell. By using a specific measurement protocol (see **Table 19** for detailed protocol) several parameters were obtained: first, with 0.5 mM Ca^{2+} Ringer solution a baseline. Then, Ca^{2+}-free Ringer's solution was perfused to get the minimum levels of cytCa^{2+}. For ER Ca^{2+} store depletion, the chamber was perfused with Ca^{2+}-free Ringer's solution containing 1 µM thapsigargin (Tg; Sigma-Aldrich, Cat. No. T9033; dissolved as 1 mM stock solution in DMSO) or 100 µM histamine (His; Sigma-Aldrich, Cat. No. H7125-1G; dissolved as 10 mM stock solution in DMSO) observing the increase in cytCa^{2+} resulting from ER Ca^{2+}. Once the Ca^{2+} levels returned to minimum (minimum fluorescence levels), 0.5 mM Ca^{2+} Ringer solution with Tg or His was perfused to measure SOCE. Last, Ca^{2+}-free Ringer's solution with Tg or His was perfused to return to minimum values and ensure that the cells are in good condition.

Table 18. Measurement settings for Fura-2 imaging of cytosolic Ca^{2+} in HSF.

Excitation 1	340 nm (filter: 340/20; 25% intensity, 30 ms exposure time)
Excitation 2	380 nm (filter: 380/20; 5% intensity, 30 ms exposure time)
Dichroic mirror	T400 LP
Emission	510 nm (515/80 emission filter)
Objective	Fluar 20×/0.75
Cycle time	5 sec
Number of cycles	260

Table 19. Protocol for cytosolic Ca^{2+} measurements of fibroblast.

Number of cycle	Solution used
0-Start	0.5 mM Ca^{2+} Ringer's solution
30	0 mM Ca^{2+} Ringer's solution
60	0 mM Ca^{2+} Ringer's solution with 1 µM Tg / 100 µM His
160	0.5 mM Ca^{2+} Ringer's solution with 1 µM Tg / 100 µM His
220	0 mM Ca^{2+} Ringer's solution with 1 µM Tg / 100 µM His
260-Stop	-

The obtained 340 nm / 380 nm background corrected fluorescence ratios were analyzed and plotted by using Microsoft Excel 2016. Data are presented as average ratio of 340 nm / 380 nm values for Fura-2 AM over time (minutes).

4.9.2. Cytosolic Ca^{2+} measurements in Cardiomyocytes

Cytosolic Ca^{2+} measurements in cardiomyocytes were performed on a Zeiss Axio Observer 7 setup, equipped with a Plan-Apochromat 20× (N.A. 0.8) objective and pE-340fura (CoolLED, Andover, United Kingdom) LED light source with excitation LEDs at 340 nm (excitation filter: 340/20) and 380 nm (excitation filter: 380/20) together with a 409 nm dichroic mirror and 510/84 nm emission filter, keeping a humidified atmosphere of 37 °C during the measuring. Cardiomyocytes were field-stimulated at 0.5 Hz, 18.0 V and 3 ms using a MyoPacer EP Field Stimulator model MEP100 (IonOptix Corporation, Milton, MA.) in order to synchronize the contraction and images were acquired with Zen 3.2 software (Zeiss, Oberkochen, Germany).

For cell preparation process, 7 - 8 weeks after cardiac differentiation initiation, 300.000 iPSC-CM were seeded in a 25 mm x 25 mm squared glass coverslips with a thickness No. 1.5 (Corning, Cat. No. 2850-25) placed in 6-well plates, getting a monolayer. The coverslips were

previously coated with Geltrex overnight at 4 °C. Cells were seeded in 2 mL RPMI 1640 GlutaMAX™ medium supplemented with B-27 and kept at rest for 6 days.

Cytosolic Ca^{2+} was measured with Fura-2 AM dye and before measuring, the staining proceeded as described in section **4.9.1.** for HSF. After incubation of FURA-2 AM and after removal of excess medium, the coverslip with the attached cells was assembled in the MyoPacer imaging chamber, 500 µL of Ringer's buffer containing 2 mM Ca^{2+} were added on top and the chamber was placed into the microscope connecting to the electrodes.

Before starting the measurement, the iPSC-CM that were successfully loaded with the dye and contracting were identified and individually selected with the imaging software defining ROI to monitor the change of cytCa^{2+} in each cell.

The settings used for imaging are described in **Table 20**. No particular protocol was used since variations in cytCa^{2+} were due to contraction *per se*. Only addition of 500 µL 2 mM Ca^{2+} Ringer's solution with 30 µM digitonin (dig; Sigma-Aldrich, Cat. No. D141) was added at the end causing holes in the plasma membrane and therefore the abrupt entry of Ca^{2+} into the cytosol proving that the measurement worked.

Table 20. Measurement settings for Fura-2 imaging of cytosolic Ca^{2+} in cardiomyocytes.

Excitation 1	340 nm (filter: 340/20; 25% intensity, 20 ms exposure time)
Excitation 2	380 nm (filter: 380/20; 5% intensity, 20 ms exposure time)
Dichroic mirror	409 nm
Emission	510 nm (510/84 emission filter)
Objective	Plan-Apochromat 20×/0.8
Cycle time	0.2 sec
Number of cycles	-

The obtained 340 nm / 380 nm background corrected fluorescence ratios were analyzed and plotted by using Microsoft Excel 2016. Data are presented as average ratio of 340 nm / 380 nm

values for Fura-2 AM over time (seconds). For quantification, a minimum of 8-10 peaks were analyzed for each cell and the average of all of them was determined. Then, the average of all cells in each individual measurement was calculated, and subsequently the average of all performed measurements was quantified.

4.9.3. Cytosolic H_2O_2 measurements in HSF

The oxidative state of the cells was measured based on the production of H_2O_2. These measurements were done by using an imaging system on a Carl Zeiss Observer D1 microscope equipped with a 40× oil EC-Plan Neofluar (N.A. 1.3) objective, multi-filter system, a fluorescence camera (Axiocam 702 mono, Zeiss) and LED fluorescence system (Colibri, Zeiss) at 37 °C. Data acquisition was performed with the Zen 2.6 (Zeiss) software.

Cytosolic H_2O_2 (cytH_2O_2) production was measure by using the protein sensor cyto-HyPer (HyPer 3) (**figure 17**). This sensor is YFP-based, containing two OXYR domains which upon oxidation by H_2O_2 form a disulfide bond, leading to a shift of the two excitation maxima.

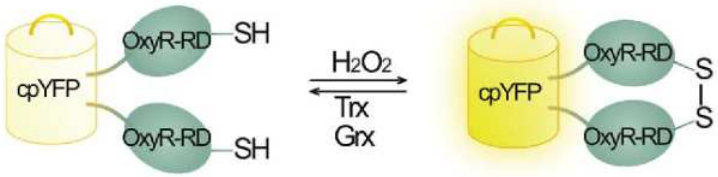

***Figure 17**. HyPer sensor illustration. HyPer has circular-permutated YFP as fluorophore and two OxyR domains which upon increase of H_2O_2 form a disulfide bond, leading to a shift and increase in excitation ratio. Image taken from (Bilan & Belousov, 2017).*

For the cell preparation process, fibroblasts were first transfected with nucleoporation using Amaxa™ 4D-Nucleofector™ System (4D-Nucleofector™ Core Unit and 4D-Nucleofector™ X Unit). Each nucleoporation proceeded by transfecting 1 x 10^6 cells with the program DT-130 and 1 µg of cyto-HyPer sensor and 100 µL P2 Primary Cell 4D-NucleofectorTM X Kit L (Lonza. Catalog #: V4XP-2024) in Nucleovette™ Vessels. After transfection, fibroblasts (100,000) were seeded in growth medium, on 25 mm round glass coverslips with a thickness of No. 1.5 (getting a confluence of 75 – 85 % of the surface) as described for cytCa^{2+}

measurements. The medium was changed 4 hours later and the cells were kept at rest between 24 and 48 hours to achieve a successful sensor expression.

If necessary the cells were treated. In the case of CoQ_{10} inhibition, they were treated for 7 days prior the transfection as indicated in section **4.4.1**. In the case of addition of quinones to cell culture, this was done once they had been seeded on the coverslips after transfection. It was waited for the cells to attach to the bottom (minimum 4 hours) and the quinones (DMSO as control) were added at a concentration of 0.5 µM for 24 hours prior imaging. Then, the coverslip with the attached cells was assembled into the image chamber and placed on the microscope to proceed with the measurement.

The imaging chamber used for these experiments was simple, consisting only in a chamber ring in which the coverslip with the attached cells is placed and fixed with silicone, and a locking ring that keeps the solution in (see **figure 18**). All the experiments also performed in Ringer's buffer containing 0.5 mM Ca^{2+}.

The settings used for the measurements are described in **Table 21.** Firstly, successfully transfected cells were located, and ROI were selected individually by using the imaging software. Secondly, the measurement protocol was performed as described below: it was started with 0.5 mM Ca^{2+} Ringer solution to obtain a baseline. Then, an equal volume of 0.5 mM Ca^{2+} Ringer solution with 200 µM H_2O_2 (Sigma-Aldrich, Cat. No. H1009), to get a final concentration of 100 µM, was added on top to measure the maximal cell oxidative capacity. Finally, to reduce the status of the cells, the same volume as initially with 30 mM DTT was added (threefold concentration than desired, 10 mM) (see **Table 22** for protocol).

As a control to access the pH sensitivity of cyto-HyPer, the pH-sensitive but H_2O_2-insensitive mutant cyto-SypHer (cyto-HyPer-C199S) was used to monitor pH changes in the cytosol, using the same experimental settings.

For analysis, all transfected cells were used and obtained data was exported and analyzed using Microsoft Excel 2016. Data are presented as average of fluorescence ratio 505 nm / 420 nm over time (minutes) normalized by the background fluorescence.

Table 21. Measurement settings for cyto-HyPer, cyto-SypHer, mito-HyPer and mito-SypHer imaging of cytosolic and mitochondrial H_2O_2 levels.

Excitation 1	420 nm (filter: 420/40; 30 % intensity, 30 ms exposure time)
Excitation 2	505 nm (filter: 500/15; 30 % intensity, 30 ms exposure time)
Dichroic mirror	515 nm
Emission	Filter: 539/25
Objective	40× oil EC-Plan Neofluar (N.A. 1.3)
Cycle time	1 sec
Number of cycles	300

Table 22. Protocol for cytosolic and mitochondrial H_2O_2 measurements of fibroblast.

Number of cycle	**Solution used**
0-Start	500 µL 0.5 mM Ca^{2+} Ringer's solution
100	Addition of 500 µL 0.5 mM Ca^{2+} Ringer's solution with 200 µM H_2O_2
200	Addition of 500 µL 0.5 mM Ca^{2+} Ringer's solution with 30 mM DTT
300-Stop	-

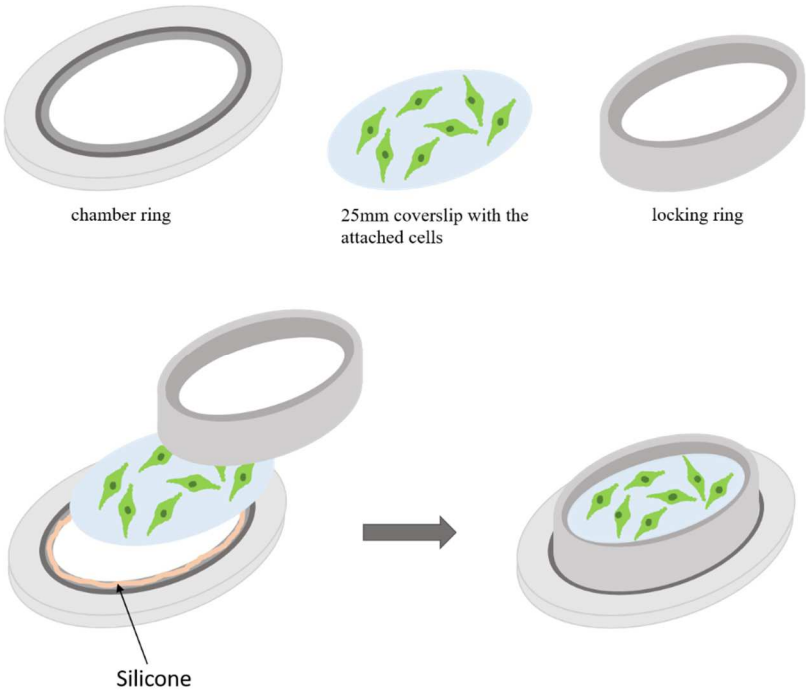

***Figure 18**. Image chamber for cytosolic and mitochondrial H_2O_2, mitochondrial Ca^{2+} and mitochondrial membrane potential measurements. The individual parts that make up the image chamber are shown at the top of the figure. In the lower left corner, the assembly is shown, and in the right, the final result ready to be placed on the microscope.*

4.10. MITOCHONDRIAL PARAMETER MEASUREMENTS

Mitochondrial Ca^{2+}, H_2O_2 and $\Delta\Psi$ measurements were measured using the same imaging system as described for cyto-HyPer (see chapter **4.9.3.)**. In case of fibroblasts it was used the imaging chamber describe in **Figure 18** while to measuring iPS-CM the MyoPacer imaging chamber was used (see chapter **4.9.2.**).

4.10.1. Mitochondrial Ca^{2+} measurements in HSF

Mitochondrial Ca^{2+} imaging was performed using the FRET (fluorescence resonance energy transfer) sensor 4mt-D3cpV (**figure 19**). The mechanism of fluorescence resonance energy transfer is a distance-dependent physical process which consists of a donor fluorophore in an excited electronic state, which may transfer its excitation energy via FRET to a nearby acceptor fluorophore through long-range dipole-dipole interactions, if the donor's emission and the

acceptor's excitation spectra overlap. Concretely, in 4mt-D3cpV, the donor and acceptor fluorophores are CFP and YFP respectively. Both are linked by a calmodulin-M13 domain that enables the detection of Ca^{2+}. Furthermore, the sensor has 4 mitochondrial localization sequences (4mt) that ensure the proper localization in the mitochondrial matrix.

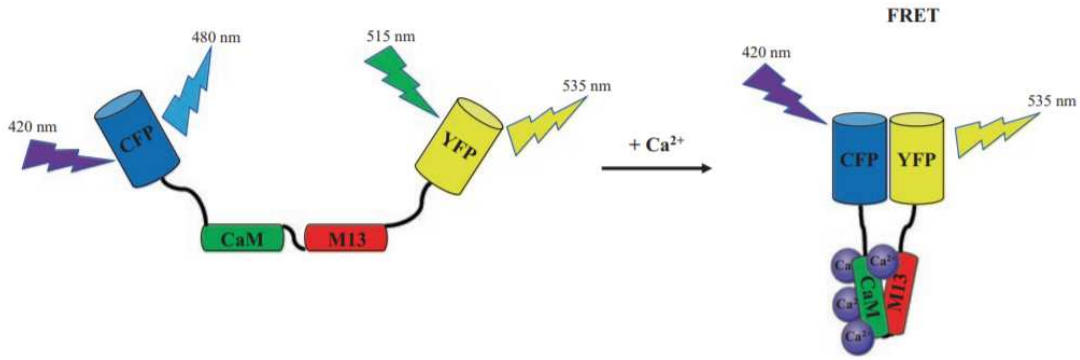

***Figure 19**. D3cpV sensor illustration. D3cpV has CFP as donor fluorophore and YFP as the acceptor fluorophore, which are tagged with 4 mitochondrial localization sequences (4mt; not shown) and fused with calmodulin and MLCK calmodulin binding peptide M13. In presence of Ca^{2+}, Ca^{2+} binds to calmodulin, enabling the interaction with M13-peptide, lowering the distance between the two fluorophores and allowing FRET. (Image taken from Palmer et al., 2006, Chemistry and Biology).*

The cell preparation proceeded exactly as described in chapter **4.9.3.** for the cytH_2O_2 in HSF measurements but using 1 µM of 4mt-D3cpV sensor instead.

The settings used for imaging are described in **Table 23,** and the measurement protocol was performed as described below: it started with 0.5 mM Ca^{2+} Ringer solution to obtain a baseline. Then, an equal volume of 0.5 mM Ca^{2+} Ringer solution with His (in a double concentration of the desired concentration considering the dilution; end concentration for His was 100 µM) was added on top to measure the mCa^{2+} uptake (see **Table 24** for detailed protocol).

For analysis, all transfected cells with the correct localization were used and obtained data were exported and analyzed using Microsoft Excel 2016. Data are presented as average of FRET/CFP ratio over time (minutes) normalized by the background fluorescence.

Table 23. Measurement settings for 4mt-D3cpV imaging of mitochondrial Ca^{2+}.

CFP signal (donor)	excitation: 420 nm (filter: 420/40; 30 % intensity, 56 ms exposure time); emission: CFP filter (dicroic mirror: 458; emission filter: 483/32)
YFP signal (acceptor)	excitation: 505 nm (filter: 500/15; 30% intensity, 8 ms exposure time); emission: YFP filter (dicroic mirror: 520; emission filter: 542/27)
FRET signal	excitaion: 420 nm (filter: 420/40; 30 % intensity, 32 ms exposure time); emission: YFP filter (dicroic mirror: 520; emission filter: 542/27)
Objective	40× oil EC-Plan Neofluar (N.A. 1.3) (for fibroblasts) 40× air Plan Neofluar (N.A.0.75) (for iPSC-CM)
Cycle time	3 sec
Number of cycles	100

Table 24. Protocol for mitochondrial Ca^{2+} measurements of fibroblast.

Number of cycle	**Solution used**
0-Start	500 µL 0.5 mM Ca^{2+} Ringer's solution
40	Addition of 500 µL 0.5 mM Ca^{2+} Ringer's solution with 200 µM His
100-stop	-

4.10.2. Mitochondrial H_2O_2 measurements in HSF

The levels of mitochondrial H_2O_2 (mH_2O_2) were measured by using the protein sensor HyPer (**figure 17**) targeted to the mitochondria (mito-HyPer).

The cell preparation, the protocol, the settings used and the data analysis were exactly the same as $cytH_2O_2$ measurements (see chapter **4.9.3.**). As well the pH sensitivity of mito-HyPer was control by using the pH-sensitive but H_2O_2-insensitive mutant mito-SypHer, using the same experimental settings.

4.10.3. Mitochondrial membrane potential measurements in HSF

Mitochondrial membrane potential measurements were carried out with Tetramethylrhodamin-methylester-perchlorat (TMRM; Sigma-Aldrich, Cat. No. T5428), a fluorescent cell-permeant dye that accumulates in healthy cell with active mitochondria, thereby emitting a red-orange fluorescent signal.

To perform the experiment, cell preparation proceeded exactly as described in section **4.9.1**. For measuring, the cells were stained with 1 µM TMRM solution (100 µM stock solution dissolved in DMSO) in growth medium for 10 minutes at room temperature on a platform shaker.

After incubation of TMRM and after removal of excess medium, the coverslip with the attached cells was assembled in the imaging chamber and the $m\Delta\Psi$ was measured using the settings described in **Table 25.**

As in the previous Ca^{2+} and H_2O_2 measurements, ROIs were selected by using the imaging software. The protocol used for $m\Delta\Psi$ was as following: first, with 0.5 mM Ca^{2+} Ringer solution a baseline was obtained. Then, an equal volume of 0.5 mM Ca^{2+} Ringer solution with 2 µM Carbonyl cyanide m-chlorophenyl hydrazine (CCCP; Sigma-Aldrich, Cat. No. C2759), to have 1 µM CCCP final concentration, was added on top for the induction of mitochondrial membrane depolarization (see **Table 26**).

For the analysis, obtained data were exported to Microsoft Excel 2016 and are presented as arbitrary fluorescence units (background subtracted mean intensity) over time (minutes).

Table 25. Measurement settings for TMRM imaging of mitochondrial membrane potential.

Excitation	white LED ranging from 540 nm – 580 nm (filter: 550/32; 20 % intensity, 2 ms exposure time)
Dichroic mirror	573 nm
Emission	Filter: 630/92
Objective	40× oil EC-Plan Neofluar (N.A. 1.3) (for fibroblasts) 40× air Plan Neofluar (N.A.0.75) (for iPSC-CM)
Cycle time	5 sec (for fibroblasts) / 1 sec (for iPSC-CM)
Number of cycles	150 (for fibroblasts) / 300(for iPSC-CM)

Table 26. Protocol for mitochondrial membrane potential measurements of fibroblast.

Number of cycle	Solution used
0-Start	500 µL 0.5 mM Ca^{2+} Ringer's solution
50	Addition of 500 µL 0.5 mM Ca^{2+} Ringer's solution with 2 µM CCCP
150-stop	-

4.10.4. Mitochondrial membrane potential measurements in Cardiomyocytes

Mitochondrial membrane potential measurements in iPSC-CM were also performed using TMRM dye.

For the cell preparation process, the same protocol was followed as in section **4.9.2**. After having the cells for 6 days at rest, the measurements were performed. For this purpose, iPSC-CM were stained with 1 µM TMRM solution (100 µM stock solution dissolved in DMSO) in growth medium for 10 minutes at room temperature on a platform shaker.

After TMRM incubation and after removal of excess medium, the coverslip with attached cells was assembled in the MyoPacer imaging chamber and mΔΨ was measured using the settings described in **Table 25**. Before starting, ROIs (the iPSC-CM that were successfully loaded with the dye and contracting) were selected using the imaging software.

The protocol used for mΔΨ was as following: first, with 2 mM Ca^{2+} Ringer solution a baseline was obtained. Then, an equal volume of 2 mM Ca^{2+} Ringer solution with 2 µM CCCP was added on top (having a final concentration of 1 µM CCCP) for the induction of mitochondrial membrane depolarization (see **Table 27**).

Table 27. Protocol for mitochondrial membrane potential measurements of cardiomyocytes.

Number of cycle	Solution used
0-Start	500 µL 2 mM Ca^{2+} Ringer's solution
150	Addition of 500 µL 2 mM Ca^{2+} Ringer's solution with 2 µM CCCP
300-stop	-

For the analysis, obtained data were exported to Microsoft Excel 2016 and are presented as arbitrary fluorescence units (background subtracted mean intensity) over time (minutes).

4.11. RESPIRATION MEASUREMENTS

To measure respiration, Seahorse assays were performed using an XF96 Extracellular Flux Analyzer (Seahorse Bioscience, Billerica, MA, USA), getting the oxygen consumption rate (OCR), an indicator of mitochondrial respiration, and the extracellular acidification rate (ECAR), an indicator of glycolysis, in real-time in live fibroblasts.

During the assay, the oxygen consumption rate (OCR) is measured before and after the addition of electron transport chain inhibitors to measure various parameters of mitochondrial respiration. Firstly, baseline cellular OCR is measured. Next oligomycin (Sigma-Aldrich, Cat. No. O4876), an inhibitor of ATP synthase (complex V) is added, which decreases electron flow through the ETC, resulting a reduction in mitochondrial respiration or OCR. This decrease in OCR give information of cellular ATP production. Next, CCCP, an uncoupling agent that collapses the proton gradient and disrupts the $m\Delta\Psi$, is added. Which means that the ETC goes to its maximum rate providing details of the maximal respiratory capacity. Lastly, antimycin A (Sigma-Aldrich, Cat. No. A8674) and rotenone (Sigma-Aldrich, Cat. No. 557368), inhibitors of complex III and I respectively, are added to shut down ETC function, revealing the non-mitochondrial respiration.

In this experiment, respiration in control fibroblasts was compared to fibroblasts treated with mitoQ or OHmitoQ. To do this, before seeding the cells into the Seahorse 96-well plate (XF96 V3-PS, Cat. No. 101085-004). Fibroblasts were incubated for 24 hours with 0.5 µM quinones and the same amount of vehicle (DMSO).

Then, the assay procedure started with the coating of the Seahorse 96-well plate with poly-L-lysine (50 µg/mL; Biochrom, Cat. No. L7240), 20 µL per well. The plate was, then, sealed and kept at 4 °C overnight. Agilent Seahorse XFe96 Extracellular Flux Assay Kit was also calibrated over night at 37 °C (in the Seahorse incubator) with 180 µL XF Calibrant (pH = 7.4) (Cat. No. 100840-000).

Next day, fibroblasts were seeded in normal culture medium in a proper amount to form a monolayer of 90 - 100 % confluence (40.000 cells per well) in the Seahorse 96-well plate. The plate was incubated at 37 °C and 5 % CO_2 for 4 hours.

After the 4 hours incubation, the culture medium was removed and replaced it with 180 µL of Seahorse XF DMEM medium (Agilent, Cat. No. 103575-100) + 10 mM Glucose + 1 mM Na-

pyruvate + 2 mM L-Glutamine. The plate was incubated in the non-CO_2 incubator at 37 °C for at least 45 - 60 minutes to equilibrate.

The drug cartridge was prepared diluting the drugs to their working concentration in XF working medium as described in **Table 28.**

Table 28. Drug dilutions for Seahorse assay.

	Stock Concentration	**Volume of XF Medium**	**Volume of the drug**	**Working concentration**	**Concentration in the Assay**
Oligomycin	50 mM	5 mL	3 µL	30 µM	3 µM
CCCP	100 mM		0.5 µL	10 µM	1 µM
Antimycin A	10 mM		10 µL	10 µM	1 µM
Rotenone	10 mM		10 µL	20 µM	2 µM

The respective drug dilution was poured in a channel plate and load the cartridge using a multichannel pipette.

Port A (Oligomycin): 25 µL

Port B (CCCP): 27.5 µL

Port C (Rotenone + Antimycin A): 30 µL

Then, the prepared cartridge was placed in the XF96 Extracellular Flux Analyzer (Seahorse Bioscience, Billerica, MA, USA). A calibration step is pursued before starting the assay. Afterwards the plate with the cells was inserted into the machine and periodic measurements were performed.

Data analysis were quantified using Microsoft Excel 2016.

4.12. LIPID PEROXIDATION MEASUREMENTS

LPO was measured using the lipophilic fluorescent dye probe BODIPY$^{581/591}$ C11 (4,4-difluoro-5-(4-phenyl-1,3-butadienyl)-4-bora-3a,4a-diaza-s-indacene-3-undecanoic acid; Molecular Probes, Cat. No. D-3861). BODIPY $^{581/591}$ C11 measures the antioxidant activity in lipid environments by exploiting its loss of fluorescence upon interaction with peroxyl radicals.

For the cell preparation process, fibroblasts (100,000) were seeded on 25 mm round glass coverslips with a thickness No. 1.5 24 hours before measuring and in a confluence of 75 – 85 %. Cells were seeded in 2 mL DMEM medium supplemented with 10 % FBS. 6 hours before measuring, fibroblasts were treated with quinones and/or FINs. The quinones were added at a concentration of 0.5 µM and erastin at 5 µM.

Thereafter, cells were loaded with BODIPY$^{581/591}$ C11 at a final concentration of 2 µM (2 mM stock solution dissolved in DMSO) in growth medium for 30 minutes at room temperature on a platform shaker.

After the loading time, the coverslip with the attached cells was assembled in the imaging chamber (**Figure 18**) and the LPO was measured using the same imaging system as described for cyto-HyPer (see chapter **4.9.3**). The settings used for these experiments are described in **Table 29.**

As in the previous measurements done in this imaging system, ROIs were selected by using the imaging software. The protocol used for LPO was as following: first, with 0.5 mM Ca^{2+} Ringer solution a baseline was obtained. Then, an equal volume of 0.5 mM Ca^{2+} Ringer solution with 200 µM H_2O_2, to have 100 µM H_2O_2 final concentration, was added on top (see **Table 30**).

For the analysis, obtained data were exported to Microsoft Excel 2016 and are presented as ratio-fluorescence microscopy of lipid oxidation (ratio 505/555; background subtracted) over time (minutes).

Table 29. Measurement settings for lipid peroxidation in fibroblasts.

OXIDATED	excitation: 505 nm (filter: 500/15; 30 % intensity, 5 ms exposure time); emission: HyPer filter (dichroic mirror: 515; emission filter: 539/25)
REDUCED	excitation: white LED ranging from 540 nm – 580 nm (filter: 550/32; 30 % intensity, 10 ms exposure time); emission: R-GECO filter (dichroic mirror: 573; emission filter: 630/92)
Objective	40× oil EC-Plan Neofluar (N.A. 1.3)
Cycle time	2 sec
Number of cycles	150

Table 30. Protocol for lipid peroxidation measurements of fibroblast.

Number of cycle	**Solution used**
0-Start	500 µL 0.5 mM Ca^{2+} Ringer's solution
50	Addition of 500 µL 0.5 mM Ca^{2+} Ringer's solution with 200 µM H_2O_2
150-Stop	-

5. RESULTS

5.1. ROLE OF CoQ_{10} IN MITOCHONDRIAL Ca^{2+} AND REDOX HOMEOSTASIS IN HSF

Based on the discovery of OH-CoQs and their redox properties that allow them to transfer Ca^{2+} through artificial biomembranes (Bogeski et al., 2011), we investigated the role of CoQ_{10} in mitochondrial Ca^{2+} and redox homeostasis in cell cultures. For this purpose, we established several experimental study models to manipulate CoQ_{10} content in the cell.

5.1.1. First model: Inhibition of CoQ_{10} biosynthesis in HSF

We first depleted CoQ_{10} in primary HSF. This approach was based on a protocol described by Quinzii et al. (Quinzii et al., 2012) in which the drug 4-NB was used to inhibit CoQ_{10} biosynthesis, as described in chapter **4.4.1**.

Initially, we tested whether the inhibition of CoQ_{10} biosynthesis by 4-NB had any effect on mCa^{2+}, measured with 4mt-D3cpV sensor. The protocol consisted on measuring first the basal levels of mCa^{2+} and then the Ca^{2+} uptake capacity of the mitochondria, after histamine addition. The effect of histamine is mediated through receptors that belong to the family of G protein-coupled receptors (GPCR) and when activated, a cascade of second messengers is generated ending in the formation of IP_3, which binds to IP_3R located in the ER membrane, promoting the release of Ca^{2+} from ER Ca^{2+} stores. The increase of Ca^{2+} in areas close to the mitochondria generates a driving force that allows the uptake of Ca^{2+} to the mitochondria (Esbenshade et al., 2003).

In cell depleted for CoQ_{10}, our measurements show an increase in mCa^{2+} at both resting conditions (**Fig. 20, B**) and following cell activation (**Fig. 20, C**). It was confirmed that these changes were due to the inhibition of CoQ_{10} biosynthesis by 4-HB, which recovers the original CoQ_{10} biosynthesis rate. Mitochondrial Ca^{2+} concentration in HSF treated with 4-HB were similar as in the control cells (**Fig. 20**).

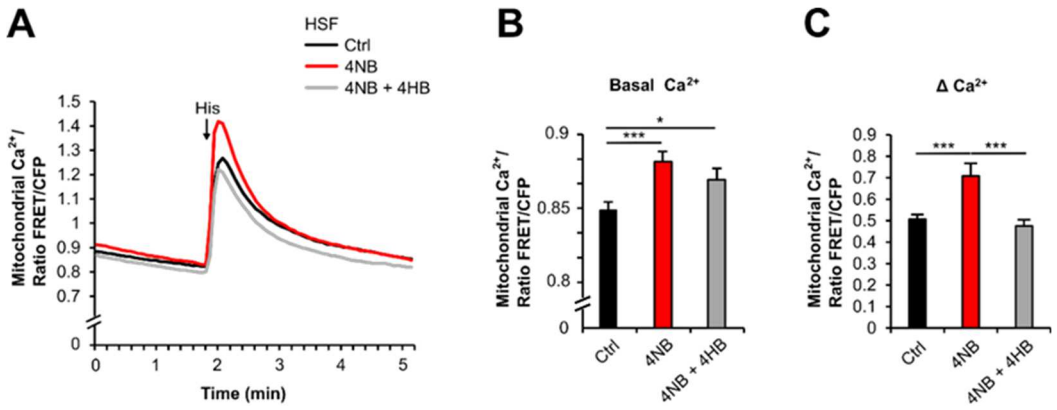

Figure 20. Mitochondrial Ca^{2+} in HSF treated with 4NB and 4NB + 4HB. (A) Data are shown in ratio FRET/CFP over time (min). First basal mitochondrial Ca^{2+} levels are shown. Then, addition of 100 µM histamine to 4mt-D3cpV expressing cells, which results in FRET ratio increase, represents Ca^{2+} uptake to mitochondria. (B) Quantification of basal Ca^{2+} levels in mitochondria. (C) Quantification of Δ values after histamine stimulation (max - min). n values = 284 (Ctrl), 312 (4NB), 230 (4NB + 4 HB) from three independent experiments. Data are presented in mean ± SEM. All P-values were calculated by using Student's t-tests. *p < 0.05; **p < 0.01; ***p < 0.001.

Next, parameters that could have been altered by the decrease in CoQ_{10} and could be responsible for the increase in mCa^{2+}, were tested. We first checked whether cell proliferation and viability were increased, which would cause a greater demand for energy and consequently an increase in mCa^{2+}. Results of CTB assays during 96 hours excluded the hypothesis that the increase in mCa^{2+} was connected with a higher proliferation rate since no differences could be observed between the treatments (**Fig. 21**).

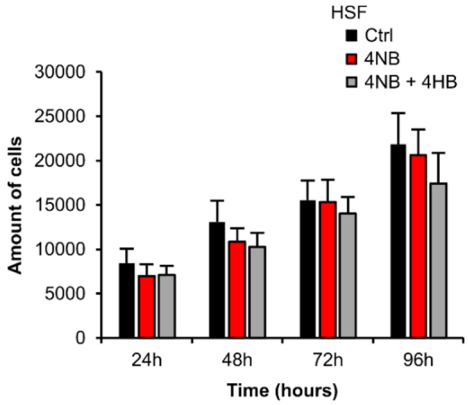

Figure 21. Proliferation and Viability of HSF treated with 4NB and 4NB + 4HB. Proliferation and Viability measured by using the CellTiter-Blue® Cell Viability Assay. The graph represents the number of cells *versus* time, from 24 hours to 96 hours. Data are presented as the mean of seven independent experiments ± SEM (n = 3 wells / each experiment).

The increase in mCa^{2+} could also be explained by an increase in $cytCa^{2+}$. Therefore, we analyzed the expression of genes related to SOCE (ORAI 1-3, STIM 1, 2). Data analysis showed no significant differences as a result of CoQ_{10} reduction (**Fig. 22, B**). In addition, we measured $cytCa^{2+}$ imaging with FURA-2AM. The levels of $cytCa^{2+}$ were monitored by quantifying several parameters such as the basal $cytCa^{2+}$ levels (**Fig. 22, C**), the ER Ca^{2+} store content and depletion following cell activation with histamine (**Fig. 22, D**), as well as SOCE induced by increasing the external Ca^{2+} concentration (**Fig. 22, E**). As there were no significant differences between conditions, we also discarded the idea that the increase in mCa^{2+} is due to variations in $cytCa^{2+}$.

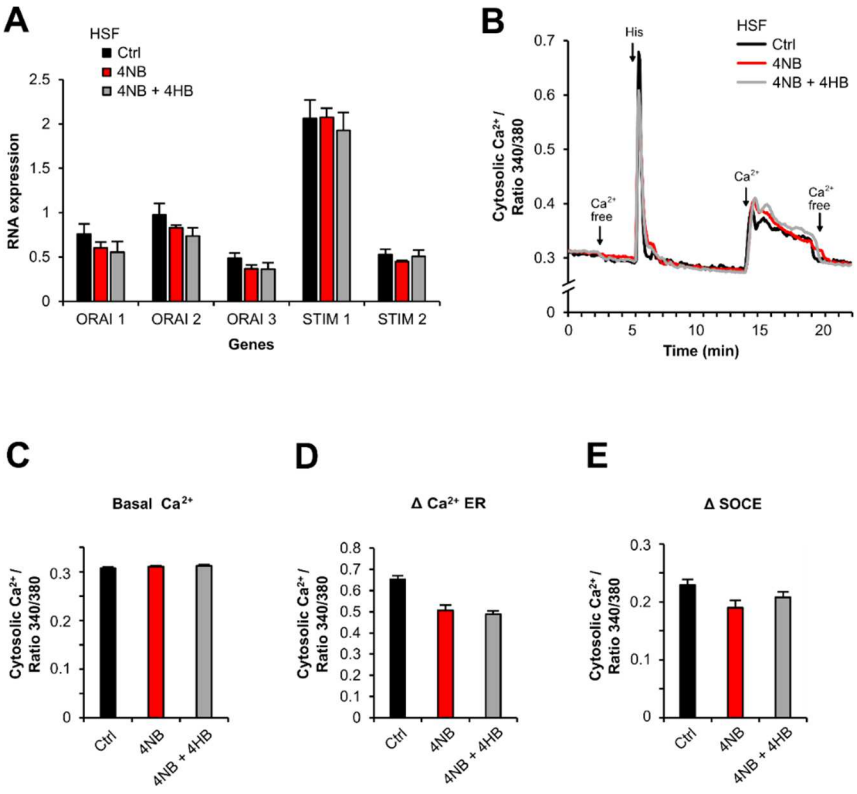

Figure 22. Non-mitochondrial parameters that could affect mitochondrial Ca^{2+} signaling in HSF treated with 4NB and 4NB + 4HB. (A) Relative RNA expression of genes related with SOCE in HSF ctrl and HSF treated with 4NB +/- 4HB. Data are presented as the average of four independent experiments ± SEM (n = 3 wells / each experiment). (B - E) $CytCa^{2+}$ levels measured with FURA - 2 AM of HSF ctrl and HSF treated with 4NB and 4NB + 4HB. (B) The graph represents the fluorescence ratio 340/380 over time (min). First basal $cytCa^{2+}$ levels are shown. Next, addition of 100 µM histamine to FURA - 2 AM loaded cells results in an increase of ratio 340/380, first peak, and the addition of extracellular Ca^{2+} provoke the second peak. (C) Quantification of basal Ca^{2+} levels in the cytosol. (D) Quantification of Δ values after histamine stimulation (max – min), which leads to the depletion of Ca^{2+} from the ER, represents the Ca^{2+} store in the cells. (E) Δ quantification of the second peak (max – min), which is due to Ca^{2+} addition in the buffer, represents SOCE. n values: ctrl = 269, 4NB = 135, 4NB + 4HB = 223;

from one independent experiment. Data are presented in mean ± SEM. All P-values were calculated by using Student's t-tests. *p < 0.05; **p < 0.01; ***p < 0.001.

Given these results, we next examined mitochondrial parameters that could be involved in the increase in mCa^{2+}. First, we measured the mΔΨ with TMRM. We found that a decrease in CoQ_{10} by 4-NB caused an increase in the mΔΨ that was reversed by restoring the content of CoQ_{10} by 4-HB (**Fig. 23, A and B**). This result leaves open the possibility that changes in the mΔΨ are the cause of the variations in Ca^{2+} signaling in HSF.

Furthermore, we determined the expression of genes involved in the MCU complex, the main Ca^{2+} channel in the IMM that allow the uptake of Ca^{2+} to mitochondria. The data showed a decrease in the expression of MCUb, whose function is to block the entry of Ca^{2+} into the mitochondria matrix, suggesting that a greater mCa^{2+} uptake was possible. Besides, no significant differences in the rest of genes, MCUa, MICU1-3, MCUR and EMRE were detected (**Fig. 23, C and D**).

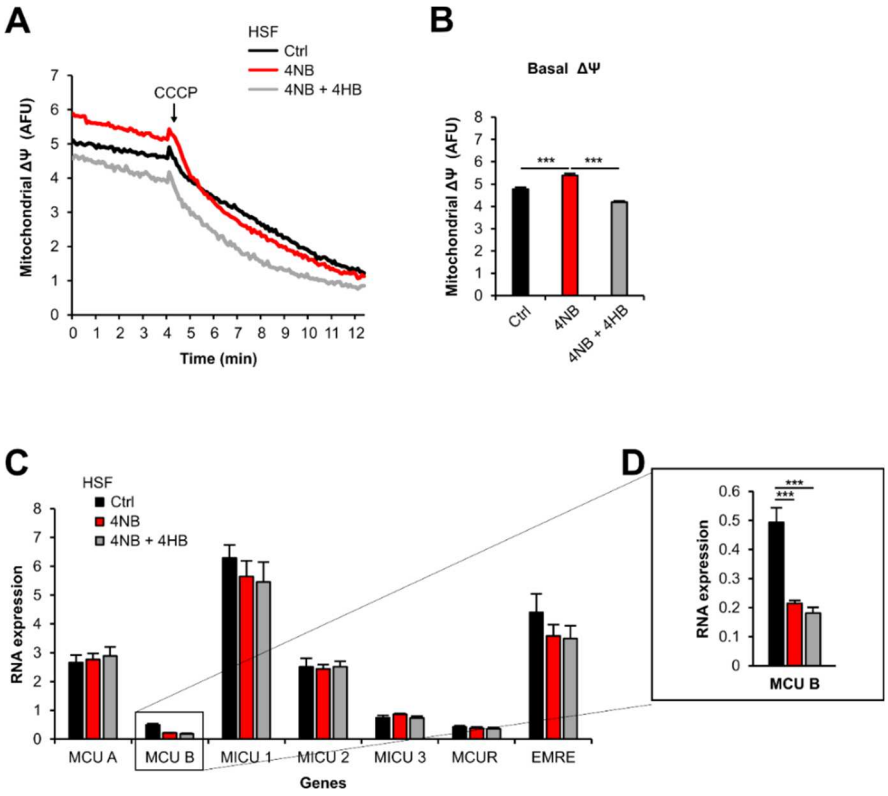

Figure 23. **Mitochondrial parameters that could affect mitochondrial Ca^{2+} signaling in HSF treated with 4NB and 4NB + 4HB.** (A - B) Mitochondria membrane potential measured with TMRM in HSF ctrl and HSF treated with 4NB and 4NB + 4HB. (A) Arbitrary fluorescence units (Intensity mean) over time (min). First, basal values are shown and then, addition of 1 µM CCCP to TMRM loaded cells depolarize the membrane and results in fluorescence decrease.

(B) Quantification of basal mΔΨ values. n values: ctrl = 272, 4NB = 274, 4NB + 4HB = 199; from two independent experiments. (C - D) Relative RNA expression of genes involved in MCU complex of HSF ctrl and HSF treated with 4NB +/- 4HB. (D) Amplification of the graph to show the MCUb values. Data are presented as the average of seven independent experiments ± SEM (n = 2 wells / each experiment). All P-values were calculated by using Student's t-tests. *p < 0.05; **p < 0.01; ***p < 0.001.

Finally, we evaluated mH_2O_2 levels by using HyPer sensor targeted to mitochondria. Addition of H_2O_2 at the end of the experiment was used as a positive control (**Fig. 24, A**). Quantification of basal mH_2O_2 levels did not vary after the reduction of CoQ_{10} between the conditions (**Fig. 24, B**), so we concluded that the decrease in CoQ_{10} by 4-NB did not affect redox signaling in HSF.

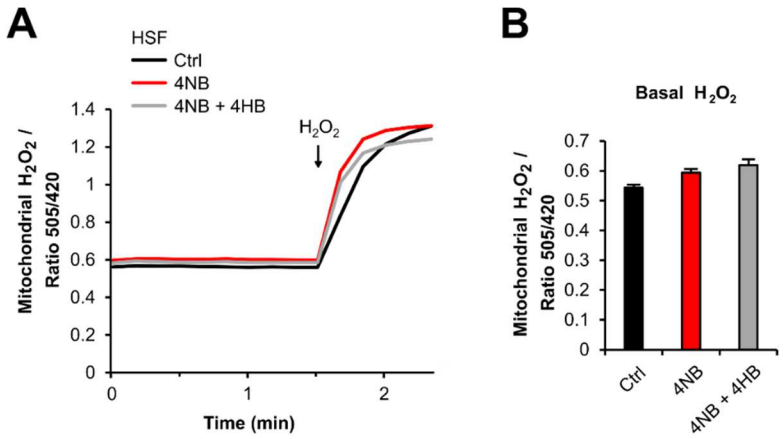

Figure 24. Mitochondrial H_2O_2 imaging measured with mitoHyPer of HSF ctrl and HSF treated with 4-NB or 4-NB + 4-HB. (A) Traces are presented as Ratio fluorescence (505 nm/420 nm) over time (min) with addition of 100 µM H_2O_2 at time 1.5 min, which causes oxidation of the probe and increased the signal ratio. (B) Quantification of H_2O_2 basal levels in mitochondria. n values: ctrl = 131, 4NB = 165, 4NB + 4HB = 149; from three independent experiments. Data are presented in mean ± SEM. All P-values were calculated by using Student's t-tests. *p < 0.05; **p < 0.01; ***p < 0.001.

These results suggest that the decrease in CoQ_{10} by 4-NB in HSF causes an increase in mCa^{2+} probably due to changes in the mΔΨ or changes in the MCU complex.

5.1.2. Second model: Addition of mitoquinones to HSF

In the second experimental model, we approached the study from the opposite perspective. The objective was to increase the concentration of CoQ_{10} in HSF to further clarify its role. Especially, it was sought to increase the content of CoQ_{10} in the mitochondria. For this purpose, we treated the cells with the mitochondrially targeted Coenzyme Q (mitoQ) (Tabara et al., 2014) and its hydroxylated form, OH-mitoQ.

First, we analyzed whether mCa^{2+} levels were affected in HSF once the content of mitochondrial CoQ_{10} had been increased by pre-incubation with mitoQ or OH-mitoQ for 24 hours. As described above, we performed measurements of mCa^{2+} imaging with 4mt-D3cpV (**Fig. 24, A**). Addition of mitoQ significantly decreased basal mCa^{2+} levels, whereas addition of OH-mitoQ increased basal levels of mCa^{2+} (**Fig. 24, B**). Besides, HSF treated with mitoQ resulted in decreased Ca^{2+} uptake to mitochondria after cell activation, but no significant differences in HSF treated with OH-mitoQ *versus* control were detected (**Fig. 24, C**).

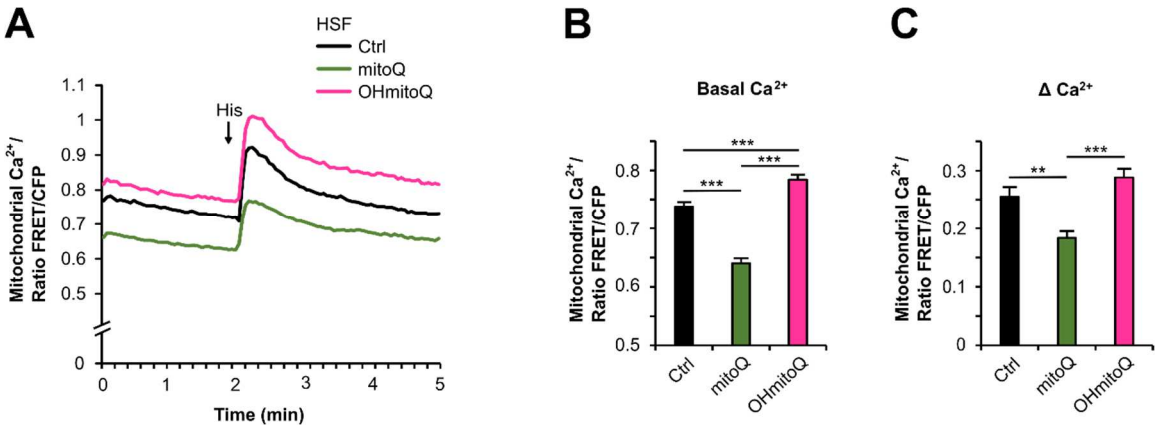

Figure 24. Mitochondrial Ca^{2+} levels in HSF treated with mitoQ and OH-mitoQ during 24 hours. (A) Data are shown in ratio FRET/CFP over time (min). First basal Ca^{2+} levels are shown. Then, addition of 100 µM histamine to 4mt-D3cpV expressing cells, which results in FRET ratio increase, represents Ca^{2+} uptake to mitochondria. (B) Quantification of basal Ca^{2+} levels in mitochondria. (C) Quantification of Δ values after histamine stimulation (max - min). n values: ctrl = 86, mitoQ = 74, OH-mitoQ = 78; from three independent experiments. Data are presented in mean ± SEM. All P-values were calculated by using Student's t-tests. *p < 0.05; **p < 0.01; ***p < 0.001.

Next, we analysed parameters that can influence changes in mCa^{2+} signaling. We started by determining the proliferation and viability of the cells with the CTB assay. We found that mitoQ treatment for 72 hours decreased the proliferation rate by about 35 % in HSF. In contrast, no changes in viability could be observed following OH-mitoQ treatment (**Fig. 25**).

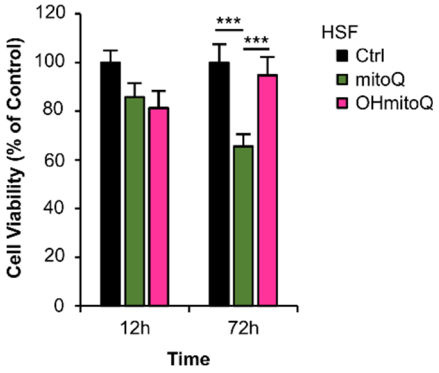

Figure 25. Proliferation and Viability of HSF treated with mitoQ and OH-mitoQ. Proliferation and viability measured by using the CellTiter-Blue® Cell Viability Assay. The graph represents cell viability (% of control) *versus* time (in 12 h and 72 h). Data are presented as the average of four independent experiments ± SEM (n = 3 wells / each experiment). All P-values were calculated by using Student's t-tests. *p < 0.05; **p < 0.01; ***p < 0.001.

Since an increase in mCa^{2+} could be explained by an increase in $cytCa^{2+}$, we next measured $cytCa^{2+}$ levels with FURA-2AM. The measuring protocol was the same that we used in the previous model but thapsigargin was used to deplete the ER Ca^{2+} stores instead of histamine. Thapsigargin is a compound isolated from a specific plant that is a cell permeable inhibitor of SERCA which inhibition leads to depletion of ER Ca^{2+} stores, consequently increasing $cytCa^{2+}$ (Rasmussen et al., 1978). Interestingly, in this experimental model we found that increased mitochondrial CoQ_{10} content due to the addition of mitoQ for 24 hours, affected $cytCa^{2+}$ signal. Data showed that the basal $cytCa^{2+}$ levels, Ca^{2+} storage in the ER, as well as SOCE were strongly reduced. By contrast, OH-mitoQ treatment did not affect basal $cytCa^{2+}$ values in comparison with control HSF, but Ca^{2+} storage in ER and SOCE were both increased (**Fig. 26, A-D**). These results could explain our results in mCa^{2+}signaling.

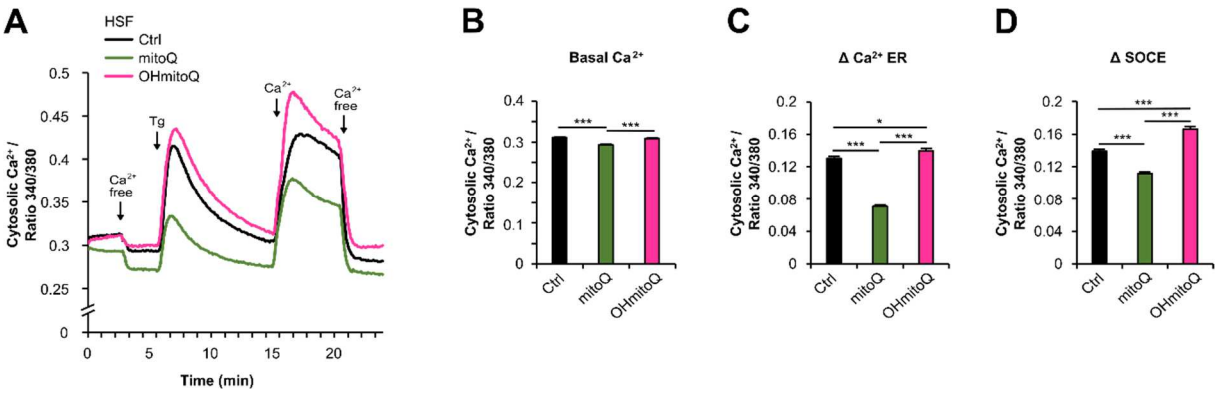

Figure 26. Cytosolic Ca^{2+} levels in HSF treated with mitoQ and OH-mitoQ during 24 hours. (A) The graph represents the fluorescence ratio 340/380 over time (min). First basal Ca^{2+} levels are shown. Next, addition of 1 µM thapsigargin to FURA - 2 AM loaded cells results in an increase of ratio 340/380, first peak, and the addition of extracellular Ca^{2+} provoke the second peak. Last, addition of free Ca^{2+} buffer decreases to minimum the ratio fluorescence. (B) Quantification of basal Ca^{2+} levels in the cytosol. (C) Quantification of Δ values after thapsigargin stimulation (max – min), which leads to the depletion of Ca^{2+} from the ER, represents the Ca^{2+} store in the cells. (D) Δ quantification of the second peak (max – min), which is due to Ca^{2+} addition in the buffer and represents SOCE. n values: ctrl = 487, mitoQ = 378, OH-mitoQ = 222; from at least three independent experiments. Data are presented in mean ± SEM. All P-values were calculated by using Student's t-tests. *p < 0.05; **p < 0.01; ***p < 0.001.

In addition, mitochondrial parameters were tested. First, we measured mΔΨ with TMRM. Data analysis showed that the treatment with mitoQ for 24 hours in HSF caused strong depolarization of the membrane and by contrast, OH-mitoQ did not provoke any change (**Fig. 27, A-B**). Acute addition of mitoQ confirmed its negative effect on the mΔΨ. Similar as after 24 hours pretreatment, acute addition of OH-mitoQ did not alter the potential (**Fig. 27, C-D**). Furthermore, the mitoQ-induced decrease in mΔΨ was dose-dependent (**Fig. 27, E-H**).

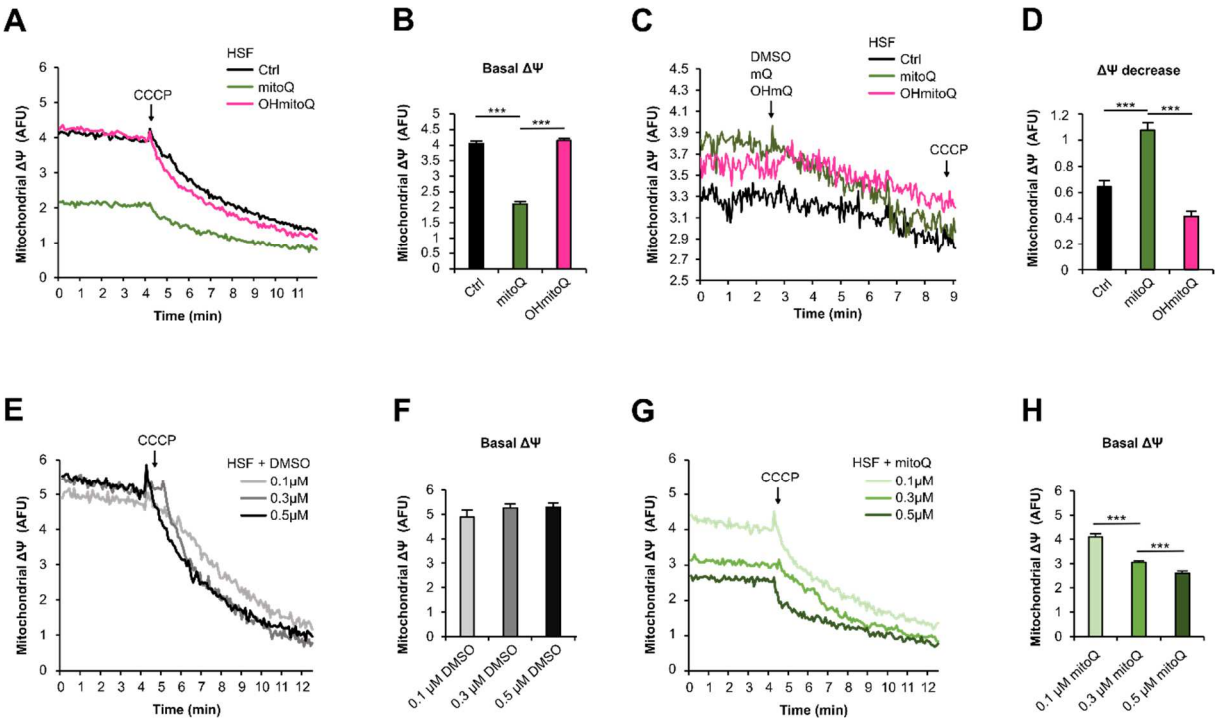

Figure 27. Mitochondrial membrane potential in HSF treated with mitoQ and OH-mitoQ. (A, B) Mitochondria membrane potential of HSF ctrl and HSF treated with mitoQ and OHmitoQ during 24 hours. (A) Arbitrary fluorescence units (Intensity mean) over time (min). First, basal values are shown and then, addition of 1 μM CCCP to TMRM loaded cells depolarize the membrane and results in fluorescence decrease. (B) Quantification of basal mΔΨ values. n values: ctrl = 147, mitoQ = 199, OH-mitoQ = 200; from two independent experiments. (C, D) Acute effect of mitoQ and OH-mitoQ addition. (C) Arbitrary fluorescence units (Intensity mean) over time (min). First, basal values are shown and then, addition of 1 μM CCCP to TMRM loaded cells depolarize the membrane and results in fluorescence decrease. (D) Quantification of mΔΨ decrease due to the quinones (values before adding the quinones (min 3) – values before adding CCCP (min 9)). n values: ctrl = 90, mitoQ = 64, OH-mitoQ = 120; from two independent experiments. (E, F) Mitochondrial membrane potential of HSF treated with several concentrations of DMSO, as control, during 24 hours. (E) Arbitrary fluorescence units (Intensity mean) over time (min). First, basal values are shown and then, addition of 1 μM CCCP to TMRM loaded cells depolarize the membrane and results in fluorescence decrease. (F) Quantification of basal mΔΨ values. n values: 0.1 μM DMSO = 34, 0.3 μM DMSO = 46, 0.5 μM DMSO = 48; from one independent experiments. (G, H) Mitochondrial membrane potential of HSF treated with several concentrations of mitoQ, during 24 hours. (G) Arbitrary fluorescence units (Intensity mean) over time (min). First, basal values are shown and then, addition of 1 μM CCCP to TMRM loaded cells depolarize the membrane and results in fluorescence decrease. (H) Quantification of mΔΨ potential values. n values: 0.1 μM mitoQ = 106, 0.3 μM mitoQ = 99, 0.5 μM mitoQ = 102; from one independent experiments. Data are presented in mean ± SEM. All P-values were calculated by using Student's t-tests. *p < 0.05; **p < 0.01; ***p < 0.001.

MCU complex gene expression was no affected in HSF treated with mitoQ and OH-mitoQ (**Fig. 28, A**). As confirmation, WB analyses were performed which revealed increased protein levels of MCUb and MICU3 and a slight decrease in MICU2, in addition to no changes in MCUa, caused by both mito-CoQs individually. (**Fig. 28, B-F**). Since this effect was very small and the same occurred with both mito-CoQs, the opposite effect that they induced in mCa^{2+} can hardly be explained by changes in protein expression of MCU complex.

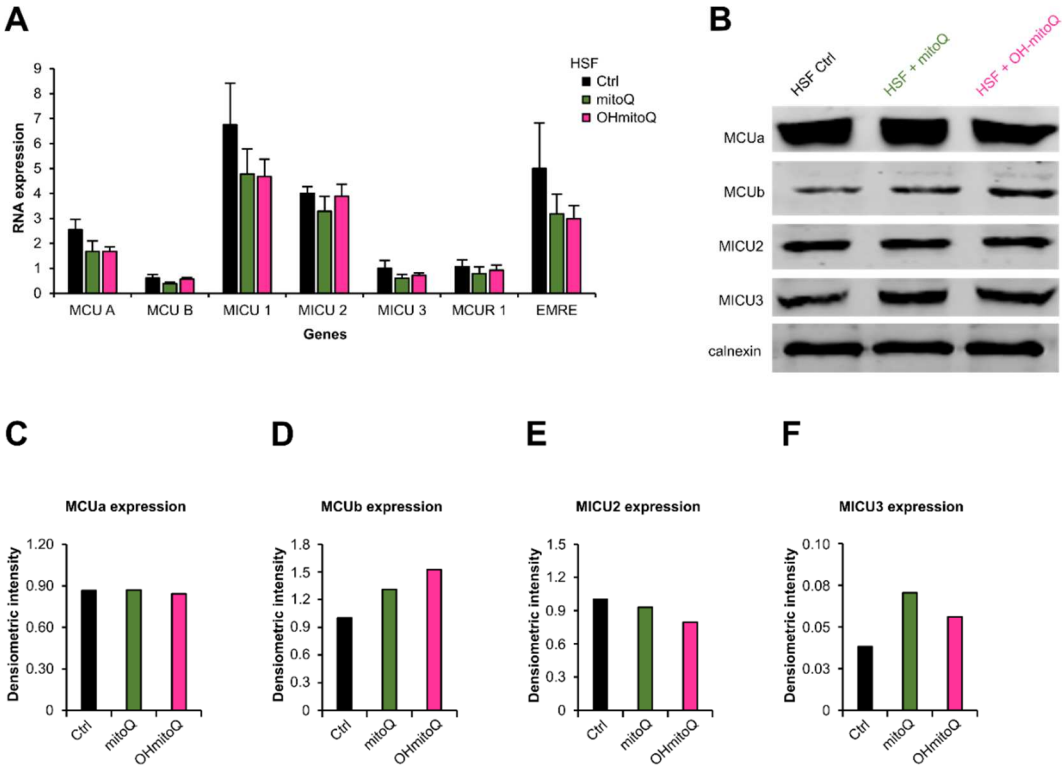

Figure 28. MCU complex expression in HSF treated with mitoQ and OH-mitoQ during 24 hours. (A) Relative RNA expression of genes involved in MCU complex in HSF ctrl and HSF treated with mitoQ and OH-mitoQ. Data are presented as the average of four independent experiments ± SEM (n = 2 wells / each experiment). All P-values were calculated by using Student's t-tests. *p < 0.05; **p < 0.01; ***p < 0.001. (B - F) Protein expression of MCU complex in HSF ctrl and HSF treated with mitoQ and OH-mitoQ. From C to F is presented the quantification (MCUa (C), MCUb (D), MICU2 (E), MICU3(F)), each graph shows the density of each band normalized by that of calnexin. n = 1.

We next checked if the mitochondrial bioenergetic output is affected by mito-CoQs treatment. For this purpose, Seahorse assays were performed, in which several inhibitors of the ETC were added, allowing the measurement of various mitochondrial respiration parameters (described in chapter **4.11**). After 24 hours of mitoQ treatment, basal respiration almost reached minimum values, maximum respiratory capacity was robustly reduced and ATP-linked respiration was

also decreased by about four-folds. These changes did not occur with the OH-mitoQ treatment, which maintained levels similar to those of the control HSF (**Fig. 29, A-D**). Analysis of ECAR determined that the cellular metabolism changed to a more glycolytic state after treatment with mitoQ (**Fig. 29, E-F**).

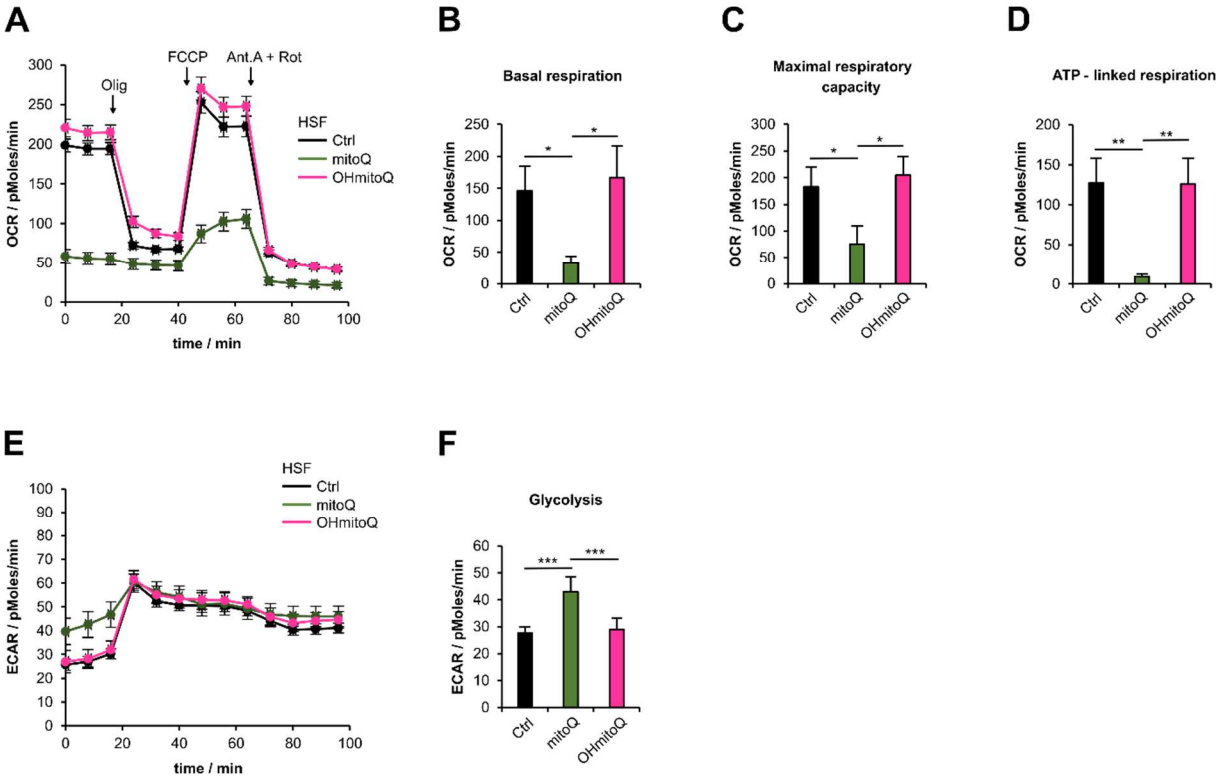

Figure 29. Mitochondrial and non-mitochondrial respiration in HSF treated with mitoQ and OH-mitoQ during 24 hours. (A) OCR levels versus time (min) comparing HSF ctrl and HSF treated with mitoQ or OH-mitoQ. Three injections of several compounds, oligomycin, FCCP, and antimycin A + rotenone, delimits four time intervals within each of which OCR is roughly constant. Basal respiration is the value just before oligomycin injection, minimal respiration is the lowest value after oligomycin injection, and maximal respiration is the highest value after FCCP injection. ATP-linked respiration, is a measure of the capacity of the cell to meet its energetic demands (basal respiration – minimal respiration). All values were calculated after subtraction of non-mitochondrial respiration (values after antimycin A + rotenone injection). Quantification of basal (B) and maximal (C) OCRs and ATP-linked respiration (D) in HSF ctrl and HSF treated with mitoQ and OH-mitoQ. Data are presented as the mean of five independent experiments ± SEM (n = 8 wells / each experiment). (E-F). ECAR levels versus time (min) of HSF control and HSF treated with mitoQ or OH-mitoQ. (F) Quantification of basal values. Data are presented as the mean of two independent experiments ± SEM. (n = 8 wells / each experiment). All P-values were calculated by using Student's t-tests. *p < 0.05; **p < 0.01; ***p < 0.001.

In addition, we determined mH_2O_2 levels by using HyPer sensor targeted to mitochondria. First, we measured basal levels of mH_2O_2, then, addition of H_2O_2 (to oxidize the sensor) and DTT (to reduce the sensor) were used as positive control. HSF were pre-incubated for 24 hours with mitoQ or OH-mitoQ and the antioxidant effect of both mito-CoQs was tested (**Fig. 30, A**). As seen in **Fig. 30, B**, basal mH_2O_2 levels were markedly lower after OH-mitoQ treatment and even lower with mitoQ in comparison to control HSF. Quantification of Δ mH_2O_2 showed that the oxidation of the sensor was lower after pre-incubation with mito-CoQs (**Fig. 30, C**), probably due to the fact that the mito-CoQs are still in the mitochondria and continue to act as scavengers of H_2O_2.

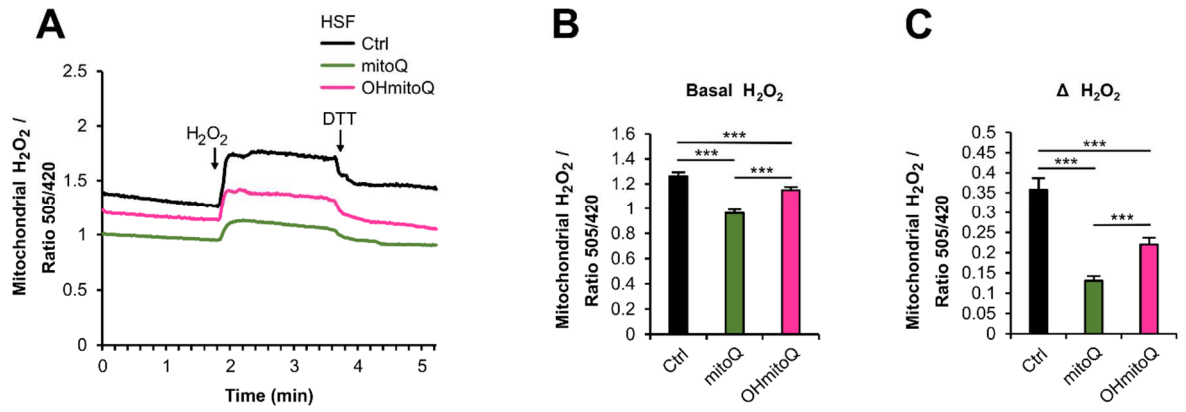

Figure 30. Mitochondrial H_2O_2 in HSF treated with mitoQ or OH-mitoQ during 24 hours. (A) Traces are presented as Ratio fluorescence (505 nm/420 nm) over time (min), addition of 100 µM H_2O_2 at time 2 min, causes oxidation of the probe and increased the signal ratio; addition of 10 mM DTT at time 4min, reduced the probe. (B) Quantification of H_2O_2 basal levels in mitochondria. (C) Quantification of Δ H_2O_2 (max- basal). n values: ctrl = 107, mitoQ = 97, OH-mitoQ = 143; from three independent experiments. Data are presented in mean ± SEM. All P-values were calculated by using Student's t-tests. *p < 0.05; **p < 0.01; ***p < 0.001.

Lastly, we analyzed cytosolic H_2O_2 ($cytH_2O_2$) levels by performing the same protocol as for mH_2O_2 using HyPer3 sensor (**Fig. 31, A**). HSF were also pre-incubated for 24 hours with mitoQ or OH-mitoQ. As depicted in **Fig. 31, B** quantification of basal $cytH_2O_2$ levels showed no differences between the mitoQ or OH-mitoQ pre-incubation when compared to the control treated cells.

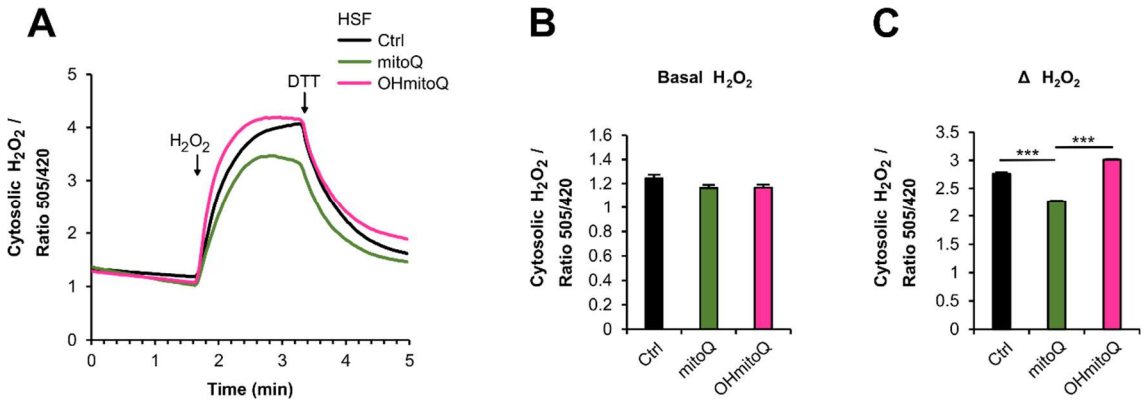

Figure 31. Cytosolic H_2O_2 in HSF treated with mitoQ and OH-mitoQ during 24 hours. (A) Traces are presented as Ratio fluorescence (505 nm/420 nm) over time (min) with addition of 100 µM H_2O_2 at time 2 min, which causes oxidation of the probe and increased the signal ratio; and 10 mM DTT at time 4 min, which reduced the probe. (B) Quantification of H_2O_2 basal levels in the cytosol. (C) Quantification of Δ H_2O_2 (max- basal). n values: ctrl = 57, mitoQ = 30, OH-mitoQ = 35; from three independent experiments. Data are presented in mean ± SEM. All P-values were calculated by using Student's t-tests. *p < 0.05; **p < 0.01; ***p < 0.001.

With the second experimental model we can conclude that mito-CoQs affect mCa^{2+} most likely via regulation of SOCE and the mΔΨ, and they might also be affecting mH_2O_2 signaling preserving their antioxidant role.

5.1.3. Third model: addition of mitoquinones to CoQ_{10} deficient fibroblasts

In the third model, we used HSF derived from two patients with a genetic deficiency in CoQ_{10} (named P104 and P106). By adding mitoQ and OH-mitoQ for 24 hours to the cell culture, we aimed to replenish CoQ_{10} and test the pharmacological properties of the two mito-CoQs.

First, we tested mCa^{2+} once mito-CoQs were added. Mitochondrial Ca^{2+} imaging, measured with 4mt-D3cpV sensor in P104 treated with mitoQ and OH-mitoQ, determined that addition of mitoQ decreased the basal mCa^{2+} levels, whereas the addition of OH-mitoQ did not alter the basal levels of mCa^{2+}. Furthermore, mitoQ treatment resulted in decreased Ca^{2+} uptake to mitochondria after cell activation in P104, but no significant differences were observed in OH-mitoQ-treated P104 (**Fig. 32, A-C**). Although this result was not statistically significant, in P106, the trend was almost the same (**Fig. 32, D-F**).

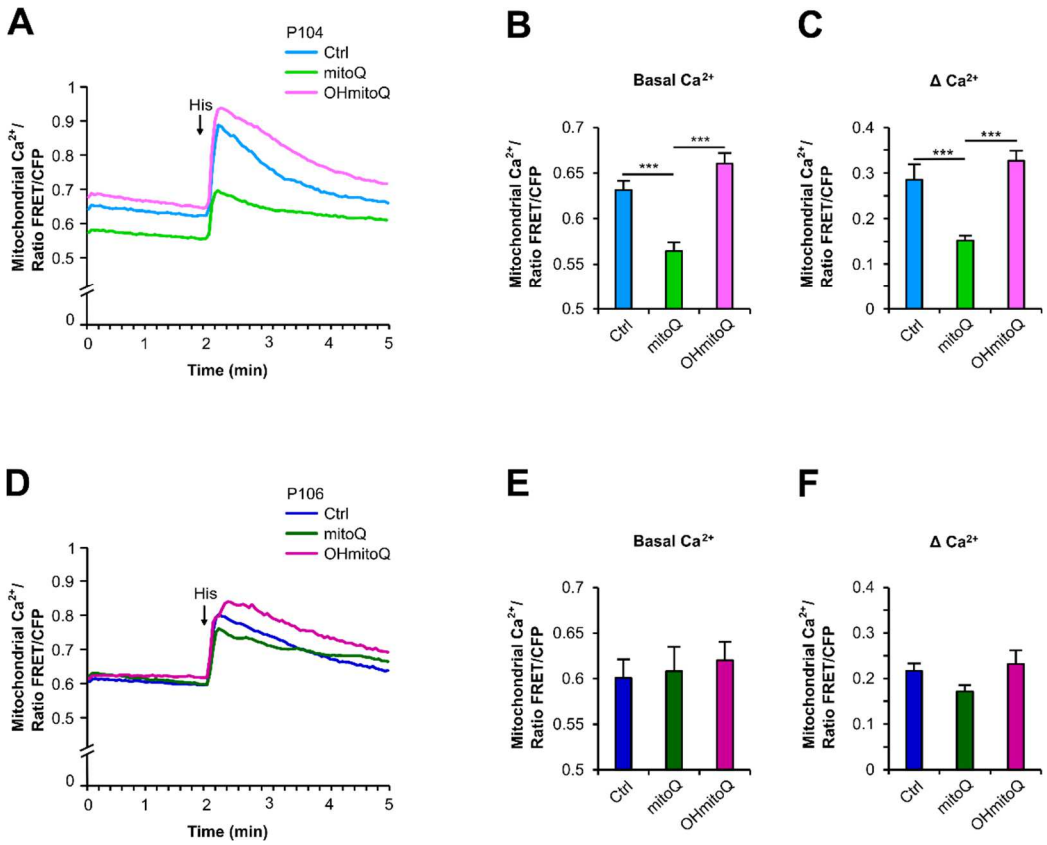

Figure 32. Mitochondrial Ca^{2+} in P104 and P106 treated with mitoQ and OH-mitoQ during 24 hours. (A-C) Mitochondrial Ca^{2+} levels in P104; (D-F) mitochondrial Ca^{2+} levels in P106. (A, D) Ratio FRET/CFP over time (min). First basal mCa^{2+} levels are shown. Then, addition of 100 µM histamine to 4mt-D3cpV expressing cells results in FRET ratio increase, which represent the Ca^{2+} uptake to mitochondria (B, E) Quantification of basal Ca^{2+} levels in mitochondria. (C, F) Quantification of Δ values after histamine stimulation (max - min). n values: P104 ctrl = 94, P104 + mitoQ = 78, P104 + OH-mitoQ = 75, P106 ctrl = 29, P106 + mitoQ = 24, P106 + OH-mitoQ = 37; from at least three independent experiments. Data are presented in mean ± SEM. All P-values were calculated by using Student's t-tests. *p < 0.05; **p < 0.01; ***p < 0.001.

Furthermore, in this experimental model addition of mitoQ did also affect Ca^{2+} signaling at the cytosolic level. Curiously, $cytCa^{2+}$ imaging experiments with FURA-2 AM determined that basal $cytCa^{2+}$ levels in P104 were not altered after the addition of mitoQ, although they were significantly reduced in P106. Besides, ER Ca^{2+} store and SOCE were remarkably reduced in both P104 and P106. By contrast, the treatment of P104 and P106 with OH-mitoQ practically did not modify the basal values of $cytCa^{2+}$, the storage of Ca^{2+} in ER or SOCE in comparison to the untreated fibroblasts (**Fig. 33**).

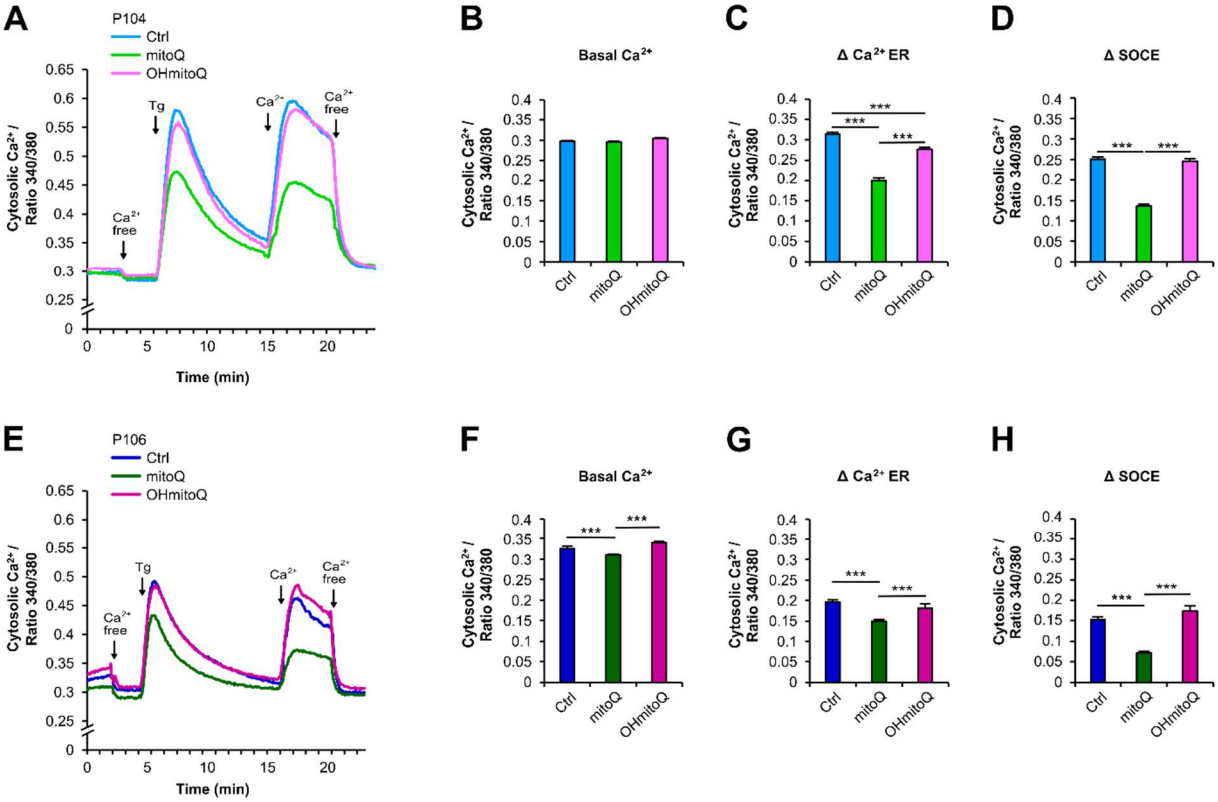

Figure 33. Cytosolic Ca^{2+} levels in P104 and P106 treated with mitoQ or OH-mitoQ during 24 hours. (A-D) Results of cytosolic Ca^{2+} measurements in P104; (E-H) results of cytosolic Ca^{2+} measurements in P106. (A, E) The graph represents the fluorescence ratio 340/380 over time (min). First basal cytCa^{2+} levels are shown. Then, addition of 1 µM thapsigargin to FURA - 2 AM loaded cells results in an increase of ratio 340/380, first peak, and the addition of extracellular Ca^{2+} provoke the second peak. Last, addition of free Ca^{2+} buffer decreases to minimum the ratio fluorescence. (B, F) Quantification of basal Ca^{2+} levels in the cytosol. (C, G) Quantification of Δ values after thapsigargin stimulation (max – min), which leads to the depletion of Ca^{2+} from the ER, represents the Ca^{2+} store in the cells. (D, H) Δ quantification of the second peak (max – min), which is due to Ca^{2+} addition in the buffer and represents SOCE. n values: P104 ctrl = 209, P104 + mitoQ = 116, P104 + OH-mitoQ = 169, P106 ctrl = 60, P106 + mitoQ = 56, P106 + OH-mitoQ = 23; from three independent experiments. Data are presented in mean ± SEM. All P-values were calculated by using Student's t-tests. *p < 0.05; **p < 0.01; ***p < 0.001.

In order to determine if changes in mΔΨ were due to treatment with mitoQ or OH-mitoQ, we performed experiments using TMRM. MitoQ treatment caused almost total depolarization of the membrane in both fibroblasts, P104 and P106, whereas OH-mitoQ provoked a smaller reduction in P104 and no changes in P106 in comparison to control cells (**Fig. 34**).

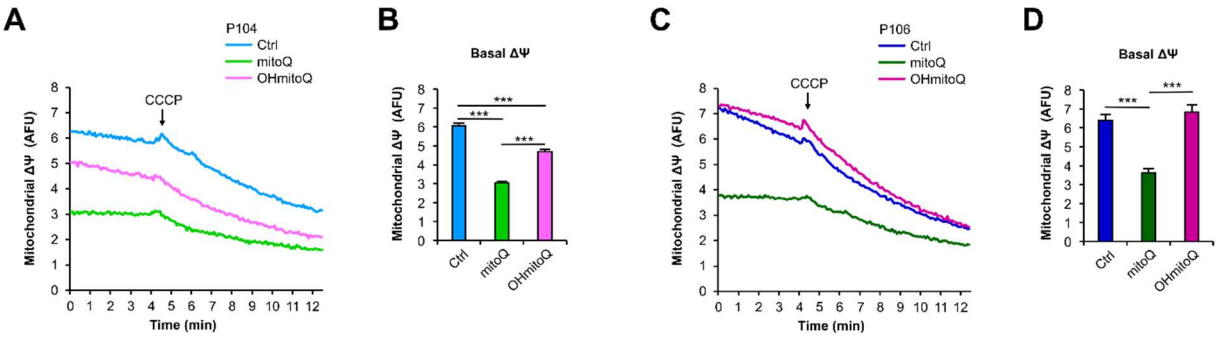

Figure 34. Mitochondrial membrane potential in P104 and P106 treated with mitoQ or OH-mitoQ during 24 hours. (A, B) Mitochondria membrane potential of P104 ctrl and P104 treated with mitoQ and OHmitoQ during 24 hours. (A) Arbitrary fluorescence units (Intensity mean) over time (min). First, basal values are shown and then, addition of 1 µM CCCP to TMRM loaded cells depolarize the membrane and results in fluorescence decrease. (B) Quantification of basal mΔΨ values. n values: P104 ctrl = 118, P104 + mitoQ = 137, P104 + OH-mitoQ = 89. (C, D) Mitochondria membrane potential of P106 ctrl and P106 treated with mitoQ and OHmitoQ during 24 hours. (C) Arbitrary fluorescence units (Intensity mean) over time (min). First, basal values are showed and then, addition of 1 µM CCCP to TMRM loaded cells depolarize the membrane and results in fluorescence decrease. (D) Quantification of basal mΔΨ values. n values: P106 ctrl =53, P106 + mitoQ = 48, P106 + OH-mitoQ = 48. Data are collected from two independent experiments and are presented in mean ± SEM. All P-values were calculated by using Student's t-tests. *p < 0.05; **p < 0.01; ***p < 0.001.

Afterwards, using Seahorse assays, we checked if mitochondrial respiration is affected by mito-CoQs treatment. The results showed that due to mitoQ treatment, basal respiration nearly reached 0 values, maximum respiratory capacity was drastically reduced and ATP-linked respiration was also significantly decreased in both fibroblasts. Conversely, OH-mitoQ treatment did not alter mitochondrial respiration (**Fig. 35**).

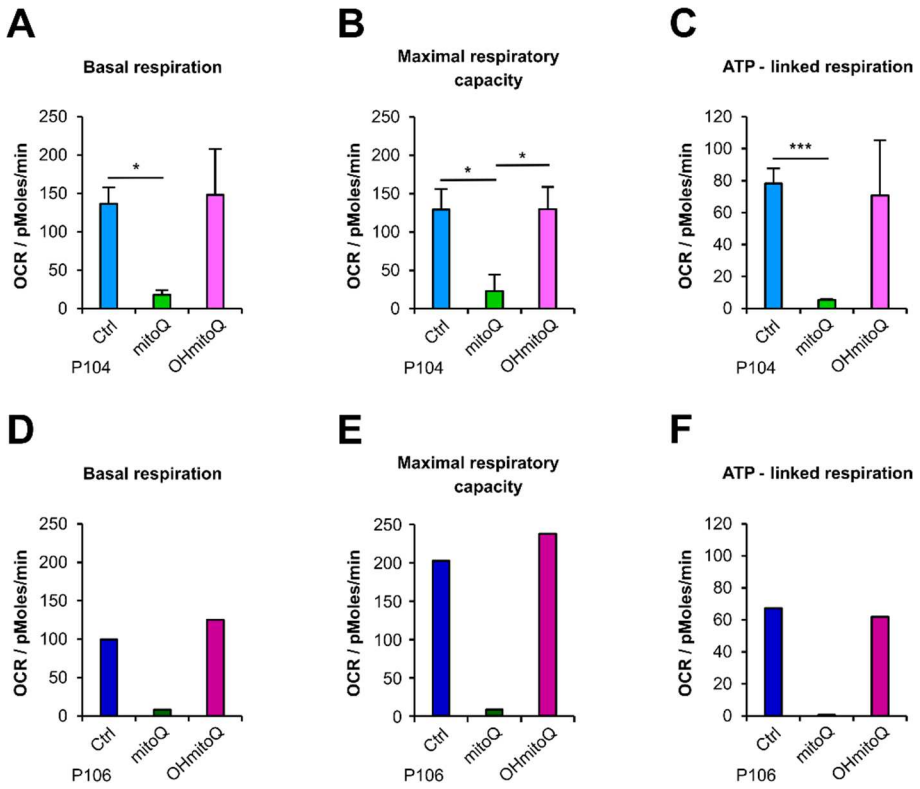

Figure 35. Mitochondrial and non-mitochondrial respiration in P104 and P106 treated with mitoQ and OH-mitoQ during 24 hours. (A) Quantification of OCR basal levels of P104 ctrl and P104 treated with mitoQ or OH-mitoQ. (B) Quantification of maximal respiration capacity after FCCP injection of P104 ctrl and P104 treated with mitoQ or OH-mitoQ. (C) Quantification of ATP-linked respiration which was calculated by doing basal respiration – minimal respiration. Being minimal respiration, the lowest value after oligomycin injection. The graph shows values of P104 ctrl and P104 treated with mitoQ or OH-mitoQ. (D) Quantification of OCR basal levels of P106 ctrl and P106 treated with mitoQ or OH-mitoQ. (E) Quantification of maximal respiration capacity after FCCP injection of P106 ctrl and P106 treated with mitoQ or OH-mitoQ. (F) Quantification of ATP-linked respiration which was calculated by doing basal respiration – minimal respiration. Being minimal respiration, the lowest value after oligomycin injection. The graph shows values of P106 ctrl and P106 treated with mitoQ or OH-mitoQ. All values were calculated after subtraction of non-mitochondrial respiration (values after antimycin A + rotenone injection). For P104, data are presented as the average of three independent experiments ± SEM (n = 8 wells / each experiment). For P106, data are presented as an individual experiment (n = 8 wells). All P-values were calculated by using Student's t-tests. *p < 0.05; **p < 0.01; ***p < 0.001.

Next, as well as for HSF, we analyzed mH_2O_2 levels by using HyPer sensor targeted to mitochondria. P104 and P106 were pre-incubated for 24 hours with mitoQ or OH-mitoQ and the antioxidant effect of both mito-CoQs was tested (**Fig. 36, A, D**). Basal mH_2O_2 levels were lower after OH-mitoQ treatment in P104 and P106 and even lower with mitoQ, as depicted in **Fig. 36, B and E**, respectively. Quantification of ΔH_2O_2 showed that the oxidation of the sensor

was lower after pre-incubation with mito-CoQs (**Fig. 30, C, F**), proving their strong role as H_2O_2 scavengers.

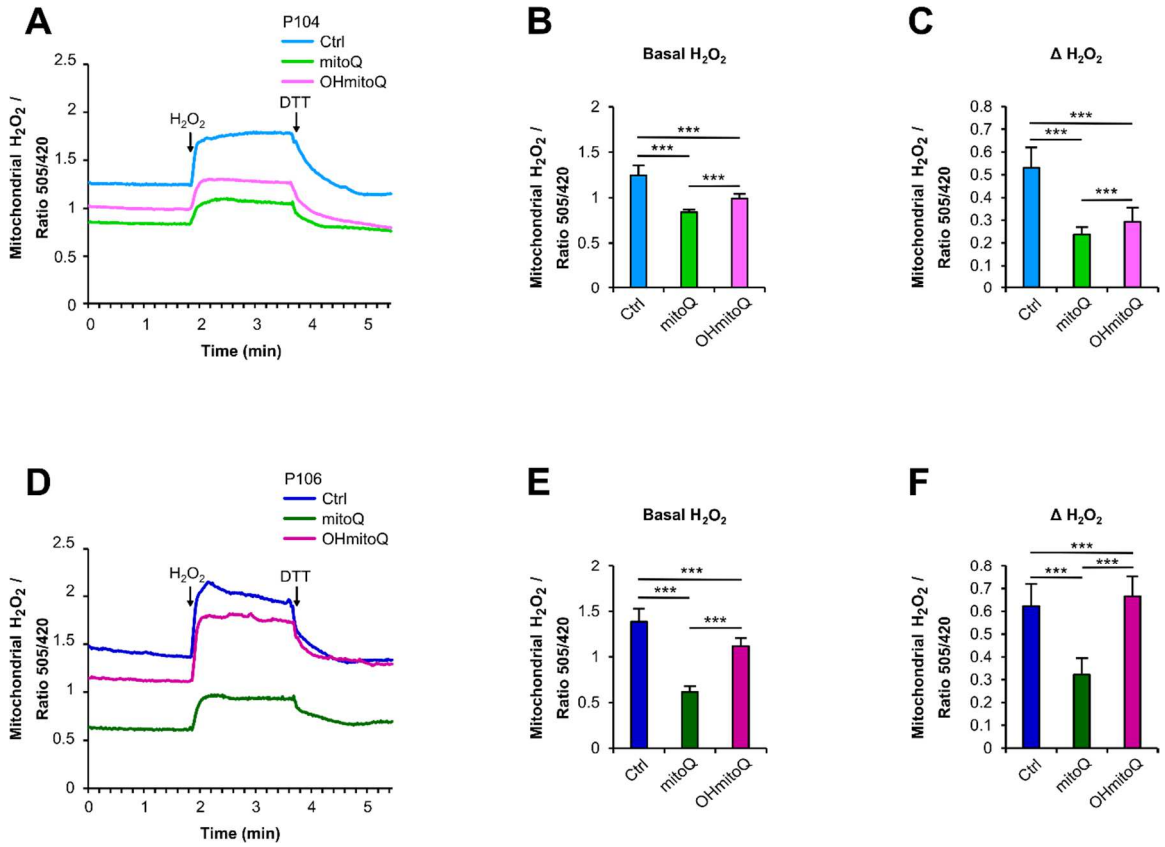

Figure 36. Mitochondrial H_2O_2 in P104 and P106 treated with mitoQ or OH-mitoQ during 24 hours. (A-C) H_2O_2 imaging in P104; (D-F) H_2O_2 imaging in P106. (A, D) Traces are presented as Ratio fluorescence (505 nm/420 nm) over time (min), addition of 100 µM H_2O_2 at time 2 min, causes oxidation of the probe and increased the signal ratio; addition of 10 mM DTT at time 4 min, reduced the probe. (B, E) Quantification of H_2O_2 basal levels in mitochondria. (C, F) Quantification of Δ H_2O_2 (max- basal). n values: P104 ctrl = 37, P104 + mitoQ = 29, P104 + OH-mitoQ = 45, P106 ctrl =18, P106 + mitoQ = 20, P106 + OH-mitoQ = 28; from three independent experiments. Data are presented in mean ± SEM. All P-values were calculated by using Student's t-tests. *p < 0.05; **p < 0.01; ***p < 0.001.

Last, we analyzed the expression of genes involved in the MCU complex, comparing HSF, P104 and P106. Although HSF cannot be considered an adequate control since each fibroblast comes from a different individual, we were able to discard large changes due to big variations in the Ca^{2+} channel itself. The data showed no statistically significant differences between the three cell lines (**Fig. 37**).

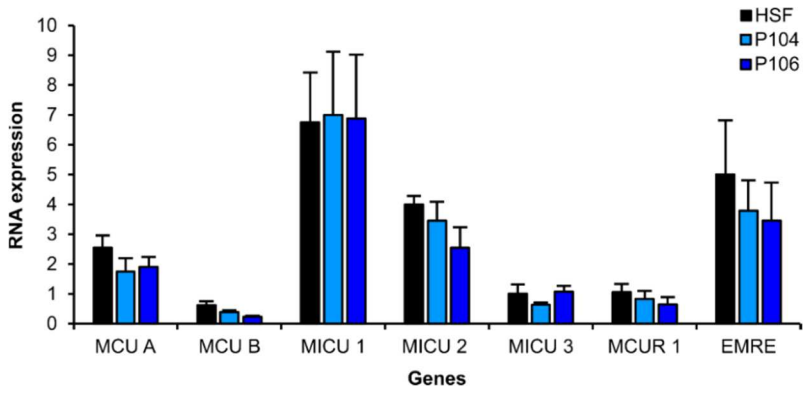

Figure 37. MCU complex expression in HSF, P104 and P106. Relative RNA expression of genes involved in MCU complex in HSF, P104 and P106. Data are presented as the average of three independent experiments ± SEM (n = 2 wells / each experiment). All P-values were calculated by using Student's t-tests. *p < 0.05; **p < 0.01; ***p < 0.001.

The third experimental model strongly suggests that mito-CoQs affect mCa^{2+} most likely via regulation of SOCE and the $m\Delta\Psi$ rather that due to CoQ_{10} itself. Mito-CoQs affect mH_2O_2 signaling preserving their antioxidant role. MitoQ, but not OH-mitoQ, negatively alters essential cellular parameters such as respiration, $m\Delta\Psi$ and Ca^{2+} signaling.

5.2. CoQ_{10} DEFICIENCY IN iPSC-DERIVED CARDIOMYOCYTES

Next, we investigated the influence of CoQ_{10} on Ca^{2+} signaling in iPSC-derived CM. For this purpose, we used COQ4-mutated iPSC-CM which contain a mutation in the COQ4 gene causing CoQ_{10} deficiency; and COQ4-corrected iPSC-CM, iPSC from the same patient in which COQ4 mutation was corrected, recovering the cellular levels of CoQ_{10}. For some of the experiments, control iPSC-CM were also used, which, although they belonged to another healthy person and cannot be considered a perfect control, could be useful in interpreting the obtained results.

First, we studied $cytCa^{2+}$ by live imaging measurements with FURA-2 AM. Calcium transients caused by contractions were detected, reflected in the form of peaks. We tried to synchronize the contractions using MyoPacer in order to quantify the changes in $cytCa^{2+}$. It was observed that the contractions in both iPSC-CM did not pace at the desired rate in all experiments. However, all cells contracted at the same time, showing small fluctuations and great irregularity in COQ4-mutated iPSC-CM (**Fig. 38**), whereas COQ4-corrected iPSC-CM presented much larger fluctuations (peaks) and more regularity between them (**Fig. 39**). As the pace failed in

most of the measurements, we could not quantify the frequency of beating, but we observed that it was much faster in COQ4-mutated iPSC-CM than in COQ4-corrected iPSC-CM (**Fig. 38 and 39**).

These fluctuations were quantified, and the basal values of cytCa^{2+} were obtained, determined as the minimum values. For this, we calculated the minimum values of each peak as shown in **Fig. 40, C**. The data showed no significant differences although there was a trend towards a higher cytCa^{2+} level in the COQ4-mutated iPSC-CM (**Fig. 40, A**). In the same way, we analysed the amplitude of the oscillations as shown in **Fig. 40, C** (red arrows - blue arrows). The quantification determined that the elevations of cytCa^{2+} were significantly higher in each contraction in the COQ4-corrected iPSC-CM compared to the mutated ones (**Fig. 40, B**). In addition, we also studied control iPSC-CM, which showed a similar behaviour to the COQ4-corrected iPSC-CMs (**Fig. 40, A-B**).

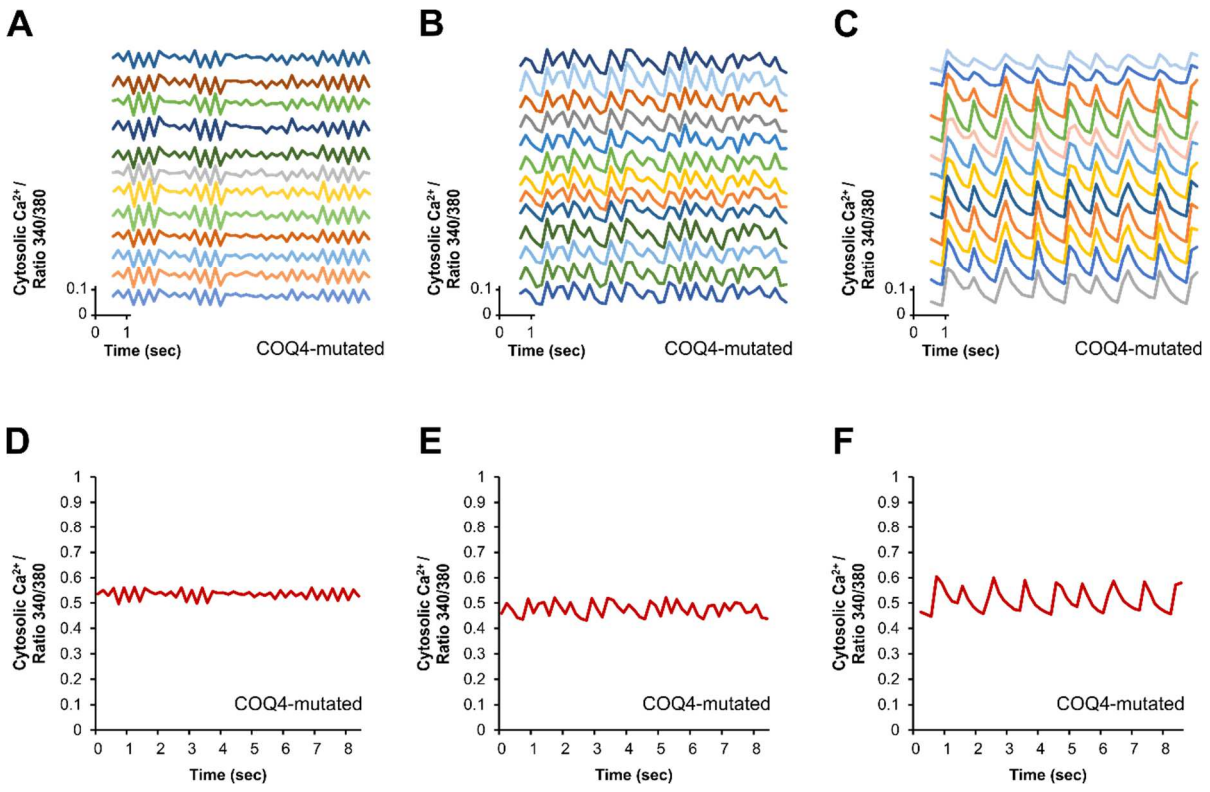

Figure 38. Cytosolic Ca^{2+} in COQ4-mutated iPSC-CM. (A-C) Three measurements as example where each graph represents the fluorescence ratio 340/380 versus time (sec) and each individual trace represents the cytCa^{2+} variations of a single cell. (D-F) The average of all the traces of the corresponding experiments (graphs above them). n values: (D) COQ4-mutated iPSC-CM = 18; (E) COQ4-mutated iPSC-CM = 26; (F) COQ4-mutated iPSC-CM = 13.

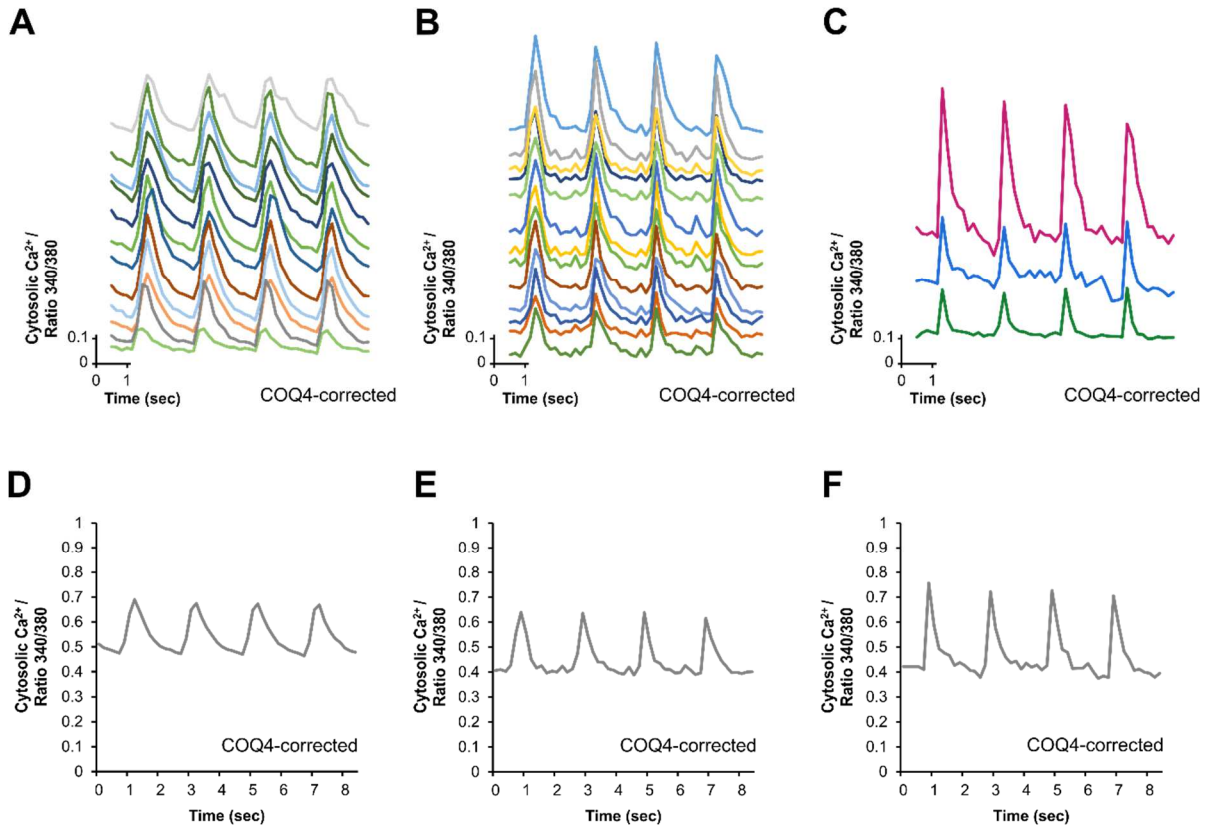

Figure 39. Cytosolic Ca^{2+} in COQ4-corrected iPSC-CM. (A-C) Three measurements as example where each graph represents the fluorescence ratio 340/380 versus time (sec) and each individual trace represents the cytCa^{2+} variations of a single cell. (D-F) The average of all the traces of the corresponding experiments (graphs above them). n values: (D) COQ4-corrected iPSC-CM = 23; (E) COQ4-corrected iPSC-CM = 24; (F) COQ4-corrected iPSC-CM = 3.

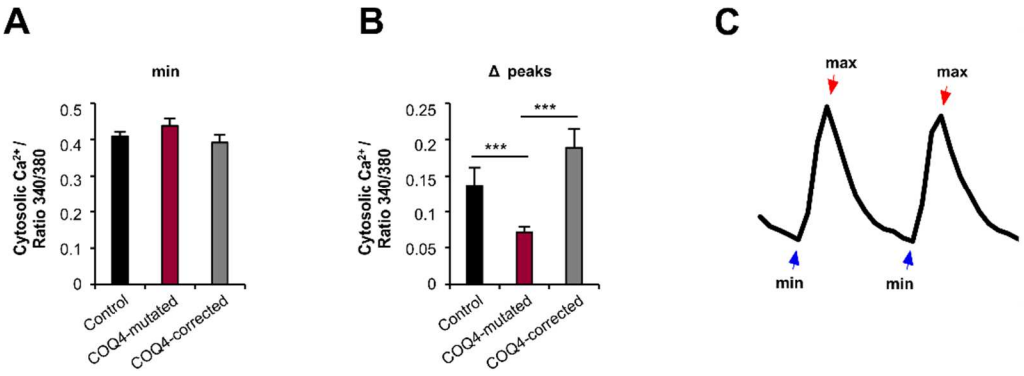

Figure 40. Cytosolic Ca^{2+} in COQ4-mutated iPSC-CM, COQ4-corrected iPSC-CM and control iPSC-CM. (A) Quantification of the minimum values. (B) Quantification of the amplitude of the oscillations (max - min). (C) Representative scheme that help to understand how the quantification was done, where the red arrows show the maximum values and the blue arrows the minimum values of the peaks. n values: control iPSC-CM = 103, from one independent experiment; COQ4-mutated iPSC = 272, from two independent experiment; COQ4-corrected iPSC-CM = 139; from three independent experiments. Data are presented in

mean ± SEM. All P-values were calculated by using Student's t-tests. *p < 0.05; **p < 0.01; ***p < 0.001.

Then, measurements of the mΔΨ by TMRM showed lower levels in COQ4-mutated iPSC-CM compared to the corrected ones (**Fig. 41, A-B**).

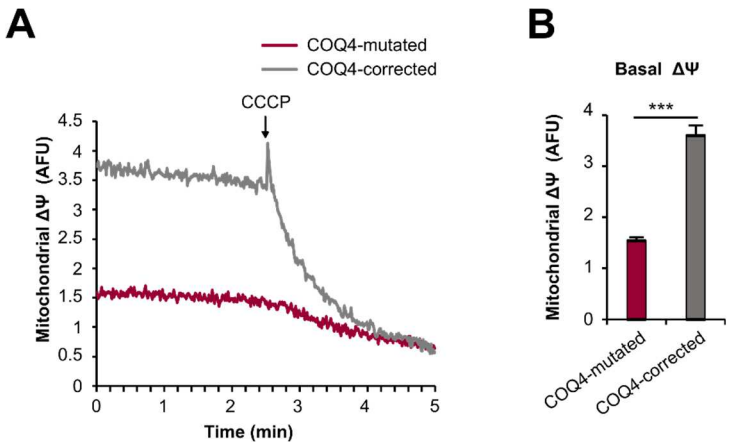

Figure 41. Mitochondrial membrane potential in COQ4-mutated and corrected iPSC-CM. (A) Arbitrary fluorescence units (Intensity mean) over time (min). First, basal values are shown and then, addition of 1 µM CCCP to TMRM loaded cells depolarize the membrane and results in fluorescence decrease. (B) Quantification of basal mitochondrial membrane potential values. n values: COQ4-mutated iPSC = 100, COQ4-corrected iPSC-CM = 53; from two independent experiments. Data are presented in mean ± SEM. All P-values were calculated by using Student's t-tests. *p < 0.05; **p < 0.01; ***p < 0.001.

Altogether, in COQ4-mutated iPSC-CM, we observe that the low values of the mΔΨ coincide with the small oscillations of cytCa^{2+}. Since there is no driving force pushing Ca^{2+} into the mitochondrial matrix, Ca^{2+} release from the SR is very small.

5.3. USE OF TARGETED QUINONES AGAINST FERROPTOSIS IN HSF

Taking into account the findings regarding the regulation of ferroptotic death through CoQ_{10} (Bersuker et al., 2019; Doll et al., 2019) and our results, we analyzed whether there is a connection between the CoQ_{10} and Ca^{2+} signaling with ferroptotic cell death.

Ferroptosis in HSF was induced using BSO and erastin. First, we performed proliferation and viability experiments with CTB and from the analysis we obtained the IC_{50} (**Fig. 42**). We choose 100 µM BSO and 1 µM for erastin as final doses to induce ferroptosis.

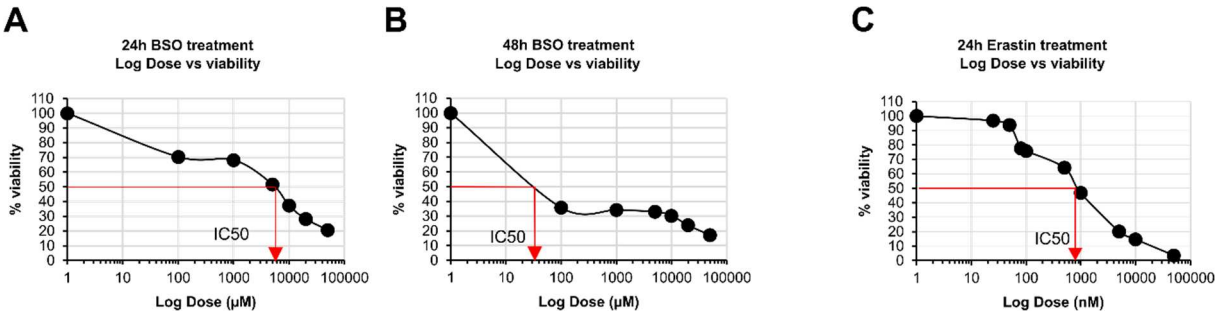

Figure 42. Ferroptosis induction in HSF. Proliferation and Viability experiments were performed with CellTiter-Blue®. HSF were cultured with BSO (100 µM, 1 mM, 5 mM, 10 mM, 20 mM, 50 mM) for 24 hours (A) and 48 hours (B) and erastin (10 nM, 25 nM, 50 nM, 80 nM, 100 nM, 500 nM, 1 µM , 5 µM, 10 µM, 50 µM) for 24 hours (C). Data are presented as the mean of at least 2 independent experiments ± SEM (n = 3 wells / each experiment).

Since ferroptosis is characterized by the accumulation of LPO products in cell membranes, we compared the effects of different CoQs depending on their location. Thus, we tested mito-CoQs (used in the previous section) and plasma membrane-targeting quinones, decylQ and its hydroxylated form, OH-decylQ. Furthermore, we also evaluated Q_1 and OH-Q_1 for some experiments.

First, we evaluated the toxicity of CoQs (mitoQ, OH-mitoQ, decylQ, OH-decylQ, Q_1, OH-Q_1). Proliferation and viability experiments measured with CTB showed that mitoQ and Q_1 at concentrations greater than 2.5 µM and OH-mitoQ at concentrations greater than 5 µM, present certain toxicity for the cells. In contrast, decylQ, OH-decylQ and OH-Q_1 did not affect cell viability at the same concentrations (**Fig. 43**).

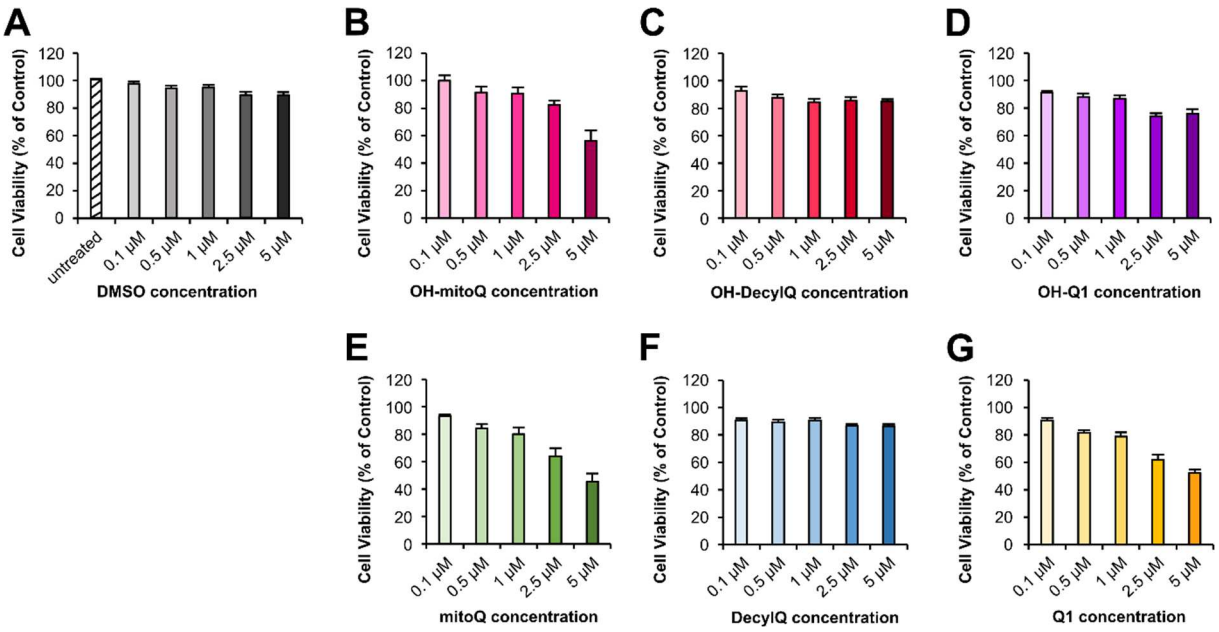

Figure 43. Toxicity of quinones assessment in HSF. Proliferation and viability measured by using the CellTiter-Blue® Cell Viability Assay of HSF in the presence of various concentrations of DMSO as a control (A), OH-mitoQ (B), OH-decylQ (C), OH-Q_1 (D), mitoQ (E), decylQ (F) and Q_1 (G). For each experiment, cells were incubated with CoQs for 72 hours before fluorescence measurement. Data were normalized with untreated HSF (Control). Data are presented as the mean of four independent experiments ± SEM (n ≥ 2 wells / each experiment).

5.3.1. Antiferroptotic effect of quinones

A possible antiferroptotic effect of the CoQs was studied. First, we incubated HSF with various concentrations of DMSO (control), to rule out a possible toxic effect of the vehicle, and 100 µM BSO or 1 µM erastin for 72 hours. As depicted in **Fig. 44**, BSO induced 60 % cell death, whereas erastin induced 95 %.

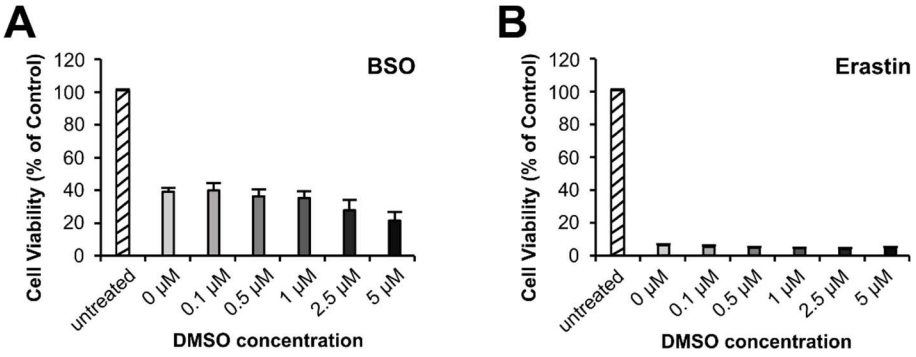

Figure 44. Ferroptosis in HSF with BSO and erastin. Proliferation and viability measured by using the CellTiter-Blue® Cell Viability Assay in HSF in the presence of 100 µM BSO (A) or 1 µM erastin (B) together with different concentrations of DMSO (as control) for 72 hours

before fluorescence measurement. Data were normalized with untreated HSF and presented as the average of at least three independent experiments ± SEM (n = 3 wells / each experiment).

Accordingly, we induced ferroptosis with 100 µM BSO (**Fig. 45**) or 1 µM erastin (**Fig. 46**) and we added the different concentrations of CoQs and OH-CoQs for 72 hours. The results showed that mito-CoQs (mitoQ and OH-mitoQ, **Fig. 45. A, D**, respectively) protected better from ferroptosis than untargeted quinones. In the experiments in which we induced ferroptosis with BSO, just 0.1 µM of mitoQ or OH-mitoQ were able to maintain 100 % survival. Using higher concentrations of these CoQs, it was seen that OH-mitoQ had a greater antiferroptotic effect. In contrast, decylQ, Q_1 and their hydroxylated forms only reached around 80 % viability even at more concentrated doses, between 0.5 µM and 1 µM (**Fig. 45. B, C, E, F**). Similarly, when we induced ferroptosis with erastin, it was observed that only mitoQ achieved a viability of 62 % with 0.1 µM (**Fig. 46. D**). However, the greatest survival (almost 80 %) was achieved with 0.5 µM OH-mitoQ (**Fig. 46. A**). Meanwhile, CoQs targeting the plasma membrane required higher doses, between 1 µM and 5 µM, to reach about 60 % viability (**Fig. 46. B, C, E, F**).

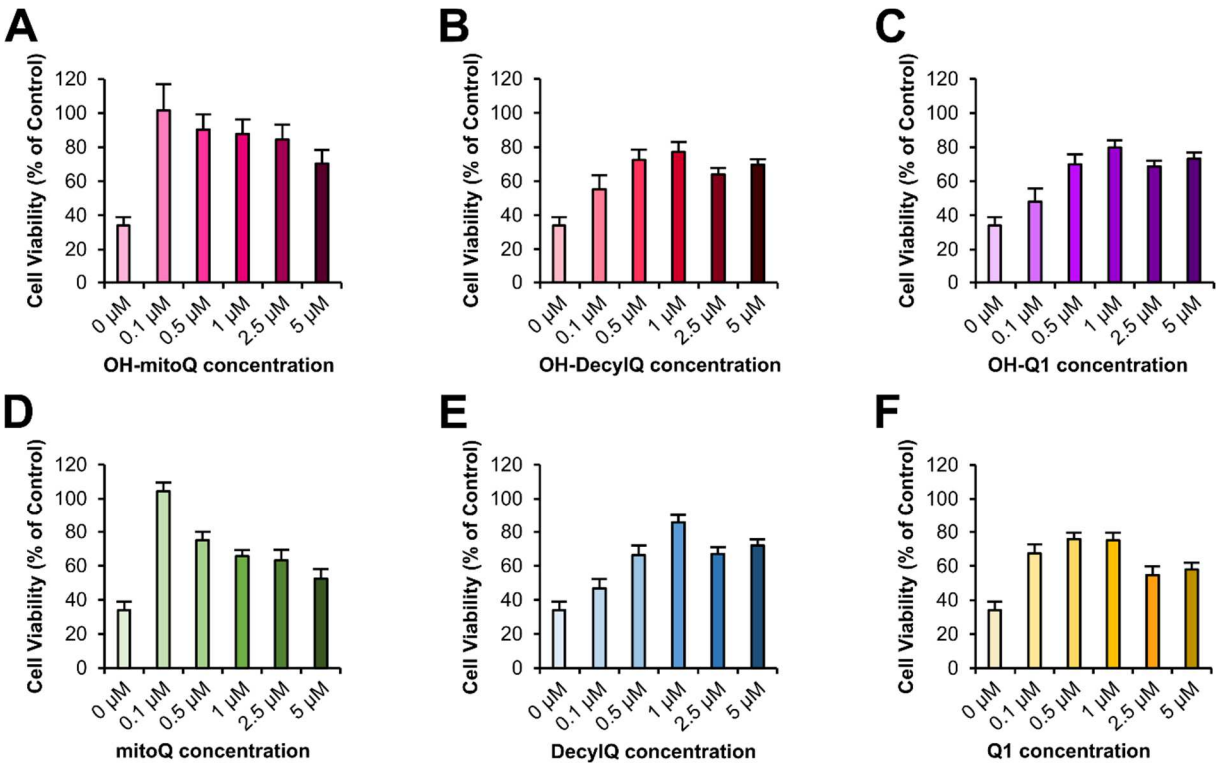

Figure 45. Induction of ferroptosis in HSF with BSO and addition of CoQs and OH-CoQs as treatment. Proliferation and viability measured by using the CellTiter-Blue® Cell Viability Assay in HSF in the presence of 100 µM BSO together with various concentrations of OH-mitoQ (A), OH-decylQ (B), OH-Q_1 (C), mitoQ (D), decylQ (E) or Q_1 (F) for 72 hours before fluorescence measurement. Data were normalized with untreated HSF (**Fig. 44, A**). Data are

presented as the mean of at least three independent experiments ± SEM (n = 3 wells / each experiment).

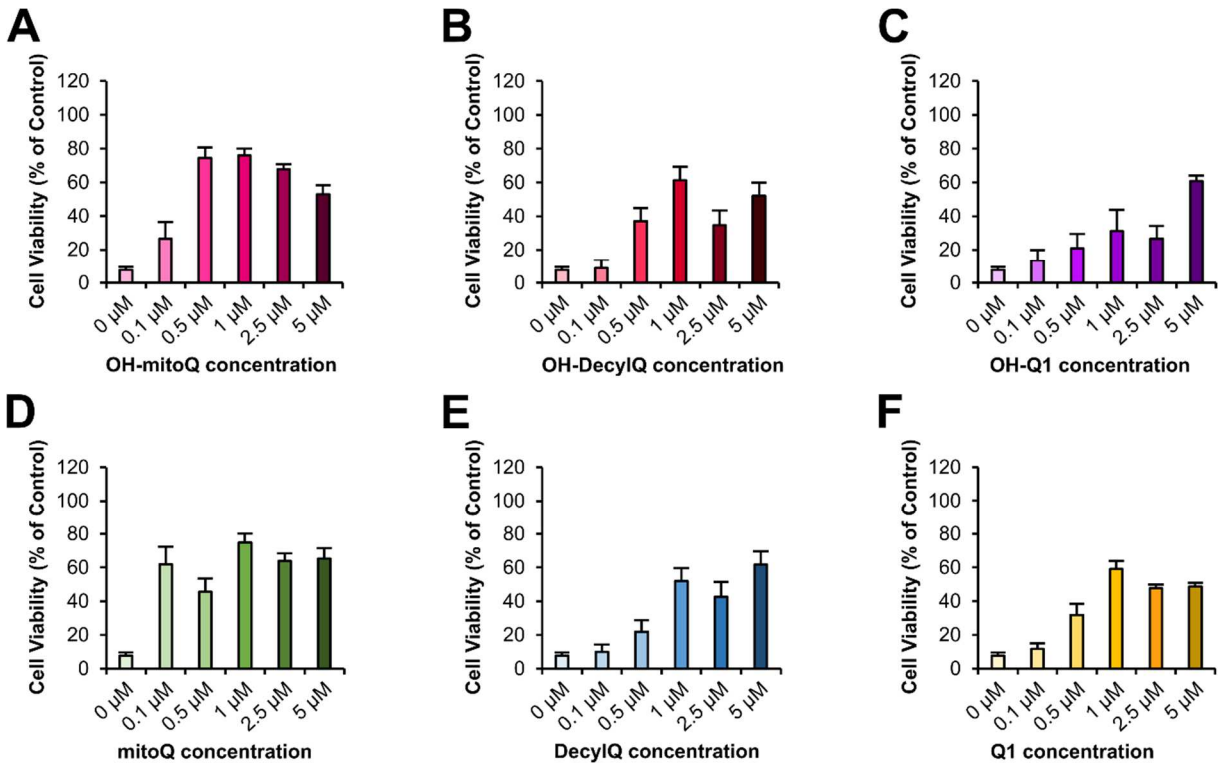

Figure 46. Induction of ferroptosis in HSF with erastin and addition of CoQs and OH-CoQs as treatment. Proliferation and viability measured by using the CellTiter-Blue® Cell Viability Assay in HSF in the presence of 1 µM erastin together with various concentrations of OH-mitoQ (A), OH-decylQ (B), OH-Q_1 (C), mitoQ (D), decylQ (E) or Q_1 (F) for 72 hours before fluorescence measurement. Data were normalized with untreated HSF (**Fig. 44, B**). Data are presented as the mean of at least three independent experiments ± SEM (n = 3 wells / each experiment).

To determine whether CoQ treatment also affects LPO, we quantified LPO with the lipophilic fluorescent dye probe BODIPY581/591 C11 after preincubating HSF with erastin and mitoQ, OH-mitoQ, decylQ, and OH-decylQ. The results indicated that all CoQs significantly decreased LPO. It should be noted that mitoQ, OH-mitoQ and decylQ stood out for their efficacy compared to OH-decylQ, which was the least effective (**Fig. 47, A-B**). To verify this result, we measured LPO in HSF pre-incubated with CoQs alone, thus evaluating the effect that CoQs cause by themselves. There were no significant differences between HSF untreated (control) and treated with mitoQ, OH-mitoQ and decylQ, whereas OH-decylQ significantly increased LPO in HSF. Although without significant differences, mitoQ and OH-mitoQ also showed a tendency to increase LPO (**Fig. 47, C**).

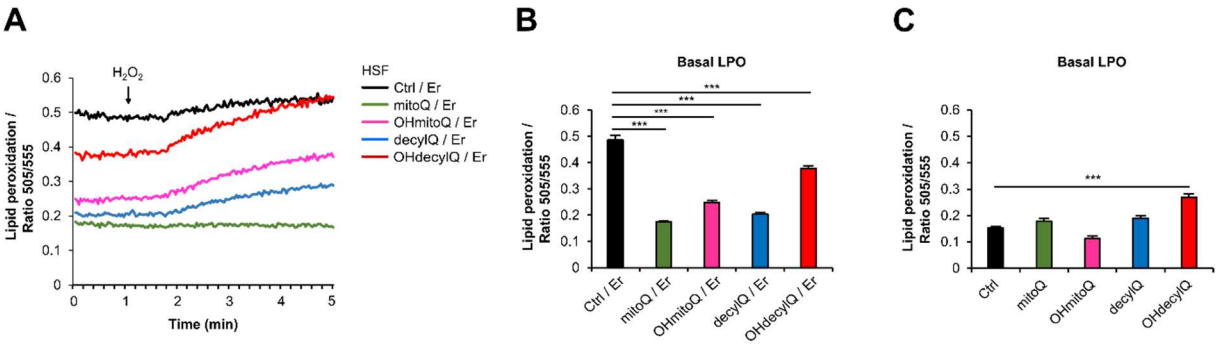

Figure 47. Protective effect of CoQs and OH-CoQs on lipid peroxidation. LPO was measured using the lipophilic fluorescent dye probe BODIPY$^{581/591}$ C11. (A, B) HSF were incubated with 5 µM erastin for 6 hours to induce ferroptosis and 0.5 µM mitoQ, OH-mitoQ, decylQ or OH-decylQ were also added in order to know the effect of quinones on LPO. 0.5 µM DMSO was added as control too. n values: ctrl/Er = 106, mitoQ/Er = 153, OH-mitoQ/Er = 138, decylQ/Er = 147, OH-decylQ/ Er = 165; from three independent experiments. (A) Data are presented as ratio-fluorescence microscopy of lipid oxidation (OX / RED ratio; background subtracted) over time (minutes). (B) The graph shows the quantification of LPO before 100 µM H_2O_2 addition. (C) HSF were incubated with 0.5 µM mitoQ, OH-mitoQ, decylQ or OH-decylQ. Also 0.5 µM DMSO was added as control. The graph presents the quantification of LPO levels. n values: ctrl = 44, mitoQ = 29, OH-mitoQ = 37, decylQ = 15, OH-decylQ = 10; from two independent experiments. Data are presented in mean ± SEM. All P-values were calculated by using Student's t-tests. *p < 0.05; **p < 0.01; ***p < 0.001.

5.3.2. Connection between Ca^{2+} signaling and ferroptosis in HSF

In order to investigate if Ca^{2+} is involved in the regulation of ferroptosis and if it is linked to quinones' functions, we performed measurements of cytCa^{2+}. Interestingly, the addition of erastin to the cell culture medium robustly reduced basal cytCa^{2+} levels, the amount of Ca^{2+} stored in the ER and SOCE (**Fig. 48**).

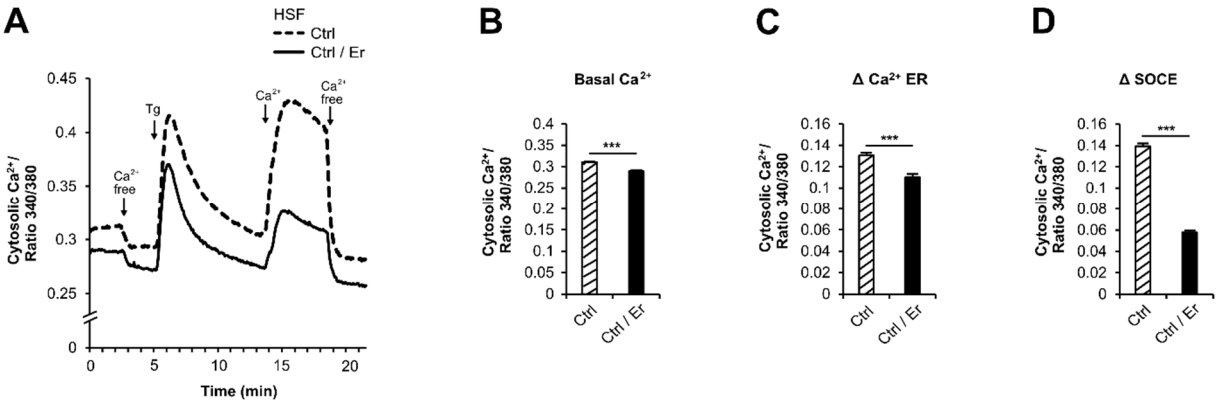

Figure 48. Cytosolic Ca^{2+} in HSF during induction of ferroptotic death. The graphs show the comparison of cytosolic Ca^{2+} between control HSF and HSF treated with 1 µM erastin for 24 h. (A) The graph represents the fluorescence ratio 340/380 over time (min). First basal cytCa^{2+} levels are shown. Next, addition of 1 µM thapsigargin to FURA - 2 AM loaded cells results in an increase of ratio 340/380, first peak, and the addition of extracellular Ca^{2+} provoke the second peak. Last, addition of free Ca^{2+} buffer decreases to minimum the ratio fluorescence. (B) Quantification of the basal Ca^{2+} levels in the cytosol. (C) Quantification of Δ values after thapsigargin stimulation (max – min), which leads to the depletion of Ca^{2+} from the ER, represents the Ca^{2+} store in the cells. (D) Δ quantification of the second peak (max – min), which is due to Ca^{2+} addition in the buffer and represents SOCE. n values: ctrl = 487, ctrl/Er = 357; from three independent experiments. Data are presented in mean ± SEM. All P-values were calculated by using Student's t-tests. *p < 0.05; **p < 0.01; ***p < 0.001.

Since we considered important to compare the role of mitochondrial-targeted and plasma-membrane-targeted quinones, before proceeding with the effect that CoQs have on ferroptosis, we assessed the effect that decylQ and OH-decylQ have on the cytCa^{2+} signaling (results of mitoQ and OH-mitoQ has been already shown (**Fig. 26**)). The results showed small changes after the addition of these CoQs compared to control HSF. OH-decylQ caused a slight decrease in basal cytCa^{2+} levels and both CoQs seemed to increase SOCE (**Fig. 49**).

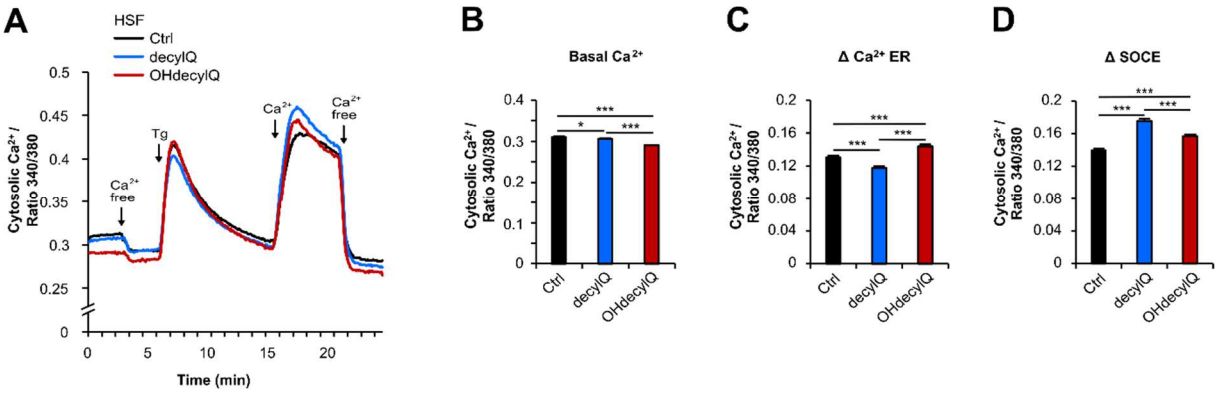

Figure 49. Cytosolic Ca^{2+} in HSF treated with decylQ and OH-decylQ. (A) The graph represents the fluorescence ratio 340/380 over time (min). First basal cytCa^{2+} levels are shown. Next, addition of 1 µM thapsigargin to FURA - 2 AM loaded cells results in an increase of ratio 340/380, first peak, and the addition of extracellular Ca^{2+} provoke the second peak. Last, addition of free Ca^{2+} buffer decreases to minimum the ratio fluorescence. (B) Quantification of the basal Ca^{2+} levels in the cytosol. (C) Quantification of Δ values after thapsigargin stimulation (max – min), which leads to the depletion of Ca^{2+} from the ER, represents the Ca^{2+} store in the cells. (D) Δ quantification of the second peak (max – min), which is due to Ca^{2+} addition in the buffer and represents SOCE. n values: ctrl = 487, decylQ = 487, OH-decylQ = 374; from three independent experiments. Data are presented in mean ± SEM. All P-values were calculated by using Student's t-tests. *p < 0.05; **p < 0.01; ***p < 0.001.

Next, we further explored the preventive effect that quinones could be providing against ferroptosis and the importance of Ca^{2+}. We pre-incubated HSF with erastin together with CoQs. For these experiments, we analyzed the effect caused by mitoQ, decylQ and their hydroxylated forms (OH-mitoQ and OH-decylQ) (**Fig. 50**). Interestingly, we again observed a pattern that distinguishes between hydroxylated and non-hydroxylated CoQs. MitoQ and decylQ showed an elevation of basal cytCa^{2+} levels, to normal values (basal cytCa^{2+}: Ctrl = 0.310, mitoQ / Er = 0.296, decylQ / Er = 0.318) while OH-mitoQ and OH-decylQ showed no changes compared to HSF incubated with erastin alone (basal cytCa^{2+} = 0.28) (**Fig. 48, B; Fig. 50, B and F**). On the other hand, mitoQ and decylQ decreased ER Ca^{2+} storage even more, while OH-mitoQ and OH-decylQ increased it reaching normal values, even exceeding them in the case of OH-decylQ (Δ Ca^{2+} ER: Ctrl = 0.130, OH-mitoQ / Er = 0.126, OH-decylQ / Er = 0.156) (**Fig. 48, C; Fig. 50, C and G**). In addition, the four CoQs increased SOCE, and the increase was more significant in the OH-CoQs, being OH-mitoQ the one that was closest to normal values (Δ SOCE: Ctrl = 0.139, Ctrl / Er = 0.057; mitoQ / Er = 0.081, decylQ / Er = 0. 085, OH-DecylQ / Er = 0. 097, OH-mitoQ / Er = 0.117) (**Fig. 48, D; Fig. 50, D and H**).

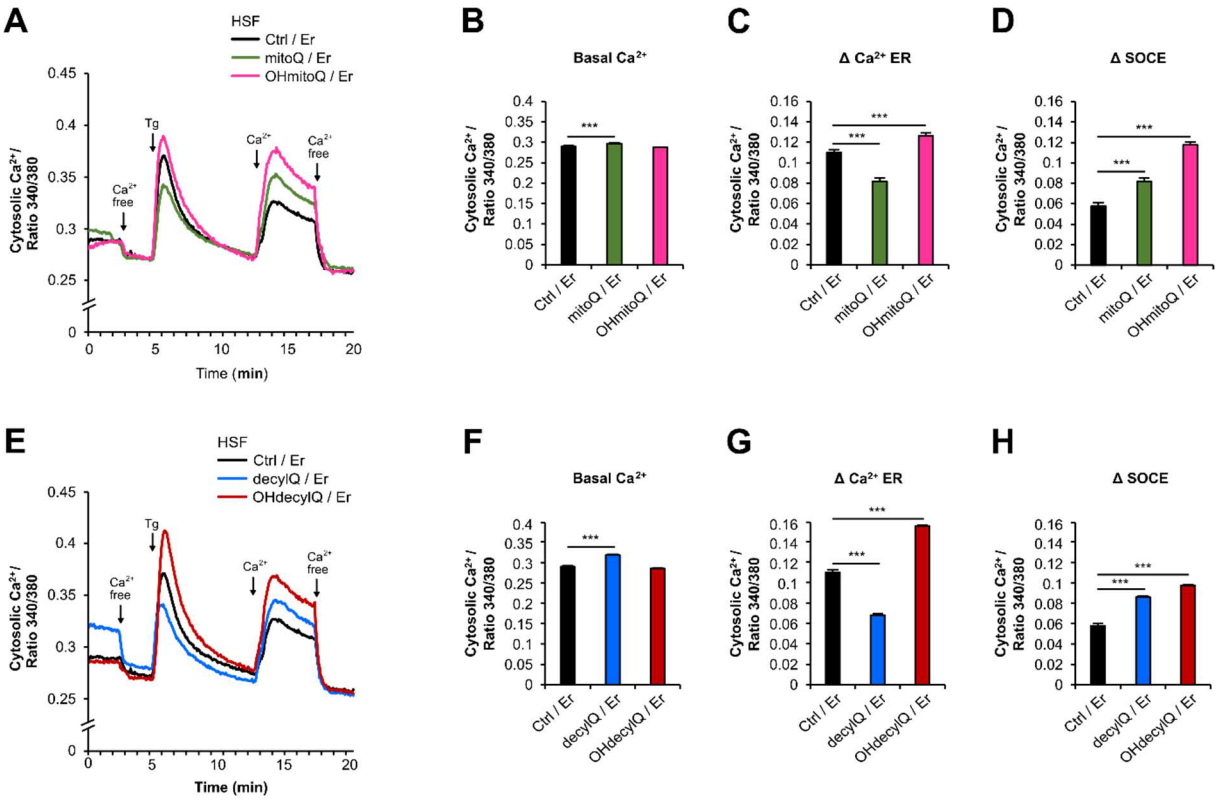

Figure 50. Cytosolic Ca^{2+} in HSF treated with CoQs and OH-CoQs during induction of ferroptotic death. The graphs show the comparison of cytosolic Ca^{2+} between HSF treated with 1 µM erastin for 24 hours and HSF treated with 1 µM erastin together with 0.5 µM of mitoQ and OH-mitoQ (A-D) or decylQ and OH-decylQ (E-H) for 24 hours. (A and E) The

graph represent the fluorescence ratio 340/380 over time (min). First basal cytCa^{2+} levels are shown. Next, addition of 1 µM thapsigargin to FURA - 2 AM loaded cells results in an increase of ratio 340/380, first peak, and the addition of extracellular Ca^{2+} provoke the second peak. Last, addition of free Ca^{2+} buffer decreases to minimum the ratio fluorescence. (B and F) Quantification of the basal Ca^{2+} levels in the cytosol. (C and G) Quantification of Δ values after thapsigargin stimulation (max – min), which leads to the depletion of Ca^{2+} from the ER, represents the Ca^{2+} store in the cells. (D and H) Δ quantification of the second peak (max – min), which is due to Ca^{2+} addition in the buffer and represents SOCE. n values: ctrl/Er = 357, mitoQ/Er = 380, OH-mitoQ/Er = 376, decylQ/Er = 259, OH-decylQ = 299 ; from three independent experiments. Data are presented in mean ± SEM. All P-values were calculated by using Student's t-tests. *p < 0.05; **p < 0.01; ***p < 0.001.

These results suggest that, mito-CoQs might be protecting against ferroptosis as effectively as untargeted CoQs, which remain in the plasma membrane, avoiding LPO. Besides, hydroxylated forms could be protecting better than native forms. In addition, the induction of ferroptosis by FINs disturbs cytCa^{2+} signaling which is almost recovered with the use of CoQs.

5.4. CoQ_{10}-DEFICIENT CELLS AND FERROPTOSIS

Finally, after observing the strong protective effect of CoQs against ferroptosis, we used cells devoid of CoQ_{10}. Based on the current knowledge, we expected that these cells will be more sensitive to FIN-induced ferroptosis.

For this purpose, we used fibroblasts lacking CoQ_{10}, labeled as P104 and P106. The cells were treated with a wide range of RSL3, BSO or erastin concentrations to induce ferroptosis. CTB assays showed that 0.5 µM of RSL3 reduced cell viability more than 50 % in control HSF, being only around 20 % of HSF able to survive with 5 µM RSL3. On the contrary, P104 and P106 were insensitive to RSL3, and even presented an increase in viability of 20 - 50 % in comparison with the untreated cells (**Fig. 51, A**). Furthermore, 100 µM BSO induced around 50 % of HSF death, while P104 and P106 again showed no changes in viability with up to 5 mM BSO. Only high concentrations of BSO (50 mM) caused reduction in viability by 50 % in the CoQ_{10} deficient fibroblasts (**Fig. 51, B**). In addition, the same experiment was performed with erastin. 1 µM erastin caused 50 % HSF death, reaching 83 % with 5 µM. As well as with the previous used FINs, P104 and P106 were much more resistant to erastin. While 10 µM erastin were needed to halve the viability in P104, P106 still exhibited almost 87 % viability at

that concentration. The addition of 50 µM erastin was needed to reduce 90 % the viability of both cells (**Fig. 51, C**).

The study continued trying to achieve such expected effect with COQ4 iPSC-CM. The idea was the same, we tried to induce ferroptotic death by the use of FINs and to prevent it with the treatment of quinones (**Fig. 52**). For this experiments, we determined cell viability by crystal violet staining comparing control iPSC-CM with COQ4 iPSC-CM. We pre-incubated the cells with RSL3 and CoQs and OH-CoQs for 216 hours. In addition, we added erastin on top the last 72 hours. At first sight, we did not observe any change in cell viability between the different conditions and neither we saw differences between iPSC-CM-control (**Fig. 52, A**) and iPSC-CM-CoQ_{10} deficient (**Fig. 52, B**), apart only from an increase in cell death probably caused by mitoQ with or without addition of erastin. However, the quantification (**Fig. 52, C**) showed that after inducing cell death with FINs around 50 % of the control iPSC-CM died, while only around 20 % death was achieved in the iPSC-CM lacking CoQ_{10}. Furthermore, OH-mito, decylQ and OH-decylQ seem to have a minimal tendency to increase cell viability after the induction of ferroptosis, but it is not statistically significant. On the other hand, mitoQ significantly decreased cell viability in both iPSC-CM.

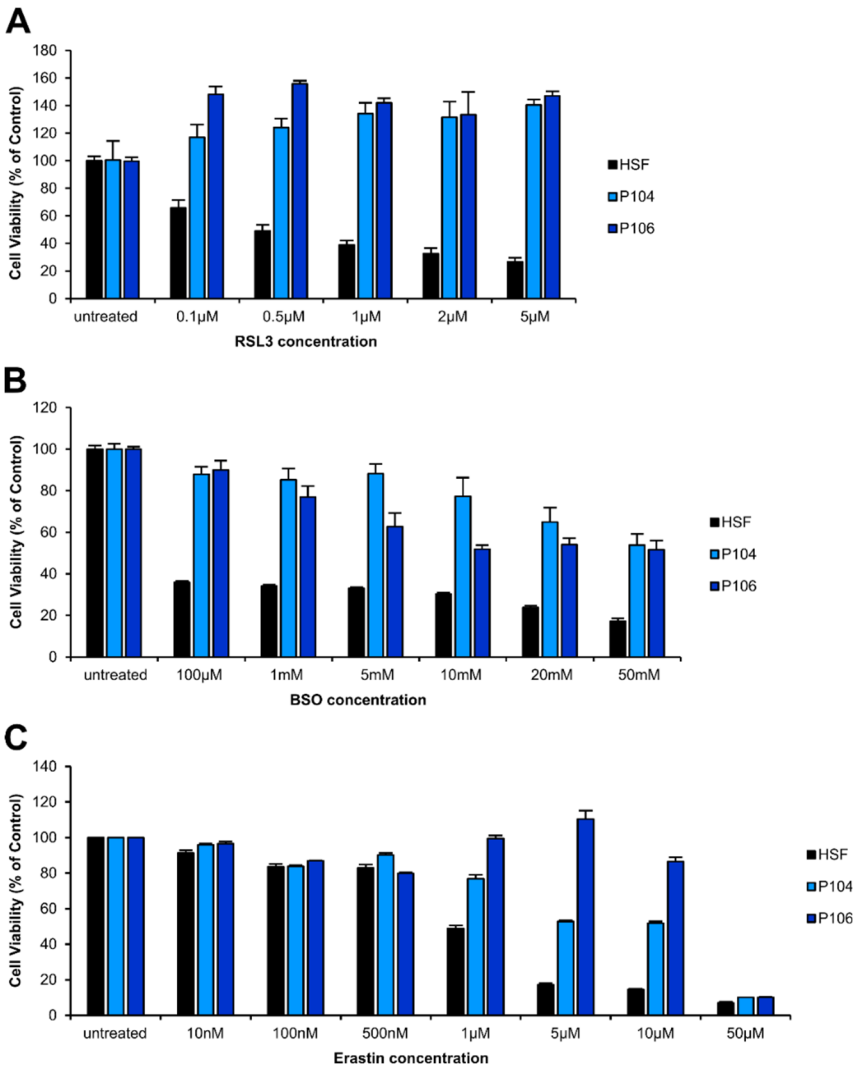

Figure 51. Induction of ferroptosis in HSF, P104 and P106 with RSL3, BSO and erastin. Proliferation and Viability measured by using the CellTiter-Blue® Cell Viability Assay in HSF, P104 and P106 in the presence of RSL3 (A), BSO (B) and erastin (C) for 24 hours before fluorescence measurement. Data were normalized with untreated HSF. Data are presented as the average of n = 3 wells ± SEM of a representative experiment, being repeated at least 2 times.

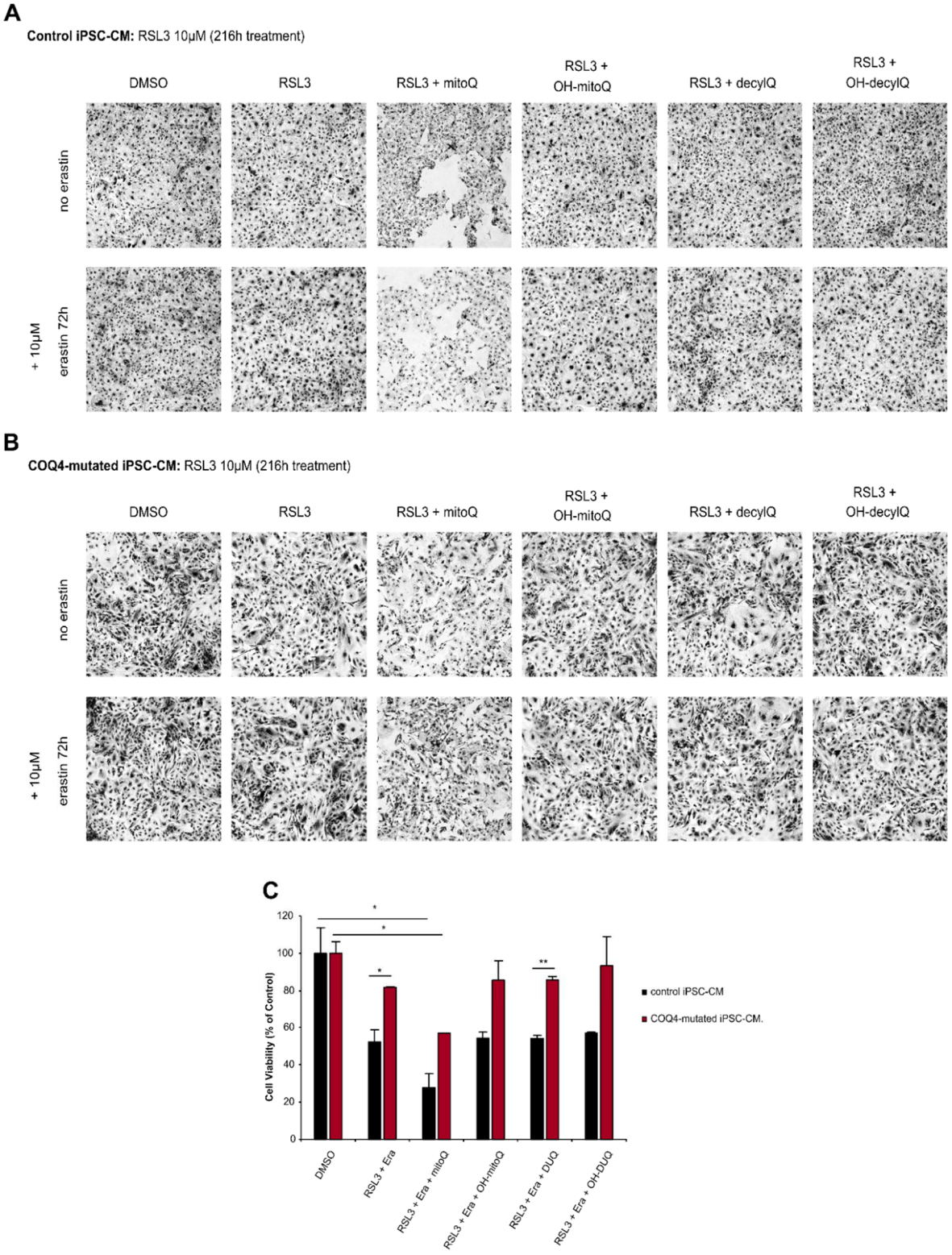

Figure 52. Induction of ferroptosis in control and COQ4-mutated iPS-CM with RSL3 ± erastin and addition of quinones as treatment. Viability measured by using PFA fixation and crystal violet staining after treating the cells with different concentrations of FINs and quinones. Images of control iPSC-CM (A) and COQ4-mutated iPSC-CM (B) after being stained with crystal violet. (C) Quantification of cell viability. Data were normalized with untreated cells. Data are presented as the mean of n = 2 wells from one independent experiments ± SEM.

Finally, as these cells were resistant to the induction of ferroptotic death, we decided to reduce the CoQ_{10} content in our control fibroblasts (HSF) by treating the cells with simvastatin. Then, we induced ferroptosis with RSL3 or erastin and perform proliferation and viability assay by using CTB. As depicted in **Fig. 53**, both addition of 0,5 µM RSL3 and 1 µM erastin in HSF, caused 50 % of cell death compared to HSF control. However, when HSF's CoQ_{10} content was reduced, RSL3 and erastin did not cause any effect on cell viability.

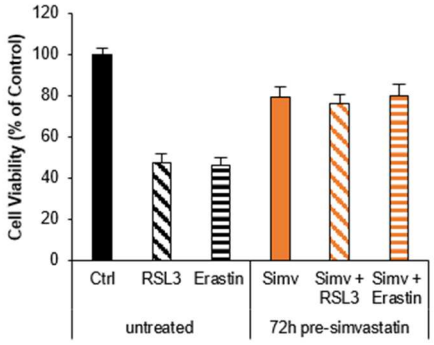

Figure 53. Induction of ferroptosis in HSF with RSL3 and erastin after CoQ_{10} reduction. Proliferation and Viability measured by using the CellTiter-Blue® Cell Viability Assay in HSF. HSF were preincubated with simvastatin (simv) for 72 hours and ferroptosis was induced by 24 hours RSL3 or erastin treatment before fluorescence measurement. Data were normalized with untreated HSF. Data are presented as the mean of at least three independent experiments ± SEM (n = 3 wells / each experiment).

These results suggested that some alternative regulatory pathway or antioxidant system may be acting to compensate CoQ_{10}'s protective properties in cells with CoQ_{10} deficiency.

6. DISCUSSION

6.1. CoQ_{10} AND Ca^{2+} SIGNALING

Mitochondria take up large amounts of Ca^{2+}, as discovered 60 years ago (Deluca & Engstrom, 1961). Since then, numerous studies have shown that mCa^{2+} signaling is essential for many cellular functions, such as proliferation, ATP synthesis and cell death (Balaban, 2009; Patron et al., 2013). Defective Ca^{2+} signaling would lead to failures in those physiological processes and, consequently, to the appearance and progression of pathologies. Several investigations have tried to identify the proteins and the mechanisms involved in Ca^{2+} transport into the mitochondria. It is known that to reach the mitochondrial matrix, Ca^{2+} has to cross the OMM and the IMM. While the OMM is permeable to Ca^{2+} through VDAC, the IMM does not have this permeability and needs specific channels and transporters. The major role in controlling mCa^{2+} uptake in the IMM is played by the MCU complex (Baughman et al., 2011; De Stefani et al., 2011; Perocchi et al., 2010). However, one of the characteristics of MCU complex is its low affinity for Ca^{2+}, being activated at concentrations around 1 μM and dependent on the electrochemical gradient of Ca^{2+} that arises from the $m\Delta\Psi$ (about -180 mV) (De Stefani et al., 2016; Kirichok et al., 2004; Petrungaro et al., 2015). Considering this and the fact that in resting conditions the $cytCa^{2+}$ concentration is $\sim 10^{-7}$ M (Bagur & Hajnoczky, 2017), an increase in Ca^{2+} localized near the mitochondria is necessary for mitochondria to take up Ca^{2+} via MCU complex. This increase in Ca^{2+} can be controlled by the organellar architecture and dynamics or generated by a stimulus or signaling mechanisms, such as SOCE (Parekh, 2008). However, we suggest that there must be some component in the IMM that mobilizes Ca^{2+} from the cytosol to the mitochondria in resting conditions.

In addition to MCU complex, other transporters have been proposed as regulators of mCa^{2+} signals. LETM1 (leucine zipper-EF-hand-containing transmembrane protein 1) has been suggested as a Ca^{2+}/H^{+} exchanger and could potentially act both on influx and efflux depending on whether the mCa^{2+} concentration is low or high, respectively (Jiang et al., 2009). NCX (mitochondrial Na^{+} -Ca^{2+} exchanger) has also been proposed as a candidate to regulate mCa^{2+}. Initially, it was suggested that it participated in the export of Ca^{2+} from the mitochondrial matrix ($3Na^{+}/Ca^{2+}$) (Palty et al., 2010). However, it has recently been shown that NCX can also act in the opposite direction by transporting Ca^{2+} to the matrix (Samanta et al., 2018). In addition, mitochondrial uncoupling proteins 2 and 3 (UCPs 2-3) were also described to participate in the mCa^{2+} uptake (Graier et al., 2008). Although, there is debate over the function of these

transporters (Brookes et al., 2008) and more research is necessary to fully understand their roles in mCa^{2+} regulation.

Given the role of CoQ_{10} as a major antioxidant and transporter of e^- and H^+ in the mETC, it was hypothesized in the past that if CoQ_{10} is capable of transporting H^+, it could also transport other cations such as Ca^{2+}. Thus, in this study, we manipulated the content of CoQ_{10} in HSF. We found that the basal levels of mCa^{2+} and the uptake of Ca^{2+} by the mitochondria were higher when CoQ_{10} was decreased (**Fig. 20**). This result suggests that CoQ_{10} may participate in the efflux of Ca^{2+} ions from the mitochondrial matrix, instead of in Ca^{2+} uptake.

However, it is unclear if Ca^{2+} transport is a real function of CoQ_{10}. Otherwise, it could be that, due to alterations in CoQ_{10} content, other parameters are affected, being responsible for these changes in Ca^{2+} signaling. For example, an increase in cell proliferation and viability, would cause a greater energy demand; or an increase in the levels of $cytCa^{2+}$, would cause the activation of the MCU complex allowing the entry of Ca^{2+}. We tested both parameters and showed that neither of them affected mCa^{2+} signaling (**Fig. 21, 22**). Furthermore, changes in $m\Delta\Psi$ could also explain such increase in mCa^{2+}, since the entry of Ca^{2+} through the MCU complex is dependent on the electrochemical gradient that exists through the IMM ($m\Delta\Psi$) (Jacobson & Duchen, 2004; McKenzie et al., 2017). Interestingly, we detected an increase in $m\Delta\Psi$ after the decrease in CoQ_{10}, which was reversed by restoring the content of CoQ_{10} in the cell (**Fig. 23. A, B**). On the other hand, our observations also indicate that the increase in mCa^{2+} could also be due to changes in the MCU complex. Gene expression analysis showed a significant decrease in MCUb, a blocking part of the complex (Lambert et al., 2019), which would positively affect the entry of Ca^{2+} (**Fig. 23, D**). However, the cells treated with 4NB + 4HB, displayed a decrease in MCUb expression and, on the contrary, mCa^{2+} levels were not altered.

6.1.1. CoQ supplementation

With the idea of correcting deficiencies in CoQ_{10} and the drawbacks that they entail, numerous studies have suggested beneficial effects of CoQ_{10} supplementation in several diseases. For instance, in cardiomyopathy, patients with moderate to severe heart failure treated with CoQ_{10} showed that CoQ_{10} treatment was safe, improved symptoms and reduced major adverse cardiovascular events (Mortensen et al., 2014). Furthermore, Mohseni et al. found that CoQ_{10}

supplementation was able to improve blood pressure and lower cholesterol in patients with hyperlipidemia and myocardial infarction (Mohseni et al., 2014). In addition to cardiac diseases, there are studies showing that supplementation with CoQ_{10} has a beneficial effect on hypertension (Gonzalez-Guardia et al., 2015), diabetic kidney diseases (Xiao et al., 2017) and multiple sclerosis (Mao et al., 2013). Moreover, CoQ_{10} administration significantly reduced triglyceride concentrations in patients with metabolic disease (Sharifi et al., 2018), improved chronic obstructive pulmonary disease (Chen et al., 2019) and neurodegenerative diseases (Muthukumaran et al., 2018), and it has even been described as a potential treatment for COVID-19 (Ouyang & Gong, 2020). More focused on the mitochondria, since it contains large amounts of CoQ_{10}, the mitochondrial-targeting CoQ_{10} analogue, mitoQ, has long been considered as a potential drug. For instance, a study of cardiac fibrosis in mice showed that mitoQ improves cardiac hypertrophy, fibrosis and LV dysfunction in pressure-overloaded hearts by inhibiting the interaction between TGF-β1 and mitochondrial redox signalling (Goh et al., 2019). It should be noted that most studies performed with CoQ_{10} supplementation focused on its function as an antioxidant. It is even stated, literally, that the main benefit of CoQ_{10} supplementation comes from its ability to reduce oxidative stress, which is the most important and relevant function (Gutierrez-Mariscal et al., 2020). While it seems clear that mitoQ experimentally reduces ROS levels in mitochondria and prevents oxidative stress, far less attention has been paid to potential side effects. Considering that mitoQ accumulates in mitochondria in very high concentrations, the possibility that it may regulate mitochondrial function at other levels should not be ignored. In particular, mitoQ could interfere with Ca^{2+} signaling, since we show that CoQ_{10} can modulate mCa^{2+}.

In previous studies, our research group has extensively analyzed the physicochemical and physiological properties of CoQ_1 and CoQ_{10}. Interestingly, a new group of specifically hydroxylated quinones (OH-CoQs) through radical mechanisms at high pH or in the presence of cytochrome P450 was identified. OH-CoQs were quite stable and acted as potent ROS scavengers. Furthermore, they were able to efficiently and selectively bind alkaline earth metal cations, particularly Ca^{2+}, and transport them through an artificial bio-membrane. It is worth noting that the chemical approach to produce hydroxylated derivatives used in the studies could, in principle, be replaced by the action of monooxygenases or other hydroxylating enzymes in organisms (Bogeski, Gulaboski, et al., 2011; Gulaboski et al., 2013). Thus, these results suggested that OH-CoQ_{10} could be a good candidate for regulating Ca^{2+} in mitochondria when $cytCa^{2+}$ levels are low.

Hence, with these findings and aiming to elucidate the mechanism of action behind this increase in mCa^{2+}, when decreasing CoQ_{10} content, we treated HSF with mitoQ and its hydroxylated form, OH-mitoQ. Addition of mitoQ significantly reduced mCa^{2+} levels fitting with the previous results, while OH-mitoQ increased them (**Fig. 24**). Further experiments showed that mitoQ depolarized the membrane (**Fig. 27**), reduced Ca^{2+} signaling also at cytosolic levels (**Fig. 26**) and reduced mitochondrial respiration (**Fig. 29**). By contrast, OH-mitoQ was shown to be a good antioxidant that does not alter mitochondrial metabolism. Furthermore, the gene expression levels of components of the MCU complex did not show an increase in MCUb (**Fig. 28, A**). Therefore, it was not possible to explain this effect by changes at the genetic level. On the other hand, at the protein level (**Fig. 28, B-F**), MCUb is highly expressed when we pre-incubate with mitoQ, suggesting that it may affect mCa^{2+} to some extent. It should also be noted that pre-incubation with OH-mitoQ also produces an increase in MCUb protein, while mCa^{2+} is not inhibited. These results show that modifications in gene or protein expression of MCU complex are not likely to be the cause of mCa^{2+} changes, but they suggest that mitoQ affects mCa^{2+} most likely via regulation of the $m\Delta\Psi$ and SOCE.

Supporting our results, previous studies also found that mitoQ decreased the $m\Delta\Psi$ in bovine aortic endothelial cells (BAECs) at concentrations higher than 1 μM, in this case, showing no toxicity when measuring cell viability (Fink et al., 2009). Furthermore, Gottwald et al. have shown, using live imaging and both *in vitro* and *in vivo* models, that mitoQ (500 nmol/L) caused inflammation and acute mitochondrial depolarization in Kidney proximal tubules (Gottwald et al., 2018). Another study has reported that mitoQ could actually increase ROS production in some cancer cells, and this was associated with a decrease in $m\Delta\Psi$ and mtDNA integrity (Pokrzywinski et al., 2016). Moreover, mitoQ has also been found to induce autophagy in liver cells (Lyamzaev et al., 2018). Besides, it has been described as inappropriate for the therapy of acute pancreatitis. In this disease, bile acids depolarize the mitochondrial membrane and *in vitro* studies with mitoQ showed that mitoQ not only did not reduce such depolarization, but it rather enhanced it. In *in vivo* models, mitoQ treatment was also not protective (Huang et al., 2015).

In addition, and supporting our data, it was published that mito-CoQs enhanced ECAR under basal respiratory conditions (Fink et al., 2012), suggesting that these compounds enhance glycolysis (**Fig. 29, E, F**). This increase in glycolysis produced by mitoQ was described to be dose-dependent. Additionally, mitoQ has been reported to suppress fatty acid oxidation (Fink et al., 2012).

Therefore, our results and, as mentioned, other studies show that mitoQ treatment is toxic to some cells, at least in the concentration used due to the devastating side effects.

6.1.2. Toxicity of mitoQ

Studies showed that the toxic effect of mitoQ may depend on time and dose. Hence, one study indicated a marked reduction in oxidative respiration at mitoQ concentrations above 150 nM. It is pointed out that the use of mitoQ for therapeutic purposes must consider the bioenergetic action and the doses must be low enough to avoid a critical limitation of the generation of cellular ATP (Fink et al., 2012). Of note is that most of the cellular studies demonstrating the benefits of mitoQ involved concentrations in the upper range or above what they examined herein. For example, a study showed that concentrations of 0.5 and 1 µM of mitoQ significantly reduced endogenous DNA damage, while lower concentrations had no impact. The results of this investigation suggest that mitoQ may have anti-immunosenescent potential on human peripheral mononuclear cells (Marthandan et al., 2011). However, our data reflected that at a concentration of 0.1 µM, mitoQ caused a decrease in the mΔΨ (**Fig. 27, G**) if we compare it with the vehicle (**Fig. 27, E**). Although it would be interesting to study how lower concentrations of mitoQ affect other physiological parameters, the change in the mΔΨ already indicates that there is a change in mitochondrial metabolism.On the other hand, other studies showed that the toxic effect of mitoQ could be caused by the TPP+ cation. Reily et al. compared effects of antioxidants directed to the mitochondria, including mitoQ, on the cellular bioenergetics of mesangial cells, with the lipophilic cation TPP+, which lacks the antioxidant functional group and is responsible for directing the molecule to the mitochondria. They demonstrated that the TPP+ can alter mitochondrial function at concentrations frequently observed in cell cultures (0.1 - 1 µM), independently of the antioxidant functional groups (Reily et al., 2013). Another study proved that depolarization mΔΨ in kidney proximal tubules is due to increased permeability of IMM, rather than antioxidant activity, since this effect is repeated by TPP+, but not by Elamipretide (SS-31), another mitochondrial target antioxidant lacking in TPP+ (Gottwald et al., 2018). On the contrary, Fink et al., showed that the effects of mitoQ on IMM uncoupling are not caused by the TPP+ cation moiety, because the cation itself did not alter the bioenergetic profile (Fink et al., 2012). Our data is supported by these last results since both mitoQ and OH-mitoQ present the TPP+ cation, and while mitoQ causes alterations in mitochondrial bioenergetics, OH-mitoQ, at the same concentration, does not (**Fig. 29**). It is

likely that the effects of TPP+ compounds also depend on the cell type, since the bioenergetics of cells show a variety of responses depending on the number of mitochondria and their regulation (Dranka et al., 2011).

In conclusion, there is a pressing need to understand better the mechanism of action of mitoQ on mitochondrial function before treating patient with it. On the contrary, we demostrate OH-mitoQ as a good potential candidate.

6.2. CoQ_{10} AND REDOX SIGNALING

Mitochondria are thought to be the main sources of ROS in most cell types. $O_2^{-\bullet}$ is produced in complexes I and II of the ETC, which is quickly converted into H_2O_2, a much more stable ROS, by SOD. $O_2^{-\bullet}$ and H_2O_2 are no longer considered simply as cytotoxic byproducts of respiration (Zorov et al., 2014). On the contrary, ROS are well established as important second messengers and signaling molecules that participate in a multitude of physiological processes (D'Autreaux & Toledano, 2007). Besides, accumulating evidence suggests an important interaction between Ca^{2+} and redox signalling (Bogeski, Kappl, et al., 2011; J et al., 2014; Jacobson & Duchen, 2002; Saul et al., 2016). Accordingly, high mCa^{2+} concentration is associated with increased energy production, resulting in greater flux through the ETC and subsequently higher levels of generated H_2O_2 (Diebold & Chandel, 2016; Ermakova et al., 2014; Murphy, 2009). H_2O_2 acts as a regulator of cell signaling pathways through the oxidation of thiol groups of proteins, affecting their location, interaction and enzymatic activities. However, when H_2O_2 levels exceed a certain threshold, indiscriminate oxidation is triggered, which can even culminate in cell death (Pak et al., 2020).

In several studies have been shown that mCa^{2+} and redox signalling are altered and significantly contribute to disease progression and pathogenesis (Lemasters et al., 2009; Nakayama et al., 2007). It was shown the relevance of Ca^{2+} on the mitochondrial permeability transition (mPTP), a relevant process in both necrosis and apoptosis cell death (Lemasters et al., 2009). Therefore, we wonder if mCa^{2+} and redox signalling also was also involved in other types of programmed cell deaths.

Oxytosis was first described more than 30 years ago in nerve cells as a non-excitotoxic pathway for glutamate-induced cell death (Miyamoto et al., 1989; Murphy et al., 1988; Murphy et al., 1990; Tan et al., 2001). The main characteristics of oxytosis are GSH depletion, lipoxygenase

activation, accumulation of ROS, and increased Ca^{2+} influx (Lewerenz et al., 2018). In 2012, a pathway with similar characteristics as oxytosis was identified in transformed fibroblasts and it was called ferroptosis (Dixon et al., 2012). All the evidences indicate that these are the same cell death pathways. Several studies have shown an increase in cytCa^{2+} during the last stage of ferroptotic death. (Li et al., 1997; Tan et al., 1998). Furthermore, several compounds that decrease Ca^{2+} influx, such as CoCl2 (Tan et al., 1998) and apomorphine (Ishige et al., 2001) have been described as inhibitors of ferroptotic cell death induced by erastin and RSL3, further supporting a role for late-stage Ca^{2+} influx in oxytosis/ferroptosis. Moreover, Nagase et al. recently showed that erastin induced Ca^{2+} influx in HT22 cells (Nagase et al., 2020). An additional study showed that the abolition of Orai1 and Orai3 also protects against RSL3-induced ferroptosis (Goldberg et al., 2020), thus providing more evidence that the Ca^{2+} entry is a characteristic of this cell death. Another group also detected an increase in cytCa^{2+} in the last stage of ferroptosis. But in this case, it was associated with nanopores in the MP instead of with SOCE (Pedrera et al., 2021). Noteworthy, all studies were conducted in mouse cell lines.

In this study, we induced ferroptosis with BSO and erastin in HSF and could record increase in cell death (**Fig. 44**) and increase in LPO (**Fig. 47**). However, contrary to what has been described, the induction of ferrotosis with erastin caused a significant decrease in the basal levels of cytCa^{2+}, as well as Ca^{2+} store content in the ER and SOCE (**Fig. 48**).

This discrepancy may be due to the different phases of the ferroptotic process. In the early phases of ferroptosis there could be a decrease in cytCa^{2+}, while in the final phase there could be an increase. We pre-incubated HSF with 1 µM erastin for 24 hours and perhaps this was not enough time to show that increase in cytCa^{2+} levels before cell death. But when checking the methods that Nagase et al., 2020 used for their study, they use lower concentrations during the same time (0.2 µM or 0.5 µM for 24 h); thus dismantling this possible explanation. However, ferroptosis is a specie- and cell-type process, therefore, although this effect on Ca^{2+} levels appears to be consistent in mouse models, it might not be happening the same in humans.

6.2.1. CoQs against ferroptosis

In 2004, Dhanasekaran et al. published that pre-treatment of BAECs with the mitochondrial antioxidants, mitoQ (1 µm) but not with the untargeted antioxidants (vitamin E) inhibited LPO

and protein oxidation (Dhanasekaran et al., 2004). It was reported that mitoQ reduced the cellular iron concentration, as it is now known that it also functions as an iron chelator (Bentinger et al., 2007; Bentinger et al., 2010).

Our results showed that mitoQ (0.5 μM) reduced LPO (**Fig. 47**) and reduced mH_2O_2 levels (**Fig. 30, 36**), but it did depolarize the mitochondrial membrane (**Fig. 27, 34**).

On the other hand, Friedmann Angeli et al. demonstrated that the mitochondria-targeted antioxidant mitoQ is much less efficient in protecting cells against ferroptotic cell death caused by the removal of Gpx4 (KO) or the use of FINs (erastin, RSL3 or BSO), compared to the membrane-targeted antioxidant decylQ. The study was done in mouse embryonic fibroblast (Pfa1 cells), and specifically, they determined that 100 times higher concentrations of mitoQ were needed. They state that not only the extramitochondrial compartments but also the mitochondria were involved in the increase in LPO caused by Gpx4 depletion. However, rescue with mitochondria-targeted antioxidants was much less efficient than with non-targeted ones (Friedmann Angeli et al., 2014).

Trying to simulate these results, in addition to verifying the effect that OH-CoQs, targeted to mitochondria or untargeted has on ferroptosis, we added quinones to HSF in which ferroptotic death was induced by BSO or erastin. Contrary to what has been described, mito-CoQs protected the cells from ferroptosis to a similar extend as untargeted CoQs that remain in the plasma membrane (**Fig. 45, 46**). Furthermore, although there was not a big difference, there was a trend that indicated that hydroxylated forms protect better. In addition, LPO was reduced following treatment with all quinones.

To further study the involvement of Ca^{2+} in the regulation of ferroptosis and the contribution of CoQs in its regulation, we induced ferroptosis with erastin and tested $cytCa^{2+}$ levels after a treatment with CoQs. Surprisingly, the levels of $cytCa^{2+}$ were almost restored, suggesting the participation of Ca^{2+} in ferroptotic cell death (**Fig. 48, 50**).

The protecting effects of mitochondrially targeted quinones may be because not all mitoQ and OH-mitoQ molecules reach the mitochondria. Due to their lipophilicity, some proportion of these molecules could remain in the plasma membrane. It may also be that the effect is different depending on the species. Although most studies are investigating fibroblasts, mouse fibroblasts and human fibroblasts can behave completely different. Nevertheless, additional studies are needed to understand the role of coenzyme Q as well as mitochondria in ferroptosis.

6.2.2. Resistance of CoQ_{10}-deficiency cells to ferroptosis

In order to understand the clinical relevance of our findings, we evaluated the potential therapeutic use of quinones targeting mitochondria, especially their hydroxylated forms. In primary HSF deficient in CoQ_{10} and also in iPSC differentiated cardiomyocytes from patients deficient in CoQ_{10}, we induced ferroptosis with erastin, BSO or RSL3. By utilizing this approach, it was possible to block the glutathione-dependent pathway at different points: by inhibiting the cystine/glutamate antiporter, the GCL enzyme or GPX4, respectively. Considering the two known pathways that protect against ferroptosis: glutathione-dependent pathway and FSP1 - CoQ_{10} - NAD(P)H pathway, we assumed that these cells, in the absence of CoQ-dependent protection, would be much more sensitive to FIN-induced ferroptosis. Unexpectedly, the concentration of FINs needed to induce ferroptotic cell death in HSF and iPSC-derived cardiomyocytes was significantly higher in the CoQ_{10}-defficient cells (**Fig. 51**). While 100 µM BSO was enough to lower the cell population to half, 50 mM BSO was required to achieve just that 50 % cell death in CoQ_{10}-deficient fibroblasts. Likewise, 1 µM erastin in healthy HSF caused a reduction in viability between 80 - 90 %, while not even 10 µM erastin affected the viability of CoQ_{10}-deficient fibroblasts. The similar effect could be observed upon treatment with RSL3, 0.5 µM caused the death of more than 50 % of the healthy HSF, while in CoQ_{10} deficient fibroblasts, the viability was intact or even increased with 5 µM. In the case of cardiomyocytes (**Fig. 52**), much higher concentrations of the drugs (RSL3 and erastin) were needed to induce ferroptosis. Nevertheless, the effect was similar, as we observed that after treatment with FINs, around 50 % cell death was achieved in the control cardiomyocytes, while only around 25 % of cardiomyocytes lacking CoQ_{10} were not viable following treatment with the same concentration of FINs. These results suggested that some other alternative pathway or antioxidant system may be activated or upregulated in cells with CoQ_{10} deficiency.

It had been described that direct inhibition of GCL (by BSO) leads to upregulation of an alternative antioxidant pathway that may also slow down ferroptosis. For example, high levels of SLC7A11-mediated import of Cystine, in conjunction with the thioredoxin system, may

replace the GSH-dependent metabolic pathway in some cells both *in vitro* and *in vivo* (Cao & Dixon, 2016; Harris et al., 2015; Mandal et al., 2010).

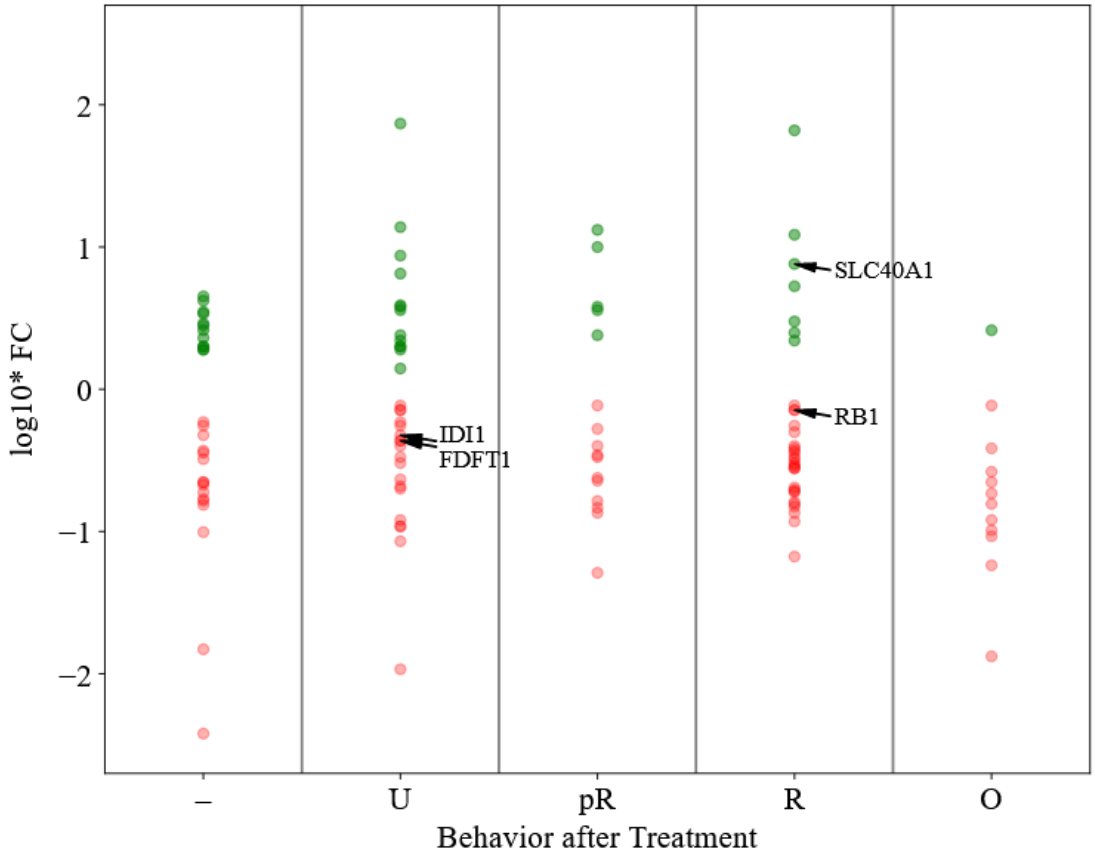

Figure 54. Significant gene hits of CoQ deficency fibroblast patients versus control. Corresponding full change (FC) values from the comparative analysis ran with Affymetrix GeneChip Human Genome U133 Plus 2.0 Array by Navas at al. are transformed via sign(x)*log10(|x|). Genes are categorized by the behavior after the treatment: non-affacted (−); uneffected (U); partially recovered (pR); complete recovered (R); opposite regulation (O). Graph done with the help of Christian Ickes.

Fernández-Ayala et al. compared the transcriptome of control fibroblasts with CoQ_{10}-deficient fibroblasts and CoQ_{10}-treated CoQ_{10}-deficient fibroblasts (Fernandez-Ayala et al., 2013). Up-regulation of TRX or SLC7A11 was not observed, although this could be due to the small number of samples that have been obtained for analysis. However, other ferroptosis relevant genes RB1, FDFT1 and IDI1 were significantly down-regulated. RB1 encodes a protein, which is a negative regulator of the cell cycle; and both FDFT1 and IDI1 genes encode proteins involved in the biosynthesis pathway of CoQ_{10}. Furthermore, SLC40A1 was up-regulated in

fibroblasts deficient in CoQ_{10} and its expression was fully recovered after CoQ treatment (**Fig. 54**). SLC40A1 encodes the only iron export protein ferroportin (FPN) in the cell membrane, whose function is to maintain iron homeostasis (Lakhal-Littleton et al., 2015). Recent studies show that the down regulation of SLC40A1 causes an increase in the amount of cellular iron which can cause an acceleration of ferroptosis (Deng et al., 2021; Geng et al., 2018; Hao et al., 2021). Thus, the upregulation of CLS40A1 provides a possible explanation for our results, although most likely, CLS40A1 does not participate alone and the rest of the genes that appear up-or down-regulated should not be ignored and their contribution to ferroptosis warrants further investigation. With a higher expression of SLC40A1, the iron molecules that trigger ferroptosis are exported, and consequently the cells will escape this type of cell death.

These findings reveal new ferroptosis-relevant regulatory mechanisms in cells and patients with CoQ_{10} deficiency. Understanding these mechanisms might be important in order to determine the clinical and therapeutic relevance of our findings.

7. CONCLUSSIONS

In conclusion, our results suggest that CoQ_{10} modulates Ca^{2+} signalling, which is crucial for essential cellular parameters, most likely via regulation of SOCE and the $m\Delta\Psi$.

CoQ_{10} analogues targeted to mitochondria, including mitoQ, have been shown to be good antioxidants, with beneficial effects in combating the development of several diseases. However, our results, supported by other studies, showed that mitoQ disturbed viability, respiration, $m\Delta\Psi$ and Ca^{2+} signalling in some cells. Therefore, this study showed mitoQ as a toxic compound, indicating that the therapeutic use of this quinone should be stopped.

On the other hand, we found that the antioxidant effects of OH-mitoQ (the hydroxylated form of mitoQ) were comparable to those of mitoQ, and both were effective inhibitors of ferroptosis, similarly as untargeted CoQs. In addition, OH-mitoQ did not cause cytotoxic effect and did not change cellular metabolism.

Furthermore, we found that $cytCa^{2+}$ signaling was disturbed in the ferroptotic process and CoQs and OH-CoQs almost restored stable $cytCa^{2+}$ levels.

Lastly, we found that CoQ_{10} deficient cells were resistant to ferroptotic cell death, suggesting that some alternative regulatory pathway or antioxidant system may be acting to compensate its protective properties.

8. BIBLIOGRAPHY

Acosta, M. J., Vazquez Fonseca, L., Desbats, M. A., Cerqua, C., Zordan, R., Trevisson, E., & Salviati, L. (2016). Coenzyme Q biosynthesis in health and disease. *Biochim Biophys Acta*, *1857*(8), 1079-1085. https://doi.org/10.1016/j.bbabio.2016.03.036

Aeby, A., Sznajer, Y., Cave, H., Rebuffat, E., Van Coster, R., Rigal, O., & Van Bogaert, P. (2007). Cardiofaciocutaneous (CFC) syndrome associated with muscular coenzyme Q10 deficiency. *J Inherit Metab Dis*, *30*(5), 827. https://doi.org/10.1007/s10545-007-0612-0

Alcazar-Fabra, M., Navas, P., & Brea-Calvo, G. (2016). Coenzyme Q biosynthesis and its role in the respiratory chain structure. *Biochim Biophys Acta*, *1857*(8), 1073-1078. https://doi.org/10.1016/j.bbabio.2016.03.010

Alcazar-Fabra, M., Trevisson, E., & Brea-Calvo, G. (2018). Clinical syndromes associated with Coenzyme Q10 deficiency. *Essays Biochem*, *62*(3), 377-398. https://doi.org/10.1042/EBC20170107

Amoretti, M., Amsler, C., Bonomi, G., Bouchta, A., Bowe, P., Carraro, C., Cesar, C. L., Charlton, M., Collier, M. J., Doser, M., Filippini, V., Fine, K. S., Fontana, A., Fujiwara, M. C., Funakoshi, R., Genova, P., Hangst, J. S., Hayano, R. S., Holzscheiter, M. H., Jorgensen, L. V., Lagomarsino, V., Landua, R., Lindelof, D., Lodi Rizzini, E., Macri, M., Madsen, N., Manuzio, G., Marchesotti, M., Montagna, P., Pruys, H., Regenfus, C., Riedler, P., Rochet, J., Rotondi, A., Rouleau, G., Testera, G., Variola, A., Watson, T. L., van der Werf, D. P., & Collaboration, A. (2002). Production and detection of cold antihydrogen atoms. *Nature*, *419*(6906), 456-459. https://doi.org/10.1038/nature01096

Ayala, A., Munoz, M. F., & Arguelles, S. (2014). Lipid peroxidation: production, metabolism, and signaling mechanisms of malondialdehyde and 4-hydroxy-2-nonenal. *Oxid Med Cell Longev*, *2014*, 360438. https://doi.org/10.1155/2014/360438

Bagur, R., & Hajnoczky, G. (2017). Intracellular Ca(2+) Sensing: Its Role in Calcium Homeostasis and Signaling. *Mol Cell*, *66*(6), 780-788. https://doi.org/10.1016/j.molcel.2017.05.028

Balaban, R. S. (2009). The role of Ca(2+) signaling in the coordination of mitochondrial ATP production with cardiac work. *Biochim Biophys Acta*, *1787*(11), 1334-1341. https://doi.org/10.1016/j.bbabio.2009.05.011

Bannai, S., & Tateishi, N. (1986). Role of membrane transport in metabolism and function of glutathione in mammals. *J Membr Biol*, *89*(1), 1-8. https://doi.org/10.1007/BF01870891

Barros, M. H., Johnson, A., Gin, P., Marbois, B. N., Clarke, C. F., & Tzagoloff, A. (2005). The Saccharomyces cerevisiae COQ10 gene encodes a START domain protein required for function of coenzyme Q in respiration. *J Biol Chem*, *280*(52), 42627-42635. https://doi.org/10.1074/jbc.M510768200

Baughman, J. M., Perocchi, F., Girgis, H. S., Plovanich, M., Belcher-Timme, C. A., Sancak, Y., Bao, X. R., Strittmatter, L., Goldberger, O., Bogorad, R. L., Koteliansky, V., & Mootha, V. K. (2011). Integrative genomics identifies MCU as an essential component of the mitochondrial calcium uniporter. *Nature*, *476*(7360), 341-345. https://doi.org/10.1038/nature10234

Bedard, K., & Krause, K. H. (2007). The NOX family of ROS-generating NADPH oxidases: physiology and pathophysiology. *Physiol Rev*, *87*(1), 245-313. https://doi.org/10.1152/physrev.00044.2005

Bentinger, M., Brismar, K., & Dallner, G. (2007). The antioxidant role of coenzyme Q. *Mitochondrion*, *7 Suppl*, S41-50. https://doi.org/10.1016/j.mito.2007.02.006

Bentinger, M., Tekle, M., & Dallner, G. (2010). Coenzyme Q--biosynthesis and functions. *Biochem Biophys Res Commun*, *396*(1), 74-79. https://doi.org/10.1016/j.bbrc.2010.02.147

Berridge, M. J. (2012). Calcium signalling remodelling and disease. *Biochem Soc Trans*, *40*(2), 297-309. https://doi.org/10.1042/BST20110766

Berridge, M. J., Bootman, M. D., & Roderick, H. L. (2003). Calcium signalling: dynamics, homeostasis and remodelling. *Nat Rev Mol Cell Biol*, *4*(7), 517-529. https://doi.org/10.1038/nrm1155

Bersuker, K., Hendricks, J. M., Li, Z., Magtanong, L., Ford, B., Tang, P. H., Roberts, M. A., Tong, B., Maimone, T. J., Zoncu, R., Bassik, M. C., Nomura, D. K., Dixon, S. J., & Olzmann, J. A. (2019). The CoQ oxidoreductase FSP1 acts parallel to GPX4 to inhibit ferroptosis. *Nature*, *575*(7784), 688-692. https://doi.org/10.1038/s41586-019-1705-2

Bilan, D. S., & Belousov, V. V. (2017). New tools for redox biology: From imaging to manipulation. *Free Radic Biol Med*, *109*, 167-188. https://doi.org/10.1016/j.freeradbiomed.2016.12.004

Bogeski, I., Gulaboski, R., Kappl, R., Mirceski, V., Stefova, M., Petreska, J., & Hoth, M. (2011). Calcium binding and transport by coenzyme Q. *J Am Chem Soc*, *133*(24), 9293-9303. https://doi.org/10.1021/ja110190t

Bogeski, I., Kappl, R., Kummerow, C., Gulaboski, R., Hoth, M., & Niemeyer, B. A. (2011). Redox regulation of calcium ion channels: chemical and physiological aspects. *Cell Calcium*, *50*(5), 407-423. https://doi.org/10.1016/j.ceca.2011.07.006

Bogeski, I., Kummerow, C., Al-Ansary, D., Schwarz, E. C., Koehler, R., Kozai, D., Takahashi, N., Peinelt, C., Griesemer, D., Bozem, M., Mori, Y., Hoth, M., & Niemeyer, B. A. (2010). Differential redox regulation of ORAI ion channels: a mechanism to tune cellular calcium signaling. *Sci Signal*, *3*(115), ra24. https://doi.org/10.1126/scisignal.2000672

Boudina, S., & Abel, E. D. (2007). Diabetic cardiomyopathy revisited. *Circulation*, *115*(25), 3213-3223. https://doi.org/10.1161/CIRCULATIONAHA.106.679597

Boyman, L., Mikhasenko, H., Hiller, R., & Khananshvili, D. (2009). Kinetic and equilibrium properties of regulatory calcium sensors of NCX1 protein. *J Biol Chem*, *284*(10), 6185-6193. https://doi.org/10.1074/jbc.M809012200

Brastianos, P. K., Carter, S. L., Santagata, S., Cahill, D. P., Taylor-Weiner, A., Jones, R. T., Van Allen, E. M., Lawrence, M. S., Horowitz, P. M., Cibulskis, K., Ligon, K. L., Tabernero, J., Seoane, J., Martinez-Saez, E., Curry, W. T., Dunn, I. F., Paek, S. H., Park, S. H., McKenna, A., Chevalier, A., Rosenberg, M., Barker, F. G., 2nd, Gill, C. M., Van Hummelen, P., Thorner, A. R., Johnson, B. E., Hoang, M. P., Choueiri, T. K., Signoretti, S., Sougnez, C., Rabin, M. S., Lin, N. U., Winer, E. P., Stemmer-Rachamimov, A., Meyerson, M., Garraway, L., Gabriel, S., Lander, E. S., Beroukhim, R., Batchelor, T. T., Baselga, J., Louis, D. N., Getz, G., & Hahn, W. C. (2015). Genomic Characterization of Brain Metastases Reveals Branched Evolution and Potential Therapeutic Targets. *Cancer Discov*, *5*(11), 1164-1177. https://doi.org/10.1158/2159-8290.CD-15-0369

Bravo-Sagua, R., Parra, V., Lopez-Crisosto, C., Diaz, P., Quest, A. F., & Lavandero, S. (2017). Calcium Transport and Signaling in Mitochondria. *Compr Physiol*, *7*(2), 623-634. https://doi.org/10.1002/cphy.c160013

Brea-Calvo, G., Rodriguez-Hernandez, A., Fernandez-Ayala, D. J., Navas, P., & Sanchez-Alcazar, J. A. (2006). Chemotherapy induces an increase in coenzyme Q10 levels in cancer cell lines. *Free Radic Biol Med*, *40*(8), 1293-1302. https://doi.org/10.1016/j.freeradbiomed.2005.11.014

Brookes, P. S., Parker, N., Buckingham, J. A., Vidal-Puig, A., Halestrap, A. P., Gunter, T. E., Nicholls, D. G., Bernardi, P., Lemasters, J. J., & Brand, M. D. (2008). UCPs--unlikely calcium porters. *Nat Cell Biol*, *10*(11), 1235-1237; author reply 1237-1240. https://doi.org/10.1038/ncb1108-1235

Cabantchik, Z. I. (2014). Labile iron in cells and body fluids: physiology, pathology, and pharmacology. *Front Pharmacol*, *5*, 45. https://doi.org/10.3389/fphar.2014.00045

Cain, J. C., & Morton, R. A. (1955). Some minor constituents of liver oils. *Biochem J*, *60*(2), 274-283. https://doi.org/10.1042/bj0600274

Cao, J. Y., & Dixon, S. J. (2016). Mechanisms of ferroptosis. *Cell Mol Life Sci*, *73*(11-12), 2195-2209. https://doi.org/10.1007/s00018-016-2194-1

Casas, A. I., Dao, V. T., Daiber, A., Maghzal, G. J., Di Lisa, F., Kaludercic, N., Leach, S., Cuadrado, A., Jaquet, V., Seredenina, T., Krause, K. H., Lopez, M. G., Stocker, R., Ghezzi, P., & Schmidt, H. H. (2015). Reactive Oxygen-Related Diseases: Therapeutic Targets and Emerging Clinical Indications. *Antioxid Redox Signal*, *23*(14), 1171-1185. https://doi.org/10.1089/ars.2015.6433

Chen, S., Wang, Y., Zhang, H., Chen, R., Lv, F., Li, Z., Jiang, T., Lin, D., Zhang, H., Yang, L., & Kong, X. (2019). The Antioxidant MitoQ Protects Against CSE-Induced Endothelial Barrier Injury and Inflammation by Inhibiting ROS and Autophagy in Human Umbilical Vein Endothelial Cells. *Int J Biol Sci*, *15*(7), 1440-1451. https://doi.org/10.7150/ijbs.30193

Cogliati, S., Frezza, C., Soriano, M. E., Varanita, T., Quintana-Cabrera, R., Corrado, M., Cipolat, S., Costa, V., Casarin, A., Gomes, L. C., Perales-Clemente, E., Salviati, L., Fernandez-Silva, P., Enriquez, J. A., & Scorrano, L. (2013). Mitochondrial cristae shape determines respiratory chain supercomplexes assembly and respiratory efficiency. *Cell*, *155*(1), 160-171. https://doi.org/10.1016/j.cell.2013.08.032

Crane, F. L. (1957). Electron Transport and Cytochromes of Sub-Cellular Particles from Cauliflower Buds. *Plant Physiol*, *32*(6), 619-625. https://doi.org/10.1104/pp.32.6.619

Crane, F. L. (2007). Discovery of ubiquinone (coenzyme Q) and an overview of function. *Mitochondrion*, *7 Suppl*, S2-7. https://doi.org/10.1016/j.mito.2007.02.011

D'Autreaux, B., & Toledano, M. B. (2007). ROS as signalling molecules: mechanisms that generate specificity in ROS homeostasis. *Nat Rev Mol Cell Biol*, *8*(10), 813-824. https://doi.org/10.1038/nrm2256

De Stefani, D., Patron, M., & Rizzuto, R. (2015). Structure and function of the mitochondrial calcium uniporter complex. *Biochim Biophys Acta*, *1853*(9), 2006-2011. https://doi.org/10.1016/j.bbamcr.2015.04.008

De Stefani, D., Raffaello, A., Teardo, E., Szabo, I., & Rizzuto, R. (2011). A forty-kilodalton protein of the inner membrane is the mitochondrial calcium uniporter. *Nature*, *476*(7360), 336-340. https://doi.org/10.1038/nature10230

De Stefani, D., Rizzuto, R., & Pozzan, T. (2016). Enjoy the Trip: Calcium in Mitochondria Back and Forth. *Annu Rev Biochem*, *85*, 161-192. https://doi.org/10.1146/annurev-biochem-060614-034216

Deluca, H. F., & Engstrom, G. W. (1961). Calcium uptake by rat kidney mitochondria. *Proc Natl Acad Sci U S A*, *47*, 1744-1750. https://doi.org/10.1073/pnas.47.11.1744

Deng, S., Zheng, Y., Mo, Y., Xu, X., Li, Y., Zhang, Y., Liu, J., Chen, J., Tian, Y., & Ke, Y. (2021). Ferroptosis Suppressive Genes Correlate with Immunosuppression in Glioblastoma. *World Neurosurg*, *152*, e436-e448. https://doi.org/10.1016/j.wneu.2021.05.098

Dhanasekaran, A., Kotamraju, S., Kalivendi, S. V., Matsunaga, T., Shang, T., Keszler, A., Joseph, J., & Kalyanaraman, B. (2004). Supplementation of endothelial cells with mitochondria-targeted antioxidants inhibit peroxide-induced mitochondrial iron uptake, oxidative damage, and apoptosis. *J Biol Chem*, *279*(36), 37575-37587. https://doi.org/10.1074/jbc.M404003200

Diebold, L., & Chandel, N. S. (2016). Mitochondrial ROS regulation of proliferating cells. *Free Radic Biol Med*, *100*, 86-93. https://doi.org/10.1016/j.freeradbiomed.2016.04.198

Dikalov, S. (2011). Cross talk between mitochondria and NADPH oxidases. *Free Radic Biol Med*, *51*(7), 1289-1301. https://doi.org/10.1016/j.freeradbiomed.2011.06.033

Dixon, S. J., Lemberg, K. M., Lamprecht, M. R., Skouta, R., Zaitsev, E. M., Gleason, C. E., Patel, D. N., Bauer, A. J., Cantley, A. M., Yang, W. S., Morrison, B., 3rd, & Stockwell, B. R. (2012). Ferroptosis: an iron-dependent form of nonapoptotic cell death. *Cell*, *149*(5), 1060-1072. https://doi.org/10.1016/j.cell.2012.03.042

Dixon, S. J., Patel, D. N., Welsch, M., Skouta, R., Lee, E. D., Hayano, M., Thomas, A. G., Gleason, C. E., Tatonetti, N. P., Slusher, B. S., & Stockwell, B. R. (2014). Pharmacological inhibition of cystine-glutamate exchange induces endoplasmic reticulum stress and ferroptosis. *Elife*, *3*, e02523. https://doi.org/10.7554/eLife.02523

Doll, S., & Conrad, M. (2017). Iron and ferroptosis: A still ill-defined liaison. *IUBMB Life*, *69*(6), 423-434. https://doi.org/10.1002/iub.1616

Doll, S., Freitas, F. P., Shah, R., Aldrovandi, M., da Silva, M. C., Ingold, I., Goya Grocin, A., Xavier da Silva, T. N., Panzilius, E., Scheel, C. H., Mourao, A., Buday, K., Sato, M., Wanninger, J., Vignane, T., Mohana, V., Rehberg, M., Flatley, A., Schepers, A., Kurz, A., White, D., Sauer, M., Sattler, M., Tate, E. W., Schmitz, W., Schulze, A., O'Donnell, V., Proneth, B., Popowicz, G. M., Pratt, D. A., Angeli, J. P. F., & Conrad, M. (2019). FSP1 is a glutathione-independent ferroptosis suppressor. *Nature*, *575*(7784), 693-698. https://doi.org/10.1038/s41586-019-1707-0

Dranka, B. P., Benavides, G. A., Diers, A. R., Giordano, S., Zelickson, B. R., Reily, C., Zou, L., Chatham, J. C., Hill, B. G., Zhang, J., Landar, A., & Darley-Usmar, V. M. (2011). Assessing bioenergetic function in response to oxidative stress by metabolic profiling. *Free Radic Biol Med*, *51*(9), 1621-1635. https://doi.org/10.1016/j.freeradbiomed.2011.08.005

Echtay, K. S., Winkler, E., & Klingenberg, M. (2000). Coenzyme Q is an obligatory cofactor for uncoupling protein function. *Nature*, *408*(6812), 609-613. https://doi.org/10.1038/35046114

Ermakova, Y. G., Bilan, D. S., Matlashov, M. E., Mishina, N. M., Markvicheva, K. N., Subach, O. M., Subach, F. V., Bogeski, I., Hoth, M., Enikolopov, G., & Belousov, V. V. (2014). Red fluorescent

genetically encoded indicator for intracellular hydrogen peroxide. *Nat Commun*, *5*, 5222. https://doi.org/10.1038/ncomms6222

Esbenshade, T. A., Kang, C. H., Krueger, K. M., Miller, T. R., Witte, D. G., Roch, J. M., Masters, J. N., & Hancock, A. A. (2003). Differential activation of dual signaling responses by human H1 and H2 histamine receptors. *J Recept Signal Transduct Res*, *23*(1), 17-31. https://doi.org/10.1081/rrs-120018758

Fernandez-Ayala, D. J., Guerra, I., Jimenez-Gancedo, S., Cascajo, M. V., Gavilan, A., Dimauro, S., Hirano, M., Briones, P., Artuch, R., De Cabo, R., Salviati, L., & Navas, P. (2013). Survival transcriptome in the coenzyme Q10 deficiency syndrome is acquired by epigenetic modifications: a modelling study for human coenzyme Q10 deficiencies. *BMJ Open*, *3*(3). https://doi.org/10.1136/bmjopen-2012-002524

Fink, B. D., Herlein, J. A., Yorek, M. A., Fenner, A. M., Kerns, R. J., & Sivitz, W. I. (2012). Bioenergetic effects of mitochondrial-targeted coenzyme Q analogs in endothelial cells. *J Pharmacol Exp Ther*, *342*(3), 709-719. https://doi.org/10.1124/jpet.112.195586

Fink, B. D., O'Malley, Y., Dake, B. L., Ross, N. C., Prisinzano, T. E., & Sivitz, W. I. (2009). Mitochondrial targeted coenzyme Q, superoxide, and fuel selectivity in endothelial cells. *PLoS One*, *4*(1), e4250. https://doi.org/10.1371/journal.pone.0004250

Finkel, T. (2011). Signal transduction by reactive oxygen species. *J Cell Biol*, *194*(1), 7-15. https://doi.org/10.1083/jcb.201102095

Fontaine, E., Ichas, F., & Bernardi, P. (1998). A ubiquinone-binding site regulates the mitochondrial permeability transition pore. *J Biol Chem*, *273*(40), 25734-25740. https://doi.org/10.1074/jbc.273.40.25734

Forsgren, M., Attersand, A., Lake, S., Grunler, J., Swiezewska, E., Dallner, G., & Climent, I. (2004). Isolation and functional expression of human COQ2, a gene encoding a polyprenyl transferase involved in the synthesis of CoQ. *Biochem J*, *382*(Pt 2), 519-526. https://doi.org/10.1042/BJ20040261

Fridovich, I. (1997). Superoxide anion radical (O2-.), superoxide dismutases, and related matters. *J Biol Chem*, *272*(30), 18515-18517. https://doi.org/10.1074/jbc.272.30.18515

Friedmann Angeli, J. P., Schneider, M., Proneth, B., Tyurina, Y. Y., Tyurin, V. A., Hammond, V. J., Herbach, N., Aichler, M., Walch, A., Eggenhofer, E., Basavarajappa, D., Radmark, O., Kobayashi, S., Seibt, T., Beck, H., Neff, F., Esposito, I., Wanke, R., Forster, H., Yefremova, O., Heinrichmeyer, M., Bornkamm, G. W., Geissler, E. K., Thomas, S. B., Stockwell, B. R., O'Donnell, V. B., Kagan, V. E., Schick, J. A., & Conrad, M. (2014). Inactivation of the ferroptosis regulator Gpx4 triggers acute renal failure in mice. *Nat Cell Biol*, *16*(12), 1180-1191. https://doi.org/10.1038/ncb3064

Gaschler, M. M., & Stockwell, B. R. (2017). Lipid peroxidation in cell death. *Biochem Biophys Res Commun*, *482*(3), 419-425. https://doi.org/10.1016/j.bbrc.2016.10.086

Gempel, K., Topaloglu, H., Talim, B., Schneiderat, P., Schoser, B. G., Hans, V. H., Palmafy, B., Kale, G., Tokatli, A., Quinzii, C., Hirano, M., Naini, A., DiMauro, S., Prokisch, H., Lochmuller, H., & Horvath, R. (2007). The myopathic form of coenzyme Q10 deficiency is caused by mutations in the electron-transferring-flavoprotein dehydrogenase (ETFDH) gene. *Brain*, *130*(Pt 8), 2037-2044. https://doi.org/10.1093/brain/awm054

Geng, N., Shi, B. J., Li, S. L., Zhong, Z. Y., Li, Y. C., Xua, W. L., Zhou, H., & Cai, J. H. (2018). Knockdown of ferroportin accelerates erastin-induced ferroptosis in neuroblastoma cells. *Eur Rev Med Pharmacol Sci*, *22*(12), 3826-3836. https://doi.org/10.26355/eurrev_201806_15267

Gibhardt, C. S., Cappello, S., Bhardwaj, R., Schober, R., Kirsch, S. A., Bonilla Del Rio, Z., Gahbauer, S., Bochicchio, A., Sumanska, M., Ickes, C., Stejerean-Todoran, I., Mitkovski, M., Alansary, D., Zhang, X., Revazian, A., Fahrner, M., Lunz, V., Frischauf, I., Luo, T., Ezerina, D., Messens, J., Belousov, V. V., Hoth, M., Bockmann, R. A., Hediger, M. A., Schindl, R., & Bogeski, I. (2020). Oxidative Stress-Induced STIM2 Cysteine Modifications Suppress Store-Operated Calcium Entry. *Cell Rep*, *33*(3), 108292. https://doi.org/10.1016/j.celrep.2020.108292

Giorgi, C., Marchi, S., & Pinton, P. (2018). Publisher Correction: The machineries, regulation and cellular functions of mitochondrial calcium. *Nat Rev Mol Cell Biol*, *19*(11), 746. https://doi.org/10.1038/s41580-018-0066-2

Goh, K. Y., He, L., Song, J., Jinno, M., Rogers, A. J., Sethu, P., Halade, G. V., Rajasekaran, N. S., Liu, X., Prabhu, S. D., Darley-Usmar, V., Wende, A. R., & Zhou, L. (2019). Mitoquinone ameliorates pressure overload-induced cardiac fibrosis and left ventricular dysfunction in mice. *Redox Biol*, *21*, 101100. https://doi.org/10.1016/j.redox.2019.101100

Goldberg, J., Currais, A., Ates, G., Huang, L., Shokhirev, M., Maher, P., & Schubert, D. (2020). Targeting of intracellular Ca(2+) stores as a therapeutic strategy against age-related neurotoxicities. *NPJ Aging Mech Dis*, *6*, 10. https://doi.org/10.1038/s41514-020-00048-1

Gonzalez-Guardia, L., Yubero-Serrano, E. M., Delgado-Lista, J., Perez-Martinez, P., Garcia-Rios, A., Marin, C., Camargo, A., Delgado-Casado, N., Roche, H. M., Perez-Jimenez, F., Brennan, L., & Lopez-Miranda, J. (2015). Effects of the Mediterranean diet supplemented with coenzyme q10 on metabolomic profiles in elderly men and women. *J Gerontol A Biol Sci Med Sci*, *70*(1), 78-84. https://doi.org/10.1093/gerona/glu098

Gottwald, E. M., Duss, M., Bugarski, M., Haenni, D., Schuh, C. D., Landau, E. M., & Hall, A. M. (2018). The targeted anti-oxidant MitoQ causes mitochondrial swelling and depolarization in kidney tissue. *Physiol Rep*, *6*(7), e13667. https://doi.org/10.14814/phy2.13667

Graier, W. F., Trenker, M., & Malli, R. (2008). Mitochondrial Ca2+, the secret behind the function of uncoupling proteins 2 and 3? *Cell Calcium*, *44*(1), 36-50. https://doi.org/10.1016/j.ceca.2008.01.001

Grevel, A., Pfanner, N., & Becker, T. (2019). Coupling of import and assembly pathways in mitochondrial protein biogenesis. *Biol Chem*, *401*(1), 117-129. https://doi.org/10.1515/hsz-2019-0310

Griffiths, E. J., & Rutter, G. A. (2009). Mitochondrial calcium as a key regulator of mitochondrial ATP production in mammalian cells. *Biochim Biophys Acta*, *1787*(11), 1324-1333. https://doi.org/10.1016/j.bbabio.2009.01.019

Gulaboski, R., Bogeski, I., Mirceski, V., Saul, S., Pasieka, B., Haeri, H. H., Stefova, M., Stanoeva, J. P., Mitrev, S., Hoth, M., & Kappl, R. (2013). Hydroxylated derivatives of dimethoxy-1,4-benzoquinone as redox switchable earth-alkaline metal ligands and radical scavengers. *Sci Rep*, *3*, 1865. https://doi.org/10.1038/srep01865

Guo, R., Ma, H., Gao, F., Zhong, L., & Ren, J. (2009). Metallothionein alleviates oxidative stress-induced endoplasmic reticulum stress and myocardial dysfunction. *J Mol Cell Cardiol*, *47*(2), 228-237. https://doi.org/10.1016/j.yjmcc.2009.03.018

Gutierrez-Mariscal, F. M., Arenas-de Larriva, A. P., Limia-Perez, L., Romero-Cabrera, J. L., Yubero-Serrano, E. M., & Lopez-Miranda, J. (2020). Coenzyme Q10 Supplementation for the Reduction of Oxidative Stress: Clinical Implications in the Treatment of Chronic Diseases. *Int J Mol Sci*, *21*(21). https://doi.org/10.3390/ijms21217870

Hajnoczky, G., Csordas, G., Das, S., Garcia-Perez, C., Saotome, M., Sinha Roy, S., & Yi, M. (2006). Mitochondrial calcium signalling and cell death: approaches for assessing the role of mitochondrial Ca2+ uptake in apoptosis. *Cell Calcium*, *40*(5-6), 553-560. https://doi.org/10.1016/j.ceca.2006.08.016

Hao, L., Mi, J., Song, L., Guo, Y., Li, Y., Yin, Y., & Zhang, C. (2021). SLC40A1 Mediates Ferroptosis and Cognitive Dysfunction in Type 1 Diabetes. *Neuroscience*, *463*, 216-226. https://doi.org/10.1016/j.neuroscience.2021.03.009

Harris, I. S., Treloar, A. E., Inoue, S., Sasaki, M., Gorrini, C., Lee, K. C., Yung, K. Y., Brenner, D., Knobbe-Thomsen, C. B., Cox, M. A., Elia, A., Berger, T., Cescon, D. W., Adeoye, A., Brustle, A., Molyneux, S. D., Mason, J. M., Li, W. Y., Yamamoto, K., Wakeham, A., Berman, H. K., Khokha, R., Done, S. J., Kavanagh, T. J., Lam, C. W., & Mak, T. W. (2015). Glutathione and thioredoxin antioxidant pathways synergize to drive cancer initiation and progression. *Cancer Cell*, *27*(2), 211-222. https://doi.org/10.1016/j.ccell.2014.11.019

Hernandez-Camacho, J. D., Bernier, M., Lopez-Lluch, G., & Navas, P. (2018). Coenzyme Q10 Supplementation in Aging and Disease. *Front Physiol*, *9*, 44. https://doi.org/10.3389/fphys.2018.00044

Hirano, M., Quinzii, C. M., & Dimauro, S. (2006). Restoring balance to ataxia with coenzyme Q10 deficiency. *J Neurol Sci*, *246*(1-2), 11-12. https://doi.org/10.1016/j.jns.2006.03.017

Holmstrom, K. M., & Finkel, T. (2014). Cellular mechanisms and physiological consequences of redox-dependent signalling. *Nat Rev Mol Cell Biol*, *15*(6), 411-421. https://doi.org/10.1038/nrm3801

Huang, W., Cash, N., Wen, L., Szatmary, P., Mukherjee, R., Armstrong, J., Chvanov, M., Tepikin, A. V., Murphy, M. P., Sutton, R., & Criddle, D. N. (2015). Effects of the mitochondria-targeted antioxidant mitoquinone in murine acute pancreatitis. *Mediators Inflamm*, *2015*, 901780. https://doi.org/10.1155/2015/901780

Ishige, K., Chen, Q., Sagara, Y., & Schubert, D. (2001). The activation of dopamine D4 receptors inhibits oxidative stress-induced nerve cell death. *J Neurosci*, *21*(16), 6069-6076. https://www.ncbi.nlm.nih.gov/pubmed/11487630

J, O. U., Ryu, S. Y., Jhun, B. S., Hurst, S., & Sheu, S. S. (2014). Mitochondrial ion channels/transporters as sensors and regulators of cellular redox signaling. *Antioxid Redox Signal*, *21*(6), 987-1006. https://doi.org/10.1089/ars.2013.5681

Jacobson, J., & Duchen, M. R. (2002). Mitochondrial oxidative stress and cell death in astrocytes--requirement for stored Ca2+ and sustained opening of the permeability transition pore. *J Cell Sci*, *115*(Pt 6), 1175-1188. https://www.ncbi.nlm.nih.gov/pubmed/11884517

Jacobson, J., & Duchen, M. R. (2004). Interplay between mitochondria and cellular calcium signalling. *Mol Cell Biochem*, *256-257*(1-2), 209-218. https://doi.org/10.1023/b:mcbi.0000009869.29827.df

Jezek, P., & Hlavata, L. (2005). Mitochondria in homeostasis of reactive oxygen species in cell, tissues, and organism. *Int J Biochem Cell Biol*, *37*(12), 2478-2503. https://doi.org/10.1016/j.biocel.2005.05.013

Jiang, D., Zhao, L., & Clapham, D. E. (2009). Genome-wide RNAi screen identifies Letm1 as a mitochondrial Ca2+/H+ antiporter. *Science*, *326*(5949), 144-147. https://doi.org/10.1126/science.1175145

Jiang, X., Stockwell, B. R., & Conrad, M. (2021). Ferroptosis: mechanisms, biology and role in disease. *Nat Rev Mol Cell Biol*, *22*(4), 266-282. https://doi.org/10.1038/s41580-020-00324-8

Juhaszova, M., Church, P., Blaustein, M. P., & Stanley, E. F. (2000). Location of calcium transporters at presynaptic terminals. *Eur J Neurosci*, *12*(3), 839-846. https://doi.org/10.1046/j.1460-9568.2000.00974.x

Jung, H. J., Park, E. H., & Lim, C. J. (2009). Evaluation of anti-angiogenic, anti-inflammatory and antinociceptive activity of coenzyme Q(10) in experimental animals. *J Pharm Pharmacol*, *61*(10), 1391-1395. https://doi.org/10.1211/jpp/61.10.0017

Kagan, V., Serbinova, E., & Packer, L. (1990). Antioxidant effects of ubiquinones in microsomes and mitochondria are mediated by tocopherol recycling. *Biochem Biophys Res Commun*, *169*(3), 851-857. https://doi.org/10.1016/0006-291x(90)91971-t

Kai, H., Kuwahara, F., Tokuda, K., & Imaizumi, T. (2005). Diastolic dysfunction in hypertensive hearts: roles of perivascular inflammation and reactive myocardial fibrosis. *Hypertens Res*, *28*(6), 483-490. https://doi.org/10.1291/hypres.28.483

Kelso, G. F., Porteous, C. M., Coulter, C. V., Hughes, G., Porteous, W. K., Ledgerwood, E. C., Smith, R. A., & Murphy, M. P. (2001). Selective targeting of a redox-active ubiquinone to mitochondria within cells: antioxidant and antiapoptotic properties. *J Biol Chem*, *276*(7), 4588-4596. https://doi.org/10.1074/jbc.M009093200

Kelso, G. F., Porteous, C. M., Hughes, G., Ledgerwood, E. C., Gane, A. M., Smith, R. A., & Murphy, M. P. (2002). Prevention of mitochondrial oxidative damage using targeted antioxidants. *Ann N Y Acad Sci*, *959*, 263-274. https://doi.org/10.1111/j.1749-6632.2002.tb02098.x

Kirichok, Y., Krapivinsky, G., & Clapham, D. E. (2004). The mitochondrial calcium uniporter is a highly selective ion channel. *Nature*, *427*(6972), 360-364. https://doi.org/10.1038/nature02246

Kuhlbrandt, W. (2015). Structure and function of mitochondrial membrane protein complexes. *BMC Biol*, *13*, 89. https://doi.org/10.1186/s12915-015-0201-x

Kumar, A., Kaur, H., Devi, P., & Mohan, V. (2009). Role of coenzyme Q10 (CoQ10) in cardiac disease, hypertension and Meniere-like syndrome. *Pharmacol Ther*, *124*(3), 259-268. https://doi.org/10.1016/j.pharmthera.2009.07.003

Lakhal-Littleton, S., Wolna, M., Carr, C. A., Miller, J. J., Christian, H. C., Ball, V., Santos, A., Diaz, R., Biggs, D., Stillion, R., Holdship, P., Larner, F., Tyler, D. J., Clarke, K., Davies, B., &

Robbins, P. A. (2015). Cardiac ferroportin regulates cellular iron homeostasis and is important for cardiac function. *Proc Natl Acad Sci U S A*, *112*(10), 3164-3169. https://doi.org/10.1073/pnas.1422373112

Lambert, J. P., Luongo, T. S., Tomar, D., Jadiya, P., Gao, E., Zhang, X., Lucchese, A. M., Kolmetzky, D. W., Shah, N. S., & Elrod, J. W. (2019). MCUB Regulates the Molecular Composition of the Mitochondrial Calcium Uniporter Channel to Limit Mitochondrial Calcium Overload During Stress. *Circulation*, *140*(21), 1720-1733. https://doi.org/10.1161/CIRCULATIONAHA.118.037968

Lemasters, J. J., Theruvath, T. P., Zhong, Z., & Nieminen, A. L. (2009). Mitochondrial calcium and the permeability transition in cell death. *Biochim Biophys Acta*, *1787*(11), 1395-1401. https://doi.org/10.1016/j.bbabio.2009.06.009

Lemire, J., & Appanna, V. D. (2011). Aluminum toxicity and astrocyte dysfunction: a metabolic link to neurological disorders. *J Inorg Biochem*, *105*(11), 1513-1517. https://doi.org/10.1016/j.jinorgbio.2011.07.001

Letts, J. A., & Sazanov, L. A. (2017). Clarifying the supercomplex: the higher-order organization of the mitochondrial electron transport chain. *Nat Struct Mol Biol*, *24*(10), 800-808. https://doi.org/10.1038/nsmb.3460

Lewerenz, J., Ates, G., Methner, A., Conrad, M., & Maher, P. (2018). Oxytosis/Ferroptosis-(Re-) Emerging Roles for Oxidative Stress-Dependent Non-apoptotic Cell Death in Diseases of the Central Nervous System. *Front Neurosci*, *12*, 214. https://doi.org/10.3389/fnins.2018.00214

Li, J., Cao, F., Yin, H. L., Huang, Z. J., Lin, Z. T., Mao, N., Sun, B., & Wang, G. (2020). Ferroptosis: past, present and future. *Cell Death Dis*, *11*(2), 88. https://doi.org/10.1038/s41419-020-2298-2

Li, Y., Maher, P., & Schubert, D. (1997). A role for 12-lipoxygenase in nerve cell death caused by glutathione depletion. *Neuron*, *19*(2), 453-463. https://doi.org/10.1016/s0896-6273(00)80953-8

Lin, M. T., & Beal, M. F. (2006). Mitochondrial dysfunction and oxidative stress in neurodegenerative diseases. *Nature*, *443*(7113), 787-795. https://doi.org/10.1038/nature05292

Liou, J., Kim, M. L., Heo, W. D., Jones, J. T., Myers, J. W., Ferrell, J. E., Jr., & Meyer, T. (2005). STIM is a Ca2+ sensor essential for Ca2+-store-depletion-triggered Ca2+ influx. *Curr Biol*, *15*(13), 1235-1241. https://doi.org/10.1016/j.cub.2005.05.055

Liu, J. C., Syder, N. C., Ghorashi, N. S., Willingham, T. B., Parks, R. J., Sun, J., Fergusson, M. M., Liu, J., Holmstrom, K. M., Menazza, S., Springer, D. A., Liu, C., Glancy, B., Finkel, T., & Murphy, E. (2020). EMRE is essential for mitochondrial calcium uniporter activity in a mouse model. *JCI Insight*, *5*(4). https://doi.org/10.1172/jci.insight.134063

Lohman, D. C., Forouhar, F., Beebe, E. T., Stefely, M. S., Minogue, C. E., Ulbrich, A., Stefely, J. A., Sukumar, S., Luna-Sanchez, M., Jochem, A., Lew, S., Seetharaman, J., Xiao, R., Wang, H., Westphall, M. S., Wrobel, R. L., Everett, J. K., Mitchell, J. C., Lopez, L. C., Coon, J. J., Tong, L., & Pagliarini, D. J. (2014). Mitochondrial COQ9 is a lipid-binding protein that associates with COQ7 to enable coenzyme Q biosynthesis. *Proc Natl Acad Sci U S A*, *111*(44), E4697-4705. https://doi.org/10.1073/pnas.1413128111

Lu, S. C. (2013). Glutathione synthesis. *Biochim Biophys Acta*, *1830*(5), 3143-3153. https://doi.org/10.1016/j.bbagen.2012.09.008

Lyamzaev, K. G., Tokarchuk, A. V., Panteleeva, A. A., Mulkidjanian, A. Y., Skulachev, V. P., & Chernyak, B. V. (2018). Induction of autophagy by depolarization of mitochondria. *Autophagy*, *14*(5), 921-924. https://doi.org/10.1080/15548627.2018.1436937

Magner, M., Kolarova, H., Honzik, T., Svandova, I., & Zeman, J. (2015). Clinical manifestation of mitochondrial diseases. *Dev Period Med*, *19*(4), 441-449. https://www.ncbi.nlm.nih.gov/pubmed/26982751

Mailloux, R. J., & Harper, M. E. (2012). Mitochondrial proticity and ROS signaling: lessons from the uncoupling proteins. *Trends Endocrinol Metab*, *23*(9), 451-458. https://doi.org/10.1016/j.tem.2012.04.004

Mallilankaraman, K., Cardenas, C., Doonan, P. J., Chandramoorthy, H. C., Irrinki, K. M., Golenar, T., Csordas, G., Madireddi, P., Yang, J., Muller, M., Miller, R., Kolesar, J. E., Molgo, J., Kaufman, B., Hajnoczky, G., Foskett, J. K., & Madesh, M. (2012). MCUR1 is an essential component of

mitochondrial Ca2+ uptake that regulates cellular metabolism. *Nat Cell Biol*, *14*(12), 1336-1343. https://doi.org/10.1038/ncb2622

Mandal, P. K., Seiler, A., Perisic, T., Kolle, P., Banjac Canak, A., Forster, H., Weiss, N., Kremmer, E., Lieberman, M. W., Bannai, S., Kuhlencordt, P., Sato, H., Bornkamm, G. W., & Conrad, M. (2010). System x(c)- and thioredoxin reductase 1 cooperatively rescue glutathione deficiency. *J Biol Chem*, *285*(29), 22244-22253. https://doi.org/10.1074/jbc.M110.121327

Mao, P., Manczak, M., Shirendeb, U. P., & Reddy, P. H. (2013). MitoQ, a mitochondria-targeted antioxidant, delays disease progression and alleviates pathogenesis in an experimental autoimmune encephalomyelitis mouse model of multiple sclerosis. *Biochim Biophys Acta*, *1832*(12), 2322-2331. https://doi.org/10.1016/j.bbadis.2013.09.005

Marbois, B., Gin, P., Faull, K. F., Poon, W. W., Lee, P. T., Strahan, J., Shepherd, J. N., & Clarke, C. F. (2005). Coq3 and Coq4 define a polypeptide complex in yeast mitochondria for the biosynthesis of coenzyme Q. *J Biol Chem*, *280*(21), 20231-20238. https://doi.org/10.1074/jbc.M501315200

Marbois, B., Gin, P., Gulmezian, M., & Clarke, C. F. (2009). The yeast Coq4 polypeptide organizes a mitochondrial protein complex essential for coenzyme Q biosynthesis. *Biochim Biophys Acta*, *1791*(1), 69-75. https://doi.org/10.1016/j.bbalip.2008.10.006

Marcheggiani, F., Cirilli, I., Orlando, P., Silvestri, S., Vogelsang, A., Knott, A., Blatt, T., Weise, J. M., & Tiano, L. (2019). Modulation of Coenzyme Q10 content and oxidative status in human dermal fibroblasts using HMG-CoA reductase inhibitor over a broad range of concentrations. From mitohormesis to mitochondrial dysfunction and accelerated aging. *Aging (Albany NY)*, *11*(9), 2565-2582. https://doi.org/10.18632/aging.101926

Marthandan, S., Murphy, M. P., Billett, E., & Barnett, Y. (2011). An investigation of the effects of MitoQ on human peripheral mononuclear cells. *Free Radic Res*, *45*(3), 351-358. https://doi.org/10.3109/10715762.2010.532497

McKenzie, M., Lim, S. C., & Duchen, M. R. (2017). Simultaneous Measurement of Mitochondrial Calcium and Mitochondrial Membrane Potential in Live Cells by Fluorescent Microscopy. *J Vis Exp*(119). https://doi.org/10.3791/55166

Mitchell, P. (1975). The protonmotive Q cycle: a general formulation. *FEBS Lett*, *59*(2), 137-139. https://doi.org/10.1016/0014-5793(75)80359-0

Miyamoto, M., Murphy, T. H., Schnaar, R. L., & Coyle, J. T. (1989). Antioxidants protect against glutamate-induced cytotoxicity in a neuronal cell line. *J Pharmacol Exp Ther*, *250*(3), 1132-1140. https://www.ncbi.nlm.nih.gov/pubmed/2778712

Mohseni, M., Vafa, M. R., Hajimiresmail, S. J., Zarrati, M., Rahimi Forushani, A., Bitarafan, V., & Shidfar, F. (2014). Effects of coenzyme q10 supplementation on serum lipoproteins, plasma fibrinogen, and blood pressure in patients with hyperlipidemia and myocardial infarction. *Iran Red Crescent Med J*, *16*(10), e16433. https://doi.org/10.5812/ircmj.16433

Montero, R., Sanchez-Alcazar, J. A., Briones, P., Navarro-Sastre, A., Gallardo, E., Bornstein, B., Herrero-Martin, D., Rivera, H., Martin, M. A., Marti, R., Garcia-Cazorla, A., Montoya, J., Navas, P., & Artuch, R. (2009). Coenzyme Q10 deficiency associated with a mitochondrial DNA depletion syndrome: a case report. *Clin Biochem*, *42*(7-8), 742-745. https://doi.org/10.1016/j.clinbiochem.2008.10.027

Mortensen, S. A., Rosenfeldt, F., Kumar, A., Dolliner, P., Filipiak, K. J., Pella, D., Alehagen, U., Steurer, G., Littarru, G. P., & Investigators, Q. S. S. (2014). The effect of coenzyme Q10 on morbidity and mortality in chronic heart failure: results from Q-SYMBIO: a randomized double-blind trial. *JACC Heart Fail*, *2*(6), 641-649. https://doi.org/10.1016/j.jchf.2014.06.008

Murphy, M. P. (2009). How mitochondria produce reactive oxygen species. *Biochem J*, *417*(1), 1-13. https://doi.org/10.1042/BJ20081386

Murphy, T. H., Malouf, A. T., Sastre, A., Schnaar, R. L., & Coyle, J. T. (1988). Calcium-dependent glutamate cytotoxicity in a neuronal cell line. *Brain Res*, *444*(2), 325-332. https://doi.org/10.1016/0006-8993(88)90941-9

Murphy, T. H., Schnaar, R. L., & Coyle, J. T. (1990). Immature cortical neurons are uniquely sensitive to glutamate toxicity by inhibition of cystine uptake. *FASEB J*, *4*(6), 1624-1633. https://www.ncbi.nlm.nih.gov/pubmed/2180770

Muthukumaran, K., Kanwar, A., Vegh, C., Marginean, A., Elliott, A., Guilbeault, N., Badour, A., Sikorska, M., Cohen, J., & Pandey, S. (2018). Ubisol-Q10 (a Nanomicellar Water-Soluble Formulation of CoQ10) Treatment Inhibits Alzheimer-Type Behavioral and Pathological Symptoms in a Double Transgenic Mouse (TgAPEswe, PSEN1dE9) Model of Alzheimer's Disease. *J Alzheimers Dis*, *61*(1), 221-236. https://doi.org/10.3233/JAD-170275

Nagase, H., Katagiri, Y., Oh-Hashi, K., Geller, H. M., & Hirata, Y. (2020). Reduced Sulfation Enhanced Oxytosis and Ferroptosis in Mouse Hippocampal HT22 Cells. *Biomolecules*, *10*(1). https://doi.org/10.3390/biom10010092

Nakagami, H., Takemoto, M., & Liao, J. K. (2003). NADPH oxidase-derived superoxide anion mediates angiotensin II-induced cardiac hypertrophy. *J Mol Cell Cardiol*, *35*(7), 851-859. https://doi.org/10.1016/s0022-2828(03)00145-7

Nakayama, H., Chen, X., Baines, C. P., Klevitsky, R., Zhang, X., Zhang, H., Jaleel, N., Chua, B. H., Hewett, T. E., Robbins, J., Houser, S. R., & Molkentin, J. D. (2007). Ca2+- and mitochondrial-dependent cardiomyocyte necrosis as a primary mediator of heart failure. *J Clin Invest*, *117*(9), 2431-2444. https://doi.org/10.1172/JCI31060

Nicolson, G. L. (2014). Mitochondrial Dysfunction and Chronic Disease: Treatment With Natural Supplements. *Integr Med (Encinitas)*, *13*(4), 35-43. https://www.ncbi.nlm.nih.gov/pubmed/26770107

https://www.ncbi.nlm.nih.gov/pmc/articles/PMC4566449/pdf/35-43.pdf

Olson, R. E., & Rudney, H. (1983). Biosynthesis of ubiquinone. *Vitam Horm*, *40*, 1-43. https://doi.org/10.1016/s0083-6729(08)60431-8

Ouyang, L., & Gong, J. (2020). Mitochondrial-targeted ubiquinone: A potential treatment for COVID-19. *Med Hypotheses*, *144*, 110161. https://doi.org/10.1016/j.mehy.2020.110161

Pak, V. V., Ezerina, D., Lyublinskaya, O. G., Pedre, B., Tyurin-Kuzmin, P. A., Mishina, N. M., Thauvin, M., Young, D., Wahni, K., Martinez Gache, S. A., Demidovich, A. D., Ermakova, Y. G., Maslova, Y. D., Shokhina, A. G., Eroglu, E., Bilan, D. S., Bogeski, I., Michel, T., Vriz, S., Messens, J., & Belousov, V. V. (2020). Ultrasensitive Genetically Encoded Indicator for Hydrogen Peroxide Identifies Roles for the Oxidant in Cell Migration and Mitochondrial Function. *Cell Metab*, *31*(3), 642-653 e646. https://doi.org/10.1016/j.cmet.2020.02.003

Palty, R., Silverman, W. F., Hershfinkel, M., Caporale, T., Sensi, S. L., Parnis, J., Nolte, C., Fishman, D., Shoshan-Barmatz, V., Herrmann, S., Khananshvili, D., & Sekler, I. (2010). NCLX is an essential component of mitochondrial Na+/Ca2+ exchange. *Proc Natl Acad Sci U S A*, *107*(1), 436-441. https://doi.org/10.1073/pnas.0908099107

Parekh, A. B. (2008). Mitochondrial regulation of store-operated CRAC channels. *Cell Calcium*, *44*(1), 6-13. https://doi.org/10.1016/j.ceca.2007.12.006

Parekh, A. B., & Putney, J. W., Jr. (2005). Store-operated calcium channels. *Physiol Rev*, *85*(2), 757-810. https://doi.org/10.1152/physrev.00057.2003

Patron, M., Raffaello, A., Granatiero, V., Tosatto, A., Merli, G., De Stefani, D., Wright, L., Pallafacchina, G., Terrin, A., Mammucari, C., & Rizzuto, R. (2013). The mitochondrial calcium uniporter (MCU): molecular identity and physiological roles. *J Biol Chem*, *288*(15), 10750-10758. https://doi.org/10.1074/jbc.R112.420752

Pedrera, L., Espiritu, R. A., Ros, U., Weber, J., Schmitt, A., Stroh, J., Hailfinger, S., von Karstedt, S., & Garcia-Saez, A. J. (2021). Ferroptotic pores induce Ca(2+) fluxes and ESCRT-III activation to modulate cell death kinetics. *Cell Death Differ*, *28*(5), 1644-1657. https://doi.org/10.1038/s41418-020-00691-x

Perocchi, F., Gohil, V. M., Girgis, H. S., Bao, X. R., McCombs, J. E., Palmer, A. E., & Mootha, V. K. (2010). MICU1 encodes a mitochondrial EF hand protein required for Ca(2+) uptake. *Nature*, *467*(7313), 291-296. https://doi.org/10.1038/nature09358

Petrungaro, C., Zimmermann, K. M., Kuttner, V., Fischer, M., Dengjel, J., Bogeski, I., & Riemer, J. (2015). The Ca(2+)-Dependent Release of the Mia40-Induced MICU1-MICU2 Dimer from MCU Regulates Mitochondrial Ca(2+) Uptake. *Cell Metab*, *22*(4), 721-733. https://doi.org/10.1016/j.cmet.2015.08.019

Piconi, L., Quagliaro, L., & Ceriello, A. (2003). Oxidative stress in diabetes. *Clin Chem Lab Med*, *41*(9), 1144-1149. https://doi.org/10.1515/CCLM.2003.177

Pokrzywinski, K. L., Biel, T. G., Kryndushkin, D., & Rao, V. A. (2016). Therapeutic Targeting of the Mitochondria Initiates Excessive Superoxide Production and Mitochondrial Depolarization Causing Decreased mtDNA Integrity. *PLoS One*, *11*(12), e0168283. https://doi.org/10.1371/journal.pone.0168283

Putney, J. W., Jr. (1986). A model for receptor-regulated calcium entry. *Cell Calcium*, *7*(1), 1-12. https://doi.org/10.1016/0143-4160(86)90026-6

Putney, J. W., Jr. (1990). Capacitative calcium entry revisited. *Cell Calcium*, *11*(10), 611-624. https://doi.org/10.1016/0143-4160(90)90016-n

Quinzii, C. M., Kattah, A. G., Naini, A., Akman, H. O., Mootha, V. K., DiMauro, S., & Hirano, M. (2005). Coenzyme Q deficiency and cerebellar ataxia associated with an aprataxin mutation. *Neurology*, *64*(3), 539-541. https://doi.org/10.1212/01.WNL.0000150588.75281.58

Quinzii, C. M., Tadesse, S., Naini, A., & Hirano, M. (2012). Effects of inhibiting CoQ10 biosynthesis with 4-nitrobenzoate in human fibroblasts. *PLoS One*, *7*(2), e30606. https://doi.org/10.1371/journal.pone.0030606

Rao, V. A., Klein, S. R., Bonar, S. J., Zielonka, J., Mizuno, N., Dickey, J. S., Keller, P. W., Joseph, J., Kalyanaraman, B., & Shacter, E. (2010). The antioxidant transcription factor Nrf2 negatively regulates autophagy and growth arrest induced by the anticancer redox agent mitoquinone. *J Biol Chem*, *285*(45), 34447-34459. https://doi.org/10.1074/jbc.M110.133579

Rasmussen, U., Broogger Christensen, S., & Sandberg, F. (1978). Thapsigargine and thapsigargicine, two new histamine liberators from Thapsia garganica L. *Acta Pharm Suec*, *15*(2), 133-140. https://www.ncbi.nlm.nih.gov/pubmed/79299

Rasola, A., & Bernardi, P. (2011). Mitochondrial permeability transition in Ca(2+)-dependent apoptosis and necrosis. *Cell Calcium*, *50*(3), 222-233. https://doi.org/10.1016/j.ceca.2011.04.007

Reily, C., Mitchell, T., Chacko, B. K., Benavides, G., Murphy, M. P., & Darley-Usmar, V. (2013). Mitochondrially targeted compounds and their impact on cellular bioenergetics. *Redox Biol*, *1*(1), 86-93. https://doi.org/10.1016/j.redox.2012.11.009

Rodriguez-Aguilera, J. C., Cortes, A. B., Fernandez-Ayala, D. J., & Navas, P. (2017). Biochemical Assessment of Coenzyme Q10 Deficiency. *J Clin Med*, *6*(3). https://doi.org/10.3390/jcm6030027

Romero-Moya, D., Santos-Ocana, C., Castano, J., Garrabou, G., Rodriguez-Gomez, J. A., Ruiz-Bonilla, V., Bueno, C., Gonzalez-Rodriguez, P., Giorgetti, A., Perdiguero, E., Prieto, C., Moren-Nunez, C., Fernandez-Ayala, D. J., Victoria Cascajo, M., Velasco, I., Canals, J. M., Montero, R., Yubero, D., Jou, C., Lopez-Barneo, J., Cardellach, F., Munoz-Canoves, P., Artuch, R., Navas, P., & Menendez, P. (2017). Genetic Rescue of Mitochondrial and Skeletal Muscle Impairment in an Induced Pluripotent Stem Cells Model of Coenzyme Q10 Deficiency. *Stem Cells*, *35*(7), 1687-1703. https://doi.org/10.1002/stem.2634

Roos, J., DiGregorio, P. J., Yeromin, A. V., Ohlsen, K., Lioudyno, M., Zhang, S., Safrina, O., Kozak, J. A., Wagner, S. L., Cahalan, M. D., Velicelebi, G., & Stauderman, K. A. (2005). STIM1, an essential and conserved component of store-operated Ca2+ channel function. *J Cell Biol*, *169*(3), 435-445. https://doi.org/10.1083/jcb.200502019

Sacconi, S., Trevisson, E., Salviati, L., Ayme, S., Rigal, O., Redondo, A. G., Mancuso, M., Siciliano, G., Tonin, P., Angelini, C., Aure, K., Lombes, A., & Desnuelle, C. (2010). Coenzyme Q10 is frequently reduced in muscle of patients with mitochondrial myopathy. *Neuromuscul Disord*, *20*(1), 44-48. https://doi.org/10.1016/j.nmd.2009.10.014

Salviati, L., Trevisson, E., Doimo, M., & Navas, P. (1993). Primary Coenzyme Q10 Deficiency. In M. P. Adam, H. H. Ardinger, R. A. Pagon, S. E. Wallace, L. J. H. Bean, G. Mirzaa, & A. Amemiya (Eds.), *GeneReviews((R))*. https://www.ncbi.nlm.nih.gov/pubmed/28125198

Samanta, K., Mirams, G. R., & Parekh, A. B. (2018). Sequential forward and reverse transport of the Na(+) Ca(2+) exchanger generates Ca(2+) oscillations within mitochondria. *Nat Commun*, *9*(1), 156. https://doi.org/10.1038/s41467-017-02638-2

Saul, S., Gibhardt, C. S., Schmidt, B., Lis, A., Pasieka, B., Conrad, D., Jung, P., Gaupp, R., Wonnenberg, B., Diler, E., Stanisz, H., Vogt, T., Schwarz, E. C., Bischoff, M., Herrmann, M., Tschernig, T., Kappl, R., Rieger, H., Niemeyer, B. A., & Bogeski, I. (2016). A calcium-redox feedback loop

controls human monocyte immune responses: The role of ORAI Ca2+ channels. *Sci Signal*, *9*(418), ra26. https://doi.org/10.1126/scisignal.aaf1639

Schaub, M. C., & Kunz, B. (1986). Regulation of contraction in cardiac and smooth muscles. *J Cardiovasc Pharmacol*, *8 Suppl 8*, S117-123. https://doi.org/10.1097/00005344-198600088-00024

Schindl, R., Muik, M., Fahrner, M., Derler, I., Fritsch, R., Bergsmann, J., & Romanin, C. (2009). Recent progress on STIM1 domains controlling Orai activation. *Cell Calcium*, *46*(4), 227-232. https://doi.org/10.1016/j.ceca.2009.08.003

Sharifi, N., Tabrizi, R., Moosazadeh, M., Mirhosseini, N., Lankarani, K. B., Akbari, M., Chamani, M., Kolahdooz, F., & Asemi, Z. (2018). The Effects of Coenzyme Q10 Supplementation on Lipid Profiles Among Patients with Metabolic Diseases: A Systematic Review and Meta-analysis of Randomized Controlled Trials. *Curr Pharm Des*, *24*(23), 2729-2742. https://doi.org/10.2174/1381612824666180406104516

Shen, Q., & Pierce, J. D. (2015). Supplementation of Coenzyme Q10 among Patients with Type 2 Diabetes Mellitus. *Healthcare (Basel)*, *3*(2), 296-309. https://doi.org/10.3390/healthcare3020296

Skulachev, V. P. (2009). New data on biochemical mechanism of programmed senescence of organisms and antioxidant defense of mitochondria. *Biochemistry (Mosc)*, *74*(12), 1400-1403. https://doi.org/10.1134/s0006297909120165

Stefely, J. A., Reidenbach, A. G., Ulbrich, A., Oruganty, K., Floyd, B. J., Jochem, A., Saunders, J. M., Johnson, I. E., Minogue, C. E., Wrobel, R. L., Barber, G. E., Lee, D., Li, S., Kannan, N., Coon, J. J., Bingman, C. A., & Pagliarini, D. J. (2015). Mitochondrial ADCK3 employs an atypical protein kinase-like fold to enable coenzyme Q biosynthesis. *Mol Cell*, *57*(1), 83-94. https://doi.org/10.1016/j.molcel.2014.11.002

Tabara, L. C., Poveda, J., Martin-Cleary, C., Selgas, R., Ortiz, A., & Sanchez-Nino, M. D. (2014). Mitochondria-targeted therapies for acute kidney injury. *Expert Rev Mol Med*, *16*, e13. https://doi.org/10.1017/erm.2014.14

Tait, S. W., & Green, D. R. (2012). Mitochondria and cell signalling. *J Cell Sci*, *125*(Pt 4), 807-815. https://doi.org/10.1242/jcs.099234

Takano, H., Zou, Y., Hasegawa, H., Akazawa, H., Nagai, T., & Komuro, I. (2003). Oxidative stress-induced signal transduction pathways in cardiac myocytes: involvement of ROS in heart diseases. *Antioxid Redox Signal*, *5*(6), 789-794. https://doi.org/10.1089/152308603770380098

Tan, S., Sagara, Y., Liu, Y., Maher, P., & Schubert, D. (1998). The regulation of reactive oxygen species production during programmed cell death. *J Cell Biol*, *141*(6), 1423-1432. https://doi.org/10.1083/jcb.141.6.1423

Tan, S., Schubert, D., & Maher, P. (2001). Oxytosis: A novel form of programmed cell death. *Curr Top Med Chem*, *1*(6), 497-506. https://doi.org/10.2174/1568026013394741

Thanan, R., Oikawa, S., Hiraku, Y., Ohnishi, S., Ma, N., Pinlaor, S., Yongvanit, P., Kawanishi, S., & Murata, M. (2014). Oxidative stress and its significant roles in neurodegenerative diseases and cancer. *Int J Mol Sci*, *16*(1), 193-217. https://doi.org/10.3390/ijms16010193

Tinning, P. W., Franssen, A., Hridi, S. U., Bushell, T. J., & McConnell, G. (2018). A 340/380 nm light-emitting diode illuminator for Fura-2 AM ratiometric Ca(2+) imaging of live cells with better than 5 nM precision. *J Microsc*, *269*(3), 212-220. https://doi.org/10.1111/jmi.12616

Tran, U. C., & Clarke, C. F. (2007). Endogenous synthesis of coenzyme Q in eukaryotes. *Mitochondrion*, *7 Suppl*, S62-71. https://doi.org/10.1016/j.mito.2007.03.007

Turunen, M., Olsson, J., & Dallner, G. (2004). Metabolism and function of coenzyme Q. *Biochim Biophys Acta*, *1660*(1-2), 171-199. https://doi.org/10.1016/j.bbamem.2003.11.012

Xiao, L., Xu, X., Zhang, F., Wang, M., Xu, Y., Tang, D., Wang, J., Qin, Y., Liu, Y., Tang, C., He, L., Greka, A., Zhou, Z., Liu, F., Dong, Z., & Sun, L. (2017). The mitochondria-targeted antioxidant MitoQ ameliorated tubular injury mediated by mitophagy in diabetic kidney disease via Nrf2/PINK1. *Redox Biol*, *11*, 297-311. https://doi.org/10.1016/j.redox.2016.12.022

Xie, L. X., Hsieh, E. J., Watanabe, S., Allan, C. M., Chen, J. Y., Tran, U. C., & Clarke, C. F. (2011). Expression of the human atypical kinase ADCK3 rescues coenzyme Q biosynthesis and

phosphorylation of Coq polypeptides in yeast coq8 mutants. *Biochim Biophys Acta*, *1811*(5), 348-360. https://doi.org/10.1016/j.bbalip.2011.01.009

Yang, L., Calingasan, N. Y., Wille, E. J., Cormier, K., Smith, K., Ferrante, R. J., & Beal, M. F. (2009). Combination therapy with coenzyme Q10 and creatine produces additive neuroprotective effects in models of Parkinson's and Huntington's diseases. *J Neurochem*, *109*(5), 1427-1439. https://doi.org/10.1111/j.1471-4159.2009.06074.x

Yang, W. S., SriRamaratnam, R., Welsch, M. E., Shimada, K., Skouta, R., Viswanathan, V. S., Cheah, J. H., Clemons, P. A., Shamji, A. F., Clish, C. B., Brown, L. M., Girotti, A. W., Cornish, V. W., Schreiber, S. L., & Stockwell, B. R. (2014). Regulation of ferroptotic cancer cell death by GPX4. *Cell*, *156*(1-2), 317-331. https://doi.org/10.1016/j.cell.2013.12.010

Yang, W. S., & Stockwell, B. R. (2008). Synthetic lethal screening identifies compounds activating iron-dependent, nonapoptotic cell death in oncogenic-RAS-harboring cancer cells. *Chem Biol*, *15*(3), 234-245. https://doi.org/10.1016/j.chembiol.2008.02.010

Yin, H., Xu, L., & Porter, N. A. (2011). Free radical lipid peroxidation: mechanisms and analysis. *Chem Rev*, *111*(10), 5944-5972. https://doi.org/10.1021/cr200084z

Yubero, D., Montero, R., Martin, M. A., Montoya, J., Ribes, A., Grazina, M., Trevisson, E., Rodriguez-Aguilera, J. C., Hargreaves, I. P., Salviati, L., Navas, P., Artuch, R., Co, Q. d. s. g., Jou, C., Jimenez-Mallebrera, C., Nascimento, A., Perez-Duenas, B., Ortez, C., Ramos, F., Colomer, J., O'Callaghan, M., Pineda, M., Garcia-Cazorla, A., Espinos, C., Ruiz, A., Macaya, A., Marce-Grau, A., Garcia-Villoria, J., Arias, A., Emperador, S., Ruiz-Pesini, E., Lopez-Gallardo, E., Neergheen, V., Simoes, M., Diogo, L., Blazquez, A., Gonzalez-Quintana, A., Delmiro, A., Dominguez-Gonzalez, C., Arenas, J., Garcia-Silva, M. T., Martin, E., Quijada, P., Hernandez-Lain, A., Moran, M., Rivas Infante, E., Avila Polo, R., Paradas Lope, C., Bautista Lorite, J., Martinez Fernandez, E. M., Cortes, A. B., Sanchez-Cuesta, A., Cascajo, M. V., Alcazar, M., & Brea-Calvo, G. (2016). Secondary coenzyme Q10 deficiencies in oxidative phosphorylation (OXPHOS) and non-OXPHOS disorders. *Mitochondrion*, *30*, 51-58. https://doi.org/10.1016/j.mito.2016.06.007

Zhai, Z., Zou, P., Liu, F., Xia, Z., & Li, J. (2021). Ferroptosis Is a Potential Novel Diagnostic and Therapeutic Target for Patients With Cardiomyopathy. *Front Cell Dev Biol*, *9*, 649045. https://doi.org/10.3389/fcell.2021.649045

Zhang, S. J., Zou, M., Lu, L., Lau, D., Ditzel, D. A., Delucinge-Vivier, C., Aso, Y., Descombes, P., & Bading, H. (2009). Nuclear calcium signaling controls expression of a large gene pool: identification of a gene program for acquired neuroprotection induced by synaptic activity. *PLoS Genet*, *5*(8), e1000604. https://doi.org/10.1371/journal.pgen.1000604

Zhang, S. L., Yu, Y., Roos, J., Kozak, J. A., Deerinck, T. J., Ellisman, M. H., Stauderman, K. A., & Cahalan, M. D. (2005). STIM1 is a Ca2+ sensor that activates CRAC channels and migrates from the Ca2+ store to the plasma membrane. *Nature*, *437*(7060), 902-905. https://doi.org/10.1038/nature04147

Zorov, D. B., Juhaszova, M., & Sollott, S. J. (2014). Mitochondrial reactive oxygen species (ROS) and ROS-induced ROS release. *Physiol Rev*, *94*(3), 909-950. https://doi.org/10.1152/physrev.00026.2013

Zozina, V. I., Covantev, S., Goroshko, O. A., Krasnykh, L. M., & Kukes, V. G. (2018). Coenzyme Q10 in Cardiovascular and Metabolic Diseases: Current State of the Problem. *Curr Cardiol Rev*, *14*(3), 164-174. https://doi.org/10.2174/1573403X14666180416115428

Supplementary data

Table S1. Differentially expressed genes in coenzyme Q_{10} deficiency

Gene symbol*	Gene title	FC†	FC‡	CoQ_{10}§	Q-RT-PCR¶	CoQ_{10}**	Regulation
C7orf55	Chromosome 7 open reading frame 55	−2.1	nc	–			-
BRP44	Brain protein 44	2,00	2,3	U	8	–2-fold	+
C10orf58	Chromosome 10 open reading frame 58	−19.5	−1.6	pR			-
CYB561	Cytochrome *b*561	−1.3	nc	O			-
CYB5A	Cytochrome *b*5-A	−1.4	−1.5	U			-
CYB5R1	Cytochrome *b*5 reductase 1	−1.3	nc	U			-
CYB5R2	Cytochrome *b*5 reductase 2	−1.4	−1.9	U			-
CYB5R3	Cytochrome *b*5 reductase 3	−1.4	−1.6	R			-
CYB5R4	Cytochrome *b*5 reductase 4	−1.3	−1.6	R			-
FDFT1	Farnesyl-diphosphate farnesyltransferase 1	−2.3	−1.5	U	−4.3	+2-fold	-
IDI1	Isopentenyl-diphosphate δ isomerase 1	−2.1	nc	U			-
CH25H	Cholesterol 25-hydroxylase	−10.8	−3.2	O	−1.3	–3-fold	-
RSAD2	Radical *S*-adenosyl methionine domain containing 2	−6.8	1,4	pR			-
INSIG1	Insulin-induced gene 1	−2.6	1,7	O			-
LDLR	Low density lipoprotein receptor	−3.0	−1.8	pR			-
SQLE	Squalene epoxidase	−2.5	nc	U			-
SCD	Stearoyl-coenzyme A desaturase (δ-9-desaturase)	−3.3	nc	U			-
CPE	Carboxypeptidase E	10,00	2,5	pR			+
PAPPA	Pregnancy-associated plasma protein A, pappalysin	2,50	1,7	R	4,8	–5-fold	+
PCSK2	Proprotein convertase subtilisin/kexin type 2	−75.5	−4.3	O			-
SCIN	Scinderin	−5.4	−1.4	O			-
PYGL	Phosphorylase, glycogen; liver	−2.5	−1.6	R			-
SLC40A1	Solute carrier family 40 (iron-regulated transporter)	7,60	2,9	R			+
QPRT	Quinolinate phosphoribosyltransferase	−3.4	nc	R			-
ATP8B1	ATPase, class I, type 8B and member 1	2,40	nc	pR			+

POSTN	Periostin, osteoblast specific factor	73,80	153,9	U	238,2	–20%	+
VEGFA	Vascular endothelial growth factor A	2,90	nc	–			+
SEMA5A	Semaphorin 5A, receptor for cell growth	3,60	1,6	pR			+
AEBP1	AE binding protein 1	66,10	nc	R			+
CSRP2	Cysteine and glycine-rich protein 2	5,30	1,5	R			+
DOK5	Docking protein 5	6,50	1,6	U			+
MID1	Midline 1 (Opitz/BBB syndrome)	3,90	4,4	U			+
CHURC1	Churchill domain containing 1	3,50	nc	–			+
CREG1	Repressor 1 of E1A-stimulated genes	3,00	1,3	R			+
RUNX1	Runt-related transcription factor 1 (aml1 oncogene)	1,90	1,6	–			+
BHLHB5	Basic helix-loop-helix domain containing; class B, 5	−6.1	−1.4	–			-
IFITM1	Interferon induced transmembrane protein 1 (9–27)	−3.8	−3.7	O			-
EDN1	Endothelin 1	−3.0	nc	U			-
MATN2	Matrilin 2	−9.2	nc	U			-
MCAM	Melanoma cell adhesion molecule	−6.7	−3.0	R	−10.9	10%	-
MKX	Mohawk homeobox	−4.5	−1.5	–			-
PSG6	Pregnancy specific β-1-glycoprotein 6	2,60	nc	–			+
DCN	Decorin	2,00	−1.6	–			+
PKP4	Plakophilin 4	2,00	1,4	U			+
EFEMP1	EGF-containing fibulin-like extracellular matrix protein 1	13,20	2,2	pR			+
VCAN	Versican	2,80	2,7	–	4,6	10%	+
SMARCA1	Component of SWI/SNF chromatin complex, member A1	−1.3	nc	pR			-
SMARCA4	Component of SWI/SNF chromatin complex, member A4	−1.9	nc	pR			-
CDK6	Cyclin-dependent kinase 6, overexpressed in tumour	1,40	2,9	U			+
CDKN1A	P21, inhibitor of CDK	−9.2	−2.1	U			-
CDKN1C	P57, inhibitor of CDK	−2.6	−1.3	R			-
CDKN3	Inhibitor of CDK, overexpressed in cancer cells	1,90	2,7	U			+
CD31	Cell surface antigen	−1.8	−1.5	R			-
RB1	Retinoblastoma protein	−1.4	nc	R			-
E2F7	E2F transcription factor 7	3,60	nc	U			+
E2F8	E2F transcription factor 8	2,20	nc	U			+
FST	Follistatin	2,60	1,4	O			+

BDNF	Brain-derived neurotrophic factor	−2.9	nc	pR			-
GRP	Gastrin-releasing peptide	−263.6	nc	–			-
NTNG1	Netrin G1	−8.3	1,8	U			-
PTN	Pleiotrophin (neurite growth-promoting factor 1)	−2.7	nc	R			-
FOXQ1	Forkhead box Q1	−6.5	nc	–			-
HOXA11	Homeobox A11	−4.3	−2.4	U			-
HOXC9	Homeobox C9	−4.8	−2.0	U			-
LHX9	LIM homeobox 9	−93.0	−1.5	U			-
SP110	SP110 nuclear body protein	−2.5	nc	pR			-
P2RY5	Purinergic receptor P2Y; G-protein coupled, 5	−4.4	−1.3	pR			-
TSPAN10	Tetraspanin 10	−10.1	nc	–			-
EPSTI1	Epithelial stromal interaction 1	−5.2	−1.4	R			-
TSHZ1	Teashirt zinc finger homeobox 1	−2.8	nc	R			-
KRT34	Keratin 34	−5.3	−7.6	R	−5.7	–60%	-
TPM1	Tropomyosin 1 (α)	−1.8	1,7	–			-
FOXP1	Forkhead box P1	2,30	nc	–			+
LMCD1	LIM and cysteine-rich domains 1	3,80	nc	U			+
CYP1B1	Cytochrome P450, family 1B and polypeptide 1	4,50	1,5	–	7	–5-fold	+
MGC87042	Similar to six epithelial antigen of prostate	12,20	–	R			+
TMEM49	Transmembrane protein 49/microRNA 21	1,90	nc	–			+
RAD23B	RAD23 homologue B (*Saccharomyces cerevisiae*)	2,20	nc	R			+
TXNIP	Thioredoxin-interacting protein	2,00	−4.9	–			+
SGK1	Serum/glucocorticoid regulated kinase 1	3,40	1,5	–			+
SOCS3	Suppressor of cytokine signalling 3	−3.6	nc	R			-
RHOU	Ras homologue gene family. member U	−8.3	nc	O			-
AIM1	Absent in melanoma 1	−4.5	−1.4	O			-
APCDD1	Adenomatosis polyposis coli down-regulated 1	−6.4	−1.8	O			-
MAGED1	Melanoma antigen family D, 1	−1.7	nc	U			-
MAGED4/4B	Melanoma antigen family D, 4/4B	−5.0	−1.6	U			-
RAC2	Small GTP-binding protein Rac2 (rho family)	−2.3	−1.3	U			-
TRIM55	Tripartite motif-containing 55	−11.7	−1.6	U			-
IFI6	Interferon, α-inducible protein 6	−4.9	−1.3	R			-
XAF1	XIAP associated factor-1	−3.0	−1.5	R			-

TNFRSF10D	Tumour necrosis factor receptor superfamily 10D	2,40	2,6	U	15,1	20%	+
SFRP1	Secreted frizzled-related protein 1	8,70	2,5	U	11,8	–2-fold	+
ARL4C	ADP-ribosylation factor-like 4C	3,80	1,6	pR			+
USP53	Ubiquitin specific peptidase 53	4,20	1,7	–			+
GABBR2	γ-aminobutyric acid B receptor, 2	13,80	2	U			+
CNGA3	Cyclic nucleotide gated channel α-3	−67.3	nc	–			-
GNG2	G-protein, γ-2	−4.2	1,4	pR			-
HERC6	Hect domain and RLD 6	−7.4	−1.4	R			-
MLPH	Melanophilin	−8.5	−1.9	R			-
NCK2	NCK adaptor protein 2	−1.7	nc	–			-
PARP14	Poly (ADP-ribose) polymerase family, member 14	−3.1	−1.5	–			-
CDC42SE2	CDC42 small effector 2	−2.8	nc	–			-
LY6K	Lymphocyte antigen 6 complex, locus K	−4.7	1,4	–			-
GALNAC4S-6ST	B cell RAG associated protein	−17.3	−2.5	O			-
TNFSF4	Tumour necrosis factor superfamily, member 4	−5.9	nc	–			-
TRIM14	Tripartite motif-containing 14	−4.5	nc	–			-
BTN3(A2/A3)	Butyrophilin 3 (A2/A3)	−2.0	−1.3	R			-
IFI27	Interferon, α-inducible protein 27	−9.8	nc	O			-
IFI44	Interferon-induced protein 44	−3.3	−2.3	R			-
IFI44L	Interferon-induced protein 44-like	−15.0	−1.9	R			-
IFIT1	Interferon-induced protein (tetratricopeptide repeats 1)	−5.3	nc	–			-
IFIT3	Interferon-induced protein (tetratricopeptide repeats 3)	−3.5	−1.7	R			-
GBP1	Guanylate binding protein 1, interferon-inducible	−2.7	–	–			-
ISG15	ISG15 ubiquitin-like modifier	−6.4	nc	R			-
MX1	Myxovirus resistance 1	−7.4	−1.8	pR			-
MX2	Myxovirus resistance 2	−6.1	−3.0	pR			-
OAS1	2′,5′-oligoadenylate synthetase 1, 40/46 kDa	−5.1	−4.9	R			-
OAS2	2′-5′-oligoadenylate synthetase 2, 69/71 kDa	−6.2	−1.6	R			-
OAS3	2′-5′-oligoadenylate synthetase 3, 100 kDa	−3.6	−1.3	R			-

OASL	2′-5′-oligoadenylate synthetase-like	−3.1	−2.6	R	-
PSMB9	Proteasome subunit, β-type, 9	−1.8	nc	U	-

†Full change (FC) in the comparative analysis ran with Affymetrix GeneChip Human Genome U133 Plus 2.0 Array. Values represent the FC (mean) for each gene corresponding to different patient samples (SAM analysis; R=1.5; false discovery rate (FDR) = 0 %). In parenthesis, FC of non-significant genes by the statistical threshold used, which were selected owing to their role in specific processes and pathways. In the case of different probes selected for one gene, values represent the mean of FC for each probe.

‡FC in the comparative analysis ran with Affymetrix Gene Chip Human Gene 1.0 ST Array. In parenthesis, FC of non-significant genes by the statistical threshold used. Genes with no change (nc).

§ Effect of CoQ_{10} supplementation on gene expression in CoQ_{10} deficiency: unaffected genes by CoQ_{10} treatment (U); genes that restored the expression either partially (pR) or completely (R); genes with opposite regulation than in CoQ_{10} deficiency (O); and specifically regulated genes only after CoQ_{10} supplementation (S). Genes non-affected by CoQ_{10} supplementation (−).

**Effect of CoQ_{10} supplementation on mRNA levels analysed by Q-RT-PCR. Positive values, increase on gene expression; negative values, decrease on gene expression.

Acknowledgments

First of all, I want to thank my dedicated supervisor, Prof. Dr. Ivan Bogeski, for giving me the opportunity to do this work and for the constant supervision that was at times much needed. I will never forget my first day in Göttingen with the nerves of a new beginning. I was feeling super excited but honestly a little lost, and you came to pick me up, and opened the doors of your lab for me. Thank you for supporting me since then during these 4 bumpy years.

I also want to thank Dr. Christine S. Gibhardt and Andrea Paluschkiwitz for their endless knowledge of microscope and laboratory techniques. Thank you for all the time you have dedicated to me, for every question resolved and for everything you have taught me. Your help has always been appreciated.

Thank you to everybody in the lab: to those who were at my arrival and gave me their help and friendship, Adina, Xin and Sabrina, good luck in your next projects! To all who have come after, Magdalena, Xhu-min, Christian, Lena and all the students, thank you for the good work environment that you create. And especially a huge thank to Ioana, for her help and scientific advice but above all for her friendship, for sharing so many laughs and for being there, always the first, when I needed it. I couldn't have more luck having you as a colleague!

Special thanks to those of you who have collaborated with my project, making it go ahead: Dr. Katrin Streckfuß-Bömeke, Johanna Heine, Yvonne Metz, Prof. Dr. Peter Rehling, Dr. David Pacheu Grau, Angela Boshnakovska, Prof. Dr. Niels Voigt, Prof. Placido Navas, Prof. Dr. Pablo Menéndez and Dr. Reinhard Kappl.

I would like to thank the members of the thesis committee, Prof. Dr. Michael Meinecke and Dr. Antje Ebert, for their support and guidance in my PhD. Besides, I thank Dr. Katrin Streckfuß-Bömeke, Prof. Dr. Ralph Kehlenbach and Prof. Dr. Thomas Meyer, for kindly agreeing to be part of my examination committee.

And finally, those who are part of my life. Empiezo con vosotras, Esther, Leti y Ángela, gracias por estar siempre, por hacerme sentir que la distancia sea más corta y por saber siempre como alegrar un mal día; no podría tener amigas mejores. A ti, Lalo, porque has conseguido que me sienta un poco más en casa, por ser mi vía de escape y simplemente porque me haces feliz. A mis tíos y abuela, por tantos ánimos y cariño y por hacer vuestros mis logros. A mi otra mitad, mi hermana, gracias por apoyarme en todo momento, ayudarme a no rendirme y hacerme sentir

que nunca estoy sola. Y especialmente, gracias a mis padres, porque me lo habéis dado todo, hasta ese empujoncito a veces necesario, para que siguiera mis sueños; vosotros siempre me habéis hecho creer y creéis que puedo con todo. ¡Os quiero mucho!

List of publications

Gibhardt CS, Cappello S, Bhardwaj R, Schober R, Kirsch SA, **Bonilla Del Rio Z**, Gahbauer S, Bochicchio A, Sumanska M, Ickes C, Stejerean-Todoran I, Mitkovski M, Alansary D, Zhang X, Revazian A, Fahrner M, Lunz V, Frischauf I, Luo T, Ezerina D, Messens J, Belousov VV, Hoth M, Böckmann RA, Hediger MA, Schindl R, Bogeski I. Oxidative Stress-Induced STIM2 Cysteine Modifications Suppress Store-Operated Calcium Entry. Cell Rep. 2020 Oct 20;33(3):108292

Katharina Zimmermann, Ioana Stejerean, Adina Vultur, Christine Gibhardt, Christian Ickes, Batool Shannan, Zurine Bonilla del Río, Sabrina Cappello, Hsu-Min Sung, Magdalena Shumanska, Xin Zhang, Anna Wölling, Maithily Nanadikar, Andrea Waters, Patricia Brafford, Jörg Wilting, Henning Urlaub, Dörthe Magdalena Katschinski, Peter Rehling, Christof Lenz, Alexander Roesch, Michael P. Schön, Meenhard Herlyn, Hedwig Stanisz, Ivan Bogeski. MCU controls melanoma progression through a redox-contro lled phenotype switch. (Under review in The EMBO Journal).

Ioana Stejerean-Todoran, Phyllis A. Gimotty, Andrea Watters, Patricia Brafford, Clemens Krepler, Tetiana Godok, Haiyin Li, Zuriñe Bonilla del Rio, Anke Zieseniss, Dörthe M. Katschinski, Sinem M. Sertel, Silvio O. Rizzoli, Bradley Garman, Katherine L. Nathanson Michal Lotem, Gordon B. Mills, Michael A. Davies, Michael P. Schön, Ivan Bogeski, Meenhard Herlyn, Adina Vultur. A distinct pattern of growth and RAC1 signaling in melanoma brain metastasis. (Submitted).